TÉCNICO LISBOA

UNIVERSIDADE DE LISBOA
INSTITUTO SUPERIOR TÉCNICO

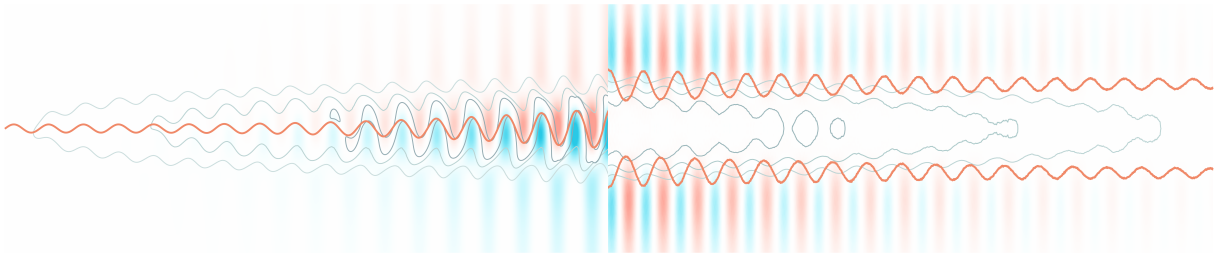

Properties of the hosing and self-modulation instabilities of long particle beams in overdense plasma

Mariana Azevedo Trocado Moreira

Supervisor: Doctor Jorge Miguel Ramos Domingues Ferreira Vieira
Co-Supervisors: Doctor Patric Muggli
Doctor Bernhard Holzer

Thesis approved in public session to obtain the PhD Degree in
Technological Physics Engineering

Jury final classification: Pass with Distinction and Honour

2024

TÉCNICO LISBOA

UNIVERSIDADE DE LISBOA
INSTITUTO SUPERIOR TÉCNICO

Properties of the hosing and self-modulation instabilities of long particle beams in overdense plasma

Mariana Azevedo Trocado Moreira

Supervisor: Doctor Jorge Miguel Ramos Domingues Ferreira Vieira
Co-Supervisors: Doctor Patric Muggli
Doctor Bernhard Holzer

Thesis approved in public session to obtain the PhD Degree in
Technological Physics Engineering

Jury final classification: Pass with Distinction and Honour

Jury

Chairperson: Doctor Luís Paulo da Mota Capitão Lemos Alves, Instituto Superior Técnico, Universidade de Lisboa

Members of the Committee:

Doctor Robert Bingham, University of Strathclyde Glasgow, United Kingdom
Doctor Alexander Pukhov, Institut für Theoretische Physik, Heinrich-Heine-Universität Düsseldorf, Germany
Doctor Jorge Miguel Ramos Domingues Ferreira Vieira, Instituto Superior Técnico, Universidade de Lisboa
Doctor Nelson Manuel Carreira Lopes, Instituto Superior Técnico, Universidade de Lisboa

Funding Institution

Fundação para a Ciência e a Tecnologia (FCT)

2024

There is only one corner of the universe you can be certain of improving, and that is your own self.

Aldous Huxley

Acknowledgments

Some people think of their doctoral thesis as a baby. If this is true, then the same piece of wisdom applies: it takes a village.

Despite what sounds like a logistical nightmare, I consider myself lucky to have had a team of three supervisors. Their complementing skill sets and easy cooperation formed an extra dense web of support. My profound thanks to Jorge Vieira, Patric Muggli and Bernhard Holzer for guiding me and for sharing both their knowledge and resources with me over these years.

The first three years of my PhD were spent at CERN. I initially sat in meetings with the "Run 1" generation of the AWAKE experiment, who already taught me so much without me realizing: Marlene Turner, Spencer Gessner, Joshua Moody, Mikhail Martyanov, Fabian Batsch, Anna-Maria Bachmann and Mathias Hüther. It was also a pleasure to work alongside a second generation of students: Pablo Morales Guzmán, Jan Pucek, Kook-Jin Moon and Tatiana Nechaeva.

A special word is reserved for my colleague and friend John Farmer, who, importantly, first noticed that the SMI equation should in fact be piecewise. What is the word? We will never know.

I have been part of the Group of Lasers and Plasmas (GoLP) and the Extreme Plasma Physics (EPP) team at IST since the beginning of my (albeit short) scientific career. GoLP contains multitudes when it comes to knowledge and character, and I am extremely grateful for the people I worked with (some of whom I consider dear friends) and the resources I was granted. In particular, I want to acknowledge Marija Vranić, Thomas Grismayer, Thales Silva, Ricardo Fonseca, Chiara Badiali, Róbert Babjak, Rui Torres, Miguel Pardal, Bernardo Malaca, Óscar Amaro and Patrícia Estrela. My gratitude includes some other EPP alumni and friends: Fábio Cruz, (Lígia) Diana Amorim, Dominika Maslarova, Bertrand Martinez, Joana Alves, Anton Helm, Giannandrea Inchingolo, Fabrizio del Gaudio, Kevin Schoeffler and Wenlong Zhang.

Leading a team of people seems like an extremely consuming job to me, so I want to express my heartfelt gratitude to both Luís Oliveira e Silva and Edda Gschwendtner for their availability and professional support throughout this PhD.

Some people make all the difference in less visible ways. Thank you so much to Cláudia Romão for making trips to conferences possible and overcoming burocratic hurdles, and always in a gentle, pragmatic manner. I also want to acknowledge the extremely thoughtful and competent service provided by Ana Rosa and Sara Teixeira of the Post-Graduation Office at IST, which is the point of contact with students at the most critical and stressful moments of their PhDs. Lastly, I truly cannot express how grateful I am for the existence of the Academic Development Unit (NDA) at IST and for the incredible, high-quality service they offer. The final years of my PhD would have looked very different without the academic coaching sessions I attended with Patrícia Simões, and I'm forever grateful for her help and for the fully personalized and effective tool set I acquired.

Stepping outside the institutions (which I occasionally did), I have also benefited from generous support from my family and friends. I know it has seemed never-ending and repetitive, so thank you for being present through these years. Love and gratitude to Bonsai, Hans, Diogo, Johnny, Bia, Paula, Analu, Clara and José Lopes.

One last, very special friend is missing. My partner has often rowed the boat when I couldn't, even when it had holes and through stormy seas. Thank you, Victor, for your unshakeable support, patience and love. I can't believe this long-distance thing worked out.

Thank you to my village!

Resumo

A aceleração baseada em plasma (ABP) poderá reduzir significativamente a dimensão e/ou o custo dos colisores de partículas, que têm sido instrumentais para obter descobertas fundamentais na física e cujos limites técnicos se está a tornar cada vez mais dispendioso desafiar. Os conceitos de ABP dependem frequentemente da capacidade de manipular interações complexas entre feixe e plasma. Num desses conceitos, direcionado a aplicações na física de alta energia e que está a ser testado na experiência AWAKE no CERN, a onda de plasma usada para aceleração é impelida por um feixe de partículas longo e altamente energético. Neste caso as interações em causa são as instabilidades de hosing e de auto-modulação. A instabilidade de auto-modulação (IAM) pode ser utilizada para produzir campos de esteira (wakefields) de alta amplitude a partir de um feixe longo, que de outra forma não seria adequado para excitar a onda de plasma. A instabilidade de hosing (IH) é indesejada, porque pode deteriorar o feixe e a estrutura do campo de esteira.

Nesta dissertação, começamos por rever e alargar a teoria que descreve estas instabilidades. Utilizamos simulações particle-in-cell com o código OSIRIS para testar a robustez da IAM, especialmente após a sua saturação, a flutuações das condições iniciais. A dependência das taxas de crescimento da IH e da IAM da frequência de perturbação é determinada para um regime adiabático e um regime inicial. Durante este regime inicial, mostramos que ambas as instabilidades podem ser interpretadas como osciladores harmónicos forçados, e que é possível controlar o seu crescimento ao "desafinar"a oscilação do plasma em resposta a uma perturbação do envelope (IAM) ou do centroide (IH) do feixe suficientemente cedo. No caso da IAM revelamos ainda um fenómeno de ressonância sub-harmónica. Todos estes resultados são validados com simulações. Esta nova compreensão do crescimento de instabilidades feixe-plasma pode ter implicações importantes para os aceleradores baseados em plasma.

Palavras-chave: aceleração baseada em plasma, instabilidade de plasma, teoria de campos de esteira (*wakefields*), ressonância sub-harmónica, simulações *particle-in-cell*/PIC

Abstract

Plasma-based acceleration (PBA) could dramatically reduce the size and/or cost of particle colliders, which have been at the forefront of fundamental discoveries in physics, and whose technical limits it is becoming increasingly costly to push. The success of PBA schemes often relies on the ability to manipulate complex beam-plasma interactions. One such concept, which is geared towards high-energy-physics applications (implying long propagation distances and high final energies), is a single-stage plasma wakefield accelerator driven by a long, highly energetic particle bunch, and is being tested at the AWAKE facility at CERN. In this case, the key interactions are the symmetric and asymmetric modes of the transverse two-stream instability, called self-modulation and hosing, respectively. The self-modulation instability (SMI) can be harnessed to produce high-amplitude wakefields from a long driver, which would otherwise be unfit to excite a plasma wave. The hosing instability (HI) is undesirable due to its potential disruption of the bunch and wakefield structure.

In this dissertation, we first review and extend the theory that describes both instabilities. Particle-in-cell simulations with the code OSIRIS are used to test the robustness of the SMI, particularly after its saturation, to input parameter fluctuations. The dependence of the HI and SMI growth rates on an arbitrary perturbation frequency is determined for an adiabatic and an early-phase regime, which is particular interesting. During the latter, we show that both instabilities can be understood as driven harmonic oscillators, and that it is possible to control their growth rates by detuning the oscillating plasma response to either a bunch radius (SMI) or centroid (HI) perturbation early enough. For the SMI, in particular, we discover a phenomenon of subharmonic resonance. All of these results are validated with simulations. This novel understanding of the growth of beam-plasma instabilities could have important implications for plasma-based accelerators.

Keywords: plasma-based acceleration, plasma instability, wakefield theory, subharmonic resonance, particle-in-cell/PIC simulations

Contents

List of Tables

List of Figures

Chapter 1

Introduction

1.1 What are particle accelerators good for?

The most general association when the topic of particle accelerators is brought up is with high-energy physics. Monumental engineering projects like the Large Hadron Collider (LHC) at the European Organization for Nuclear Research (CERN) cannot fail to capture the general public's attention. Nevertheless, the vast majority of the roughly 30.000 existing particle accelerators worldwide are not used for the advancement of science, but for semiconductor manufacturing, radioisotope production, sterilization of food or medical equipment, plastics manufacturing, medical imaging, or cancer treatment, among others [1]. The remaining 3% of accelerators with non-commercial purposes constitute crucial but expensive tools for materials science, biochemistry, and, like the LHC, high-energy physics.

The engineering underlying these machines has made extraordinary progress during the last century, but we are reaching a technical limit of the order of 100 MV/m in the acceleration gradient [2, 3], which means that the acceleration length must be extended in order to reach a higher final energy. In the case of circular accelerators, higher energies can also translate into higher inertia (due to relativistic mass increase), which makes it necessary to use higher magnetic fields to bend the particles into a circular trajectory. Despite the technological breakthrough of superconducting magnets, there is no prospect of reaching magnetic fields beyond the tens of Teslas [4].

Due to these limitations, high-energy-physics projects focused on exploring physics at the energy frontier have been forced to scale up the size and cost of their proposed machines, such as the LHC (in operation, circumference of 27 km , construction cost of roughly €3 billion [5]), the Future Circular Collider (under study, circumference of 100 km, budget of €11.8 billion [6]), or the International Linear Collider (under study, length of 31 km, budget of almost €10 billion [7]).

1.2 What is plasma-based acceleration?

The current limitation on the acceleration gradient is due to the breakdown of the materials that make up the accelerating elements in conventional machines (radiofrequency cavities) when subject to a high enough surface electric field. The first idea to use plasma for particle acceleration was put forward in 1979, which consisted of letting a laser pulse drive a plasma wave and accelerating trapped electrons in the ensuing fields [8]. The great promise behind this idea lies in the fact that an ionized gas, i.e., plasma, is beyond material breakdown, and can thus sustain extremely high electromagnetic fields.

Plasma waves, which consist of fluctuations of the plasma electron density and are therefore associated with co-propagating electrostatic fields, provide the structure required to contain the particles we wish to accelerate. In a cold plasma, and approximating the much heavier plasma ions as an immobile, homogeneous positive background, such a wave can be produced by disturbing the plasma electrons, which naturally oscillate at the plasma frequency $\omega_p = \sqrt{e^2 n_0/\varepsilon_0 m_e}$, where e is the elementary charge, n_0 is the plasma electron density, ε_0 is the vacuum permittivity, and m_e is the electron mass.

An estimate of the maximum electric field sustainable by a plasma wave is given by the cold, non-relativistic wavebreaking limit $E_0 = m_e c \omega_p / e \approx 96\sqrt{n_0[\mathrm{cm}^{-3}]}\ [\mathrm{V/m}]$, where c is the speed of light. For a plasma density of $n_0 = 10^{18}\ \mathrm{cm}^{-3}$, for example, the wavebreaking field is almost 100 GV/m, i.e., three orders of magnitude higher than currently feasible acceleration gradients. Plasma-based acceleration therefore represents a thrilling opportunity for more compact and/or cost-effective particle accelerators.

1.3 Where does the field stand?

Since the first scheme for plasma-based acceleration driven by a laser pulse, commonly referred to as Laser Wakefield Acceleration (LWFA), was proposed, the field has blossomed into a variety of different configurations and potential applications. A plasma wave may equally be driven by a beam of charged particles, in which case it is commonly called Plasma Wakefield Acceleration (PWFA) [9, 10]. Several experimental milestones have been reached in both broader categories, and occasionally even using both kinds of drivers [11].

Advances in the use of plasma as a waveguide for extremely intense (petawatt-level) laser pulses have allowed the demonstration of electron acceleration up to 7.8 GeV in 20 cm (i.e., an acceleration gradient of almost 40 GV/m) [12]. The strength of LWFA setups is indeed access to extremely high acceleration gradients, albeit for limited propagation lengths in plasma, since these setups typically contend with driver divergence, witness dephasing, and driver depletion (for ultrashort laser pulses with current technology). In order to reach interesting final energies for a future lepton collider, for example, it would be necessary to couple several LWFA stages, the principle of which has already been proved experimentally [13].

Staging nevertheless remains a significant technical challenge, which, coupled with the very low wallplug efficiency of LWFA driven by short intense pulses [14], makes laser-driven schemes less attractive for high-energy-physics applications from this point of view. By contrast, PWFA experiments have demonstrated energy-transfer efficiencies (from the plasma to the accelerated bunch) of 30–40% [15, 16]. In fact, recent experimental efforts suggest that it may be possible to operate a beam-driven plasma accelerator with a wallplug efficiency of 13% [17], which is similar to current conventional accelerators. Moreover, relativistic particle bunches often carry more energy than laser pulses and propagate approximately at c, which delays driver depletion and avoids dephasing. The AWAKE experiment uses 400-GeV proton bunches, which contain almost 20 kJ of energy, to demonstrate single-stage, plasma-based acceleration for high-energy-physics applications [18, 19]. During its Run 1, electrons were accelerated to 2 GeV in proton-driven wakefields along a ten-meter-long plasma [20].

A beam driver has also been used to accelerate positrons in plasma [21], which remains one of the most challenging components for a potential plasma-based electron-positron collider. An energy-frontier lepton collider is most efficient in the form of a linear machine, since lighter particles radiate away much more energy on a bent trajectory than heavier particles (such as hadrons), and

thus stands to gain the most from a high acceleration gradient, which can make it more compact. The luminosity required for such high-energy-physics facilities poses an additional challenge, which part of the community has begun to tackle by measuring the minimum recovery time of a perturbed plasma and estimating an upper repetition rate limit of the order of MHz [22].

1.4 The pursuit of accelerated bunch quality

Besides the challenges already mentioned, the potential of plasma-based acceleration cannot be fulfilled without demonstrating a high degree of accelerated bunch quality, which typically comprises high bunch charge, low or preserved emittance, and low energy spread. At the time of writing, experimental results undergoing peer review appear to successfully demonstrate PWFA where the emittance, charge, and energy spread of an injected bunch has been preserved [23]. Nevertheless, bunch quality continues to be the crucial concern for most regimes and configurations of plasma-based acceleration.

The **emittance** of a particle bunch can be preserved as long as the focusing field acting on it grows linearly along the transverse direction. This is the case for plasma wakefields in the blowout regime [24, 25], where the driver is dense or intense enough to expel all plasma electrons in its path, instead of merely perturbing the plasma electron density, as in the linear regime ($\delta n/n_0 \ll 1$, where δn is the plasma density perturbation). In any regime, however, the emittance may be increased due to undesirable interactions between the bunch and the plasma, such as streaming instabilities or the hosing instability (see Ch. 3).

In both the linear and nonlinear ($\delta n/n_0 \gtrsim 1$) wakefield regimes, the (non-constant) profile of the longitudinal wakefields E_z within each wake period inevitably imprints some **energy spread** on a trapped bunch. This can be circumvented with beam loading [26], i.e., by accelerating enough particles that their collective charge is able to flatten E_z locally. This effect applies both to linear [27] and nonlinear wakefields [28, 29]. The benefits of beam loading can be maximized by shaping the accelerated bunch into an optimal profile [26, 28], which has been demonstrated experimentally in beam-driven nonlinear wakefields, using conventional techniques to prepare the injected bunch [30]. In this regime, however, the injected bunch most commonly consists of plasma electrons that become trapped in the “bubble” behind the driver and are subsequently accelerated. There are several techniques to control this so-called self-injection, mostly by changing the plasma profile or properties. It is therefore also possible to tailor the shape of a self-injected bunch for beam loading and to obtain low energy spreads, as has been accomplished experimentally for LWFA [31, 32], most recently with the help of machine learning techniques [33, 34].

Alternatively, since E_z is approximately independent of the transverse coordinate in the blowout regime [24, 25], the imparted energy spread can be considered correlated with the longitudinal coordinate. It may be possible to reach sub-0.1% energy spreads using additional plasma sections to “dechirp” a bunch with such a correlated energy spread, for example by rotating its phase space between two sections [35], and it may even be possible to form a self-correcting mechanism by chaining several of these configurations (plasma, magnetic chicane, plasma) [36].

Despite the outstanding challenges, progress on the bunch quality front has reached an extremely important milestone in 2023. Two separate groups experimentally demonstrated free-electron lasing using electron bunches accelerated in plasma (via LWFA [37] and PWFA [38]), thereby asserting the suitability of plasma-based sources for such applications.

1.5 What are the hosing and self-modulation instabilities?

The work discussed in this doctoral dissertation is oriented toward the AWAKE experiment, which seeks to demonstrate the acceleration of an electron bunch over a long distance in plasma wakefields driven by a relativistic proton bunch. The experimental setup for the AWAKE Run 1 measurement campaign is shown in Fig. 1.1. The experiment's goal is to produce an electron beam with enough quality to be suitable for high-energy-physics applications.

The driver is a 400-GeV proton bunch with a length of 6–12 cm, which is far longer than the typical lengths where plasma wakefields reach interesting amplitudes. At the nominal plasma density in AWAKE, $n_0 = 7 \times 10^{14}\ \mathrm{cm}^{-3}$, $E_0 \approx 2.5\ \mathrm{GV/m}$ and the plasma wavelength, defined as $\lambda_p = 2\pi c/\omega_p$, is roughly 1.26 mm. A plasma wave is most effectively excited when there is a density perturbation at the time scale of the plasma period ω_p^{-1}, or, equivalently, at the length scale of λ_p. A long driver can therefore only generate modest wakefields. However, the same driver is long enough to sustain several periods of the forces associated with these wakefields, in particular their transverse component (for a highly relativistic bunch). Both the hosing and self-modulation instabilities are a result of the interaction between the long driver and the transverse wakefields.

In the linear regime, where the bunch density n_b is smaller than the plasma density ($n_b < n_0$), the wakefields oscillate harmonically along the co-moving coordinate $\zeta = z - ct$ at the natural plasma wavenumber $k_p = \omega_p/c$. For a driver that is perfectly axisymmetric with respect to the propagation axis z, the transverse component of the wakefields gradually acts on the driver particles, periodically focusing and defocusing them until a train of "bunchlets" sized and spaced at approximately λ_p is eventually formed [see Fig. 1.2b)]. The more the initially long, smooth bunch profile acquires this train structure, the more the plasma wave is excited at its natural frequency ω_p, and the higher the amplitude of the generated wakefields. This resonant feedback loop constitutes the **self-modulation instability**, leading to quasi-exponential growth of the wakefield amplitude.

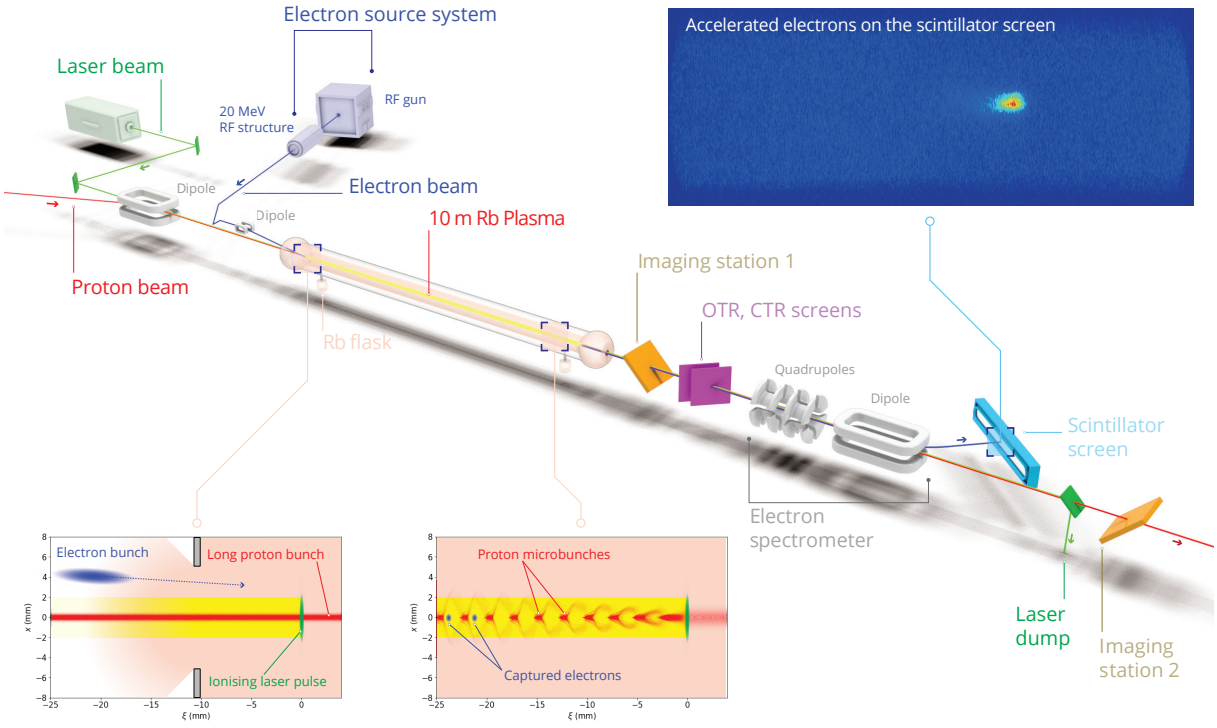

Figure 1.1: Schematic drawing of the AWAKE experiment's setup for its Run 1.

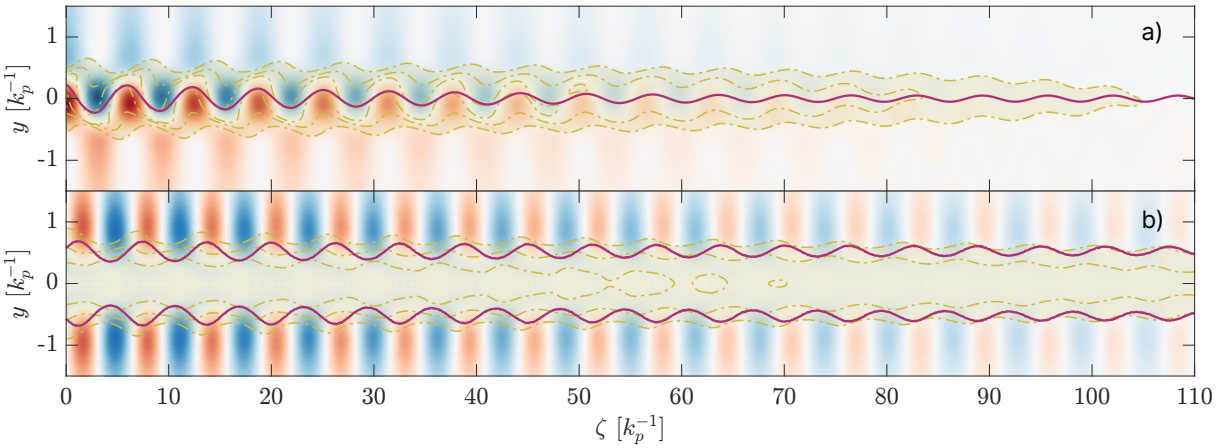

Figure 1.2: Illustrative representation of the hosing (a) and self-modulation (b) instabilities. The transverse component of the wakefields is shown as a blue-to-red color scale, the bunch distributions as yellow-shaded areas outlined by dash-dotted contours, and the centroid (a) and RMS envelope (b) as thick solid red lines. The bunches propagate from left to right.

A saturation phase of the instability is eventually reached, in part because all the bunch charge located in defocusing regions has been lost [see Fig. 4.22a) on p. 76].

The **hosing instability** can be explained by the same mechanism, with the exception that there is no axisymmetry, which is the case for a bunch propagating with a tilt relative to the z-axis. This asymmetry translates into uneven focusing or defocusing forces around the axis [see Fig. 1.2a)], which in turn exacerbate the initial asymmetry. Once again, since the wakefields oscillate at k_p along ζ, the upshot is an oscillating bunch centroid with a wavelength of λ_p and with growing amplitude along both ζ and the propagation distance z, leading to significant emittance growth.

Note that many forms of the HI exist, depending on the conditions of the bunch and accelerating structure. An overview is shown in Table 1.1, where L_b denotes the longitudinal bunch size and λ_{Np} is the nonlinear plasma wavelength [24]. Note that the terms “overdense” and “underdense” are used interchangeably with “linear” and “nonlinear”, respectively. In the following, we will concern ourselves exclusively with the strongly-coupled, overdense, long-bunch facet of the HI (and SMI, for that matter).

Since the hosing and self-modulation instabilities are dictated by the transverse dynamics of the bunch particles, their evolution time scale is tied to the betatron period. The betatron frequency is defined as $\omega_\beta = \omega_b/\sqrt{2\gamma_b} = \sqrt{n_{b0}q_b^2/(\varepsilon_0 M_b)}/\sqrt{2\gamma_b}$, where n_{b0} is the peak bunch density, and γ_b, q_b and M_b are the Lorentz factor, charge and mass of the bunch particles, respectively. The

Table 1.1: Overview of the different regimes of hosing-type instabilities in accelerators.

In terms of …	Regime	Meaning	Examples
Time/space scales of instability growth and beam evolution	weakly coupled	betatron motion cannot be neglected during growth of instability	conventional accelerators (beam break-up inst. [39])
	strongly coupled	growth of instability much faster than betatron period	plasma-based accelerators
Plasma and beam density	overdense	$n_b < n_0$	AWAKE [18, 40]
	underdense	$n_b > n_0$	FLASHForward [41]
Bunch length and plasma wavelength	short bunch	$L_b \sim \lambda_p$ or $L_b \sim \lambda_{Np}$	FLASHForward [41]
	long bunch	$L_b \gg \lambda_p$	AWAKE [18, 40]

growth of both instabilities has a spatiotemporal character, i.e., it is a function of both ζ and z (or t). Growth rates can be obtained with asymptotic methods [42, 43], which presuppose a long-bunch, early-time approximation (see Eq. 2.118 on p. 34). These growth rates are discussed in more detail in Sec. 2.3.3. Since they are similar for both instabilities, hosing and self-modulation may develop at the same time and couple to each other [43], or one may dominate over the other if the seeding levels are disparate enough [44, 45].

1.6 Which questions are addressed in this dissertation?

The overarching goal of this work is to expand the fundamental knowledge about two specific beam-plasma instabilities, thereby contributing to a successful demonstration of plasma-based acceleration (be it along the particular avenue represented by AWAKE or along other avenues).

Each chapter aims to answer the following questions.

- Chapter 2: *Theoretical models for the hosing and self-modulation instabilities*
  - What theoretical models exist to describe the HI and SMI?
  - What is the mathematical scaffolding behind existing models?
  - Under which conditions are these models valid?
  - Is it possible to model the early growth phase of these instabilities?
- Chapter 3: *Properties of the hosing instability*
  - Can the hosing instability grow at wavelengths other than the plasma wavelength?
  - Is it possible to mitigate hosing in the linear/overdense, long-bunch regime?
- Chapter 4: *Properties of the self-modulation instability*
  - Is the SMI robust to fluctuations of the input parameters after saturation?
  - Does self-modulation grow at wavelengths other than the plasma wavelength?
  - How can the development of the SMI be influenced using plasma density steps?

1.7 Methods

The doctoral work was partly conducted at the Group of Lasers and Plasmas of *Instituto de Plasmas e Fusão Nuclear* (IPFN) at *Instituto Superior Técnico* – University of Lisbon and partly at the European Organization for Nuclear Research (CERN). The results presented in this dissertation were obtained using analytical methods, numerical computation, and numerical simulations based on the particle-in-cell (PIC) method. The latter were performed with the code OSIRIS [46], with the support of several supercomputing grants (see Acknowledgments).

OSIRIS is a fully relativistic, massively parallel PIC code developed and maintained by the Osiris consortium, which consists of the Extreme Plasma Physics (EPP) team in the Group of Lasers and Plasmas and the Particle-in-Cell and Kinetic Simulation Software Center (PICKSC) at University of California, Los Angeles.

The PIC method is a computationally intensive particle-tracking simulation method, which uses a grid to compute the electromagnetic fields caused by, and acting on, the simulation macroparticles. These macroparticles represent averaged ensembles of real particles. The loop executed at each

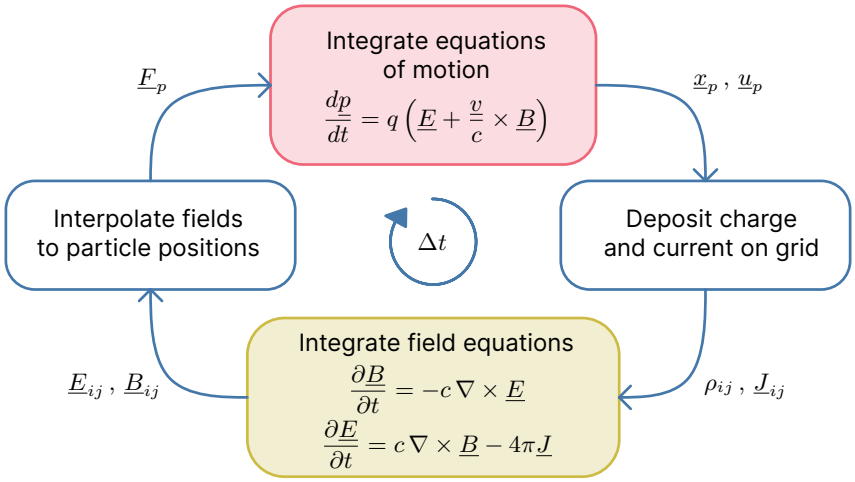

Figure 1.3: Diagram of each iteration of the particle-in-cell simulation method. The p-index denotes a macroparticle, while the indices ij refer to the grid coordinates. The orange and green boxes represent the particle pusher and field solver components of the loop, respectively.

iteration of a PIC simulation is represented in Fig. 1.3. Many algorithmic choices are available for each step of the loop.

The most common discretization of the relativistic equations of motion is the finite-difference, time-centered Boris algorithm [47]. Current deposition schemes typically rely on some order of splines (the default order in OSIRIS is quadratic), though it is essential to ensure that the total charge (and Gauss's law) is conserved. The field equations can be solved with a variety of approaches, though the Yee solver [48] (a finite-difference time-domain scheme with second-order central difference) is the most widespread.

At the beginning of each simulation, a particle species must be initialized according to some density distribution. Care must be taken to accurately translate this input into a distribution of discrete, ensemble-representing macroparticles, while ensuring that low-density regions are sufficiently represented statistically. In OSIRIS, the number of particles per cell is initially fixed and a unique weight is attributed to each macroparticle, such that the overall distribution matches the input distribution. After $t = 0$, the macroparticles are allowed to cross cell boundaries and move freely.

Though OSIRIS includes many useful advanced modules, the work in this dissertation requires only a few basic capabilities. Besides massive parallelization, we have made use of the 2D, 3D and 2D axisymmetric geometries, and of the field initialization for a charged particle beam.

Chapter 2

Theoretical models for the hosing and self-modulation instabilities

In this chapter, we will provide an overview of the theory available to describe the hosing and self-modulation instabilities. This overview will include existing work (accompanied by the respective reference) as well as original contributions.

Although the HI and SMI are mathematically and physically closely related (as we shall see), the components of the existing theory for these instabilities are scattered in different publications. In addition, due to the size constraints associated with scientific publications (understandably), pivotal details for the derivation of these theoretical components are often omitted. For these reasons, and since the calculations behind this theoretical apparatus at times require some nontrivial mathematical sleights of hand, we present a systematic derivation of some equations (both existing and original) that describe hosing and self-modulation.

2.1 Plasma response

In this dissertation, we will always consider the propagation of a relativistic charged-particle bunch in a cold plasma, where we neglect the motion of the plasma ions. The bunch densities considered are always smaller than the background plasma density ($n_b < n_0$), which means that we can use linear wakefield theory to describe the phenomena in question.

The wakefields generated in plasma in response to a particle bunch propagating along z under the above conditions are dictated by the wake potential equation, which can be derived from the cold plasma fluid and Maxwell equations (i.e., the continuity, fluid momentum, and Poisson equations). The normalized wake potential is defined as $\psi = \phi - a_z$, where $\phi = e\Phi/m_e c^2$ and $\underline{a} = e\underline{A}/m_e c^2$ are the normalized versions of the electric potential Φ and magnetic vector potential $\underline{A}$, respectively (note that vector quantities are denoted by an underline). In the following, we use the bunch co-moving coordinate $\zeta = z - ct$, or its normalized equivalent $\hat{\zeta} = k_p \zeta$ (denoted by a "hat" sign). The differential equation for the normalized wake potential is

$$(\partial_\zeta^2 + 1)(\nabla_\perp^2 - 1)\,\psi = \frac{q_b}{e}\,\frac{n_b(\zeta, \underline{x}_\perp)}{n_0}\,, \tag{2.1}$$

where $\underline{x}_\perp$ are the transverse coordinates, $\nabla_\perp^2$ is the Laplace operator in $\underline{x}_\perp$, q_b is the charge of the bunch particles and $n_b(\zeta, \underline{x}_\perp)$ is the bunch density distribution [9, 10]. The distance quantities in Eq. 2.1 (ζ and $\underline{x}_\perp$) are normalized to the plasma skin depth k_p^{-1}, although the hat notation is

ommitted. This will generally be the case for distance quantities in all the equations mentioned throughout this dissertation unless otherwise stated. As an example, the coordinate ζ (assumed normalized) should be understood as $k_p\zeta$ in physical units, and the derivative $\partial/\partial y$ as $k_p^{-1}\partial/\partial y$.

The specific form of the transverse Laplace operator in Eq. 2.1 will depend on the geometry chosen to approach a problem. It is possible to obtain a general form of the solution for ψ as a function of the bunch distribution n_b for different geometries, using Green's functions. In the following, we will first establish a general form of the solution for the wake potential ψ using Green's functions, in which the specific Green's functions for different operators (in different geometries) can be later replaced.

Once the wake potential potential has been found, it can be translated into a force $\underline{F}$ acting on a relativistic particle with charge q_b:

$$\frac{\underline{F}}{eE_0} = -\frac{q_b}{e}\,\nabla\psi\ . \tag{2.2}$$

2.1.1 General Green's function solution for the wake potential

The Green's function method provides us with a general recipe for the solution to Eq. 2.1, where we can simply plug the bunch profile and choose an appropriate kernel function from a catalog that we have calculated beforehand.

Let us consider the following general equation, composed of two differential operators $\mathcal{L}_\zeta$ and $\mathcal{L}_\perp$ acting on the function $\psi(\zeta, \underline{x}_\perp)$, with the inhomogeneity $H(\zeta, \underline{x}_\perp)$, and where the variables ζ and $\underline{x}_\perp$ belong to the general domains $\mathbf{D}_\zeta$ and $\mathbf{D}_\perp$, respectively:

$$\mathcal{L}_\zeta\mathcal{L}_\perp\psi = H\ . \tag{2.3}$$

If we define a new function $\psi_\perp = \mathcal{L}_\perp\psi$, then we can write Eq. 2.3 as $\mathcal{L}_\zeta\psi_\perp = H$. The Green's function solution for $\psi_\perp$ can be determined by finding the Green's function that fulfills the equation $\mathcal{L}_\zeta G_\zeta(\zeta,\zeta') = \delta(\zeta-\zeta')$, where $\delta(x)$ is the Dirac delta distribution. The general solution for $\psi_\perp$ will then be:

$$\psi_\perp(\zeta, \underline{x}_\perp) = \int_{\mathbf{D}_\zeta} d\zeta'\, G_\zeta(\zeta',\zeta)\, H(\zeta', \underline{x}_\perp)\ . \tag{2.4}$$

Using our earlier definition, we can now use the same procedure to solve the equation $\mathcal{L}_\perp\psi = \psi_\perp$, substituting our solution for $\psi_\perp$. The general solution for ψ is therefore:

$$\psi(\zeta, \underline{x}_\perp) = \int_{\mathbf{D}_\perp} d\underline{x}'_\perp\, G_\perp(\underline{x}'_\perp, \underline{x}_\perp)\, \phi_\perp(\zeta, \underline{x}'_\perp) = \int_{\mathbf{D}_\perp}\int_{\mathbf{D}_\zeta} d\zeta' d\underline{x}'_\perp\, G_\perp(\underline{x}'_\perp, \underline{x}_\perp)\, G_\zeta(\zeta',\zeta)\, H(\zeta', \underline{x}'_\perp)\ , \tag{2.5}$$

where $G_\perp(\underline{x}_\perp, \underline{x}'_\perp)$ is the Green's function that fulfills the equation $\mathcal{L}_\perp G_\perp(\underline{x}_\perp, \underline{x}'_\perp) = \delta(\underline{x}_\perp - \underline{x}'_\perp)$. The general solution in Eq. 2.5 means that we can find the Green's function for each longitudinal or perpendicular operator and simply replace it, instead of having to solve the full Eq. 2.1 every time for a different geometry (i.e. for different versions of the operator $\nabla_\perp^2$).

Given a certain bunch distribution $n_b(\zeta, \underline{x}_\perp)$, we set $H(\zeta, \underline{x}_\perp) = n_b(\zeta, \underline{x}_\perp)$ in the general recipe Eq. 2.5 and obtain the solution for the wake potential in Eq. 2.1

$$\begin{aligned}\psi(\zeta, \underline{x}_\perp) &= \frac{q_b}{e}\int_{\mathbf{D}_\perp}\int_{\mathbf{D}_\zeta} d\zeta' d\underline{x}'_\perp\, G_\perp(\underline{x}'_\perp, \underline{x}_\perp)\, G_\zeta(\zeta',\zeta)\, \frac{n_b(\zeta', \underline{x}'_\perp)}{n_0} \\ &= -\frac{q_b}{e}\int_\zeta^\infty d\zeta' \sin(\zeta-\zeta')\int_{\mathbf{D}_\perp} d\underline{x}'_\perp G_\perp(\underline{x}'_\perp, \underline{x}_\perp)\, \frac{n_b(\zeta', \underline{x}'_\perp)}{n_0}\ ,\end{aligned} \tag{2.6}$$

where the appropriate transverse Green's function $G_\perp(\underline{x}'_\perp, \underline{x}_\perp)$ must be replaced depending on the

coordinate system being considered (see below).

Green's function for the longitudinal plasma operator

We want to find the Green's function for the operator $\mathcal{L}_\zeta = (\partial_\zeta^2 + 1)$. For $\zeta \in [0, \infty[$, and with the boundary conditions $\psi(\zeta \to \infty) = 0$ and $\partial_\zeta \psi(\zeta \to \infty) = 0$, it can be shown that the Green's function is [49]

$$G(\zeta, \zeta') = \begin{cases} 0 & \zeta < \zeta' \\ \sin(\zeta - \zeta') & \zeta \geq \zeta' \end{cases} . \tag{2.7}$$

Green's function for the transverse operator in cylindrical coordinates

In cylindrical coordinates (r, θ, z), the Laplace operator along the transverse dimensions reduces to $\nabla_\perp^2 = \partial_r^2 + \frac{1}{r}\partial_r$ for an axisymmetric (θ-independent) function. The transverse operator acting on the wake potential in Eq. 2.1 therefore becomes $\mathcal{L}_\perp = (\partial_r^2 + \frac{1}{r}\partial_r - 1)$. Since the Green's function is found by setting $\mathcal{L}_\perp G(r, r') = \delta(r - r') = 0$ for $r < r'$ and $r > r'$, we can multiply this equation by r^2 and find that it corresponds to the modified Bessel equation for $m = 0$ (see below), the solutions to which are known. For $r \in [0, \infty[$ and the boundary condition $\partial_r \psi|_{r\to\infty} = 0$, the Green's function is

$$G(r, r') = \begin{cases} -r\, I_0(r) K_0(r') & r < r' \\ -r\, I_0(r') K_0(r) & r \geq r' \end{cases} , \tag{2.8}$$

where $I_m(r)$ and $K_m(r)$ are the modified Bessel functions of the first and second kind, respectively.

The transverse Green's function can also be determined for a general, non-axisymmetric right-hand side (i.e. bunch distribution). In that case, the transverse Laplace operator is $\nabla_\perp^2 = \partial_r^2 + \frac{1}{r}\partial_r + \frac{1}{r^2}\partial_\theta$. Given that the equation we wish to solve is $\mathcal{L}_\perp \psi = H$, let us assume that we can write the azimuthal dependence of the inhomogeneity as a cosine series $H(r, \theta) = \sum_{m=0}^{\infty} \hat{H}_m(r) \cos(m\theta)$. Due to the orthogonality of the cosine modes, the solution must also be a cosine series $\psi(r, \theta) = \sum_{m=0}^{\infty} \hat{\psi}_m(r) \cos(m\theta)$. If we apply the transverse operator $\mathcal{L}_\perp = (\partial_r^2 + \frac{1}{r}\partial_r + \frac{1}{r^2}\partial_\theta - 1)$ to $\psi(r, \theta)$, using the fact that $\partial_\theta^2 \cos(m\theta) = -m^2 \cos(m\theta)$, we will have to solve the following differential equation for each independent mode m:

$$\left(\partial_r^2 + \frac{1}{r}\partial_r - \frac{m^2}{r^2} - 1\right) \hat{\psi}_m(r, \zeta) = \hat{H}_m(r, \zeta) . \tag{2.9}$$

As mentioned before, the Green's function for this operator is found by setting $\big(\partial_r^2 + \frac{1}{r}\partial_r - \frac{m^2}{r^2} - 1\big) G(r, r') = 0$ for $r < r'$ and $r > r'$, and therefore we once again multiply the equation by r^2 and arrive at the generalized modified Bessel equation: $\big[r^2\partial_r^2 + r\,\partial_r - (r^2 + m^2)\big] G(r, r') = 0$. For the same domain and assuming the same boundary condition as before, $r \in [0, \infty[$ and $\partial_r \hat{\psi}_m|_{r\to\infty} = 0$, the Green's function for each mode is

$$G(r, r') = \begin{cases} -r\, I_m(r) K_m(r') & r < r' \\ -r\, I_m(r') K_m(r) & r \geq r' \end{cases} . \tag{2.10}$$

Green's function for the transverse operator in 2D Cartesian coordinates

Further along this dissertation, we will consider a simplified Cartesian geometry with only one transverse dimension, so that the overall problem is two-dimensional in (z, y) or (ζ, y). In this

case, the transverse Laplace operator is simply $\nabla_\perp^2 = \partial_y^2$, and we find the Green's function for the operator $(\partial_y^2 - 1)$. For $y \in]-\infty, \infty[$, and with the condition $\partial_y \psi|_{y\to 0} = 0$, the Green's function is

$$G(y, y') = \begin{cases} -\frac{1}{2}\, e^{-y'} e^{y} & y < y' \\ -\frac{1}{2}\, e^{-y} e^{y'} & y \geq y' \end{cases} . \tag{2.11}$$

2.2 Differential equations

For the following derivations, we start from the equation of motion for a single particle with mass M_b propagating relativistically along the z axis with a Lorentz factor γ. By assuming that the longitudinal velocity of the particle is constant and approximately equal to the speed of light ($v_z \approx c$), we may substitute the derivative in time (t) with a spatial one according to $\frac{d}{dt} = c\, \frac{d}{dz}$:

$$\frac{d(\gamma m \underline{v})}{dt} = \underline{F} \quad \Leftrightarrow \quad \frac{d\underline{v}}{dz} = \frac{\underline{F}}{\gamma M_b c} \quad \Leftrightarrow \quad \frac{d^2\underline{x}}{dz^2} = \frac{\underline{F}}{\gamma M_b c^2} , \tag{2.12}$$

where $\underline{x}$ and z are **not** normalized. Here, $\underline{x}$ and $\underline{v}$ are the position and velocity of the particle, respectively, and $\underline{F}$ is any force acting on it. We may now normalize the distance quantities $\underline{x}$ and z to the plasma skin depth $k_p^{-1} = c/\omega_p$. We therefore replace the normalized $\hat{\underline{x}} = \underline{x}\, k_p$ and $d/dz = k_p\, d/d\hat{z}$, and recast the equation such that a natural normalization for $\underline{F}$ appears:

$$\frac{d^2\hat{\underline{x}}}{d\hat{z}^2} = \frac{1}{\gamma\, M_b} \frac{\underline{F}}{c\, \omega_p} = \frac{m_e}{\gamma\, M_b} \frac{\underline{F}}{e E_0} = \frac{m_e}{\gamma\, M_b} \hat{\underline{F}} , \tag{2.13}$$

where $E_0 = m_e c \omega_p / e$ is the wavebreaking field. For simplicity, the hat symbol characterizing normalized quantities will be omitted henceforth.

The density profile of the bunch is defined as $n_b(\zeta, \underline{x}_\perp) = n_{b0} \cdot f(\zeta) \cdot g(\underline{x}_\perp, \zeta)$, where n_{b0} is the peak density and f and g are the normalized longitudinal and transverse profiles, respectively. The transverse profile may depend explicitly on the longitudinal coordinate ζ via the bunch centroid or radius. Lastly, and since we will require this later on, we note that the average over the transverse bunch profile is defined as

$$\langle \bullet \rangle = \frac{\int \bullet\, n_b(\zeta, \underline{x}_\perp)\, d\underline{x}_\perp}{\int n_b(\zeta, \underline{x}_\perp)\, d\underline{x}_\perp} . \tag{2.14}$$

2.2.1 Centroid (HI)

The hosing instability results from the misalignment between the propagation axis of a particle bunch and the transverse wakefields. This misalignment ultimately leads to an oscillating bunch centroid, which feeds back into the wakefield asymmetry and thus forms an instability. Hosing can be described by setting up an equation for the bunch centroid. We simply take Eq. 2.13 (for a single bunch particle), and average it transversely over the bunch distribution. A final form of the differential equation for the centroid will therefore depend on the choice of coordinate system and on the transverse profile of the bunch.

We choose the transverse dimension y to set up the centroid equation (i.e., across which the centroid will oscillate). Taking the transverse average $\langle \bullet \rangle$ of the y component of Eq. 2.13, and defining the centroid $y_c = \langle y \rangle$, we obtain the differential equation for the bunch centroid

$$\frac{d^2 y_c}{dz^2} = \frac{m_e}{\gamma M_b} \langle F_y \rangle . \tag{2.15}$$

The transverse force due to the plasma response can be found by taking the transverse average over the y component of Eq. 2.2:

$$\langle F_y \rangle = -\frac{q_b}{e} \, \langle \partial_y \psi \rangle \ . \tag{2.16}$$

In the following, we will determine the specific form of the right-hand side of Eq. 2.15 for different geometries and transverse bunch profiles.

2D Cartesian, flat-top transverse profile

The right-hand side of the centroid differential equation (Eq. 2.16) consists of several chained integrals, which is why we begin by considering the simplest function possible for the transverse bunch profile $g(y, \zeta, z)$. Let us define

$$g(y, \zeta, z) = \frac{y_e(\zeta, 0)}{y_e(\zeta, z)} \, \Theta\big[y_e(\zeta) - |y - y_c(\zeta)|\big] \ , \tag{2.17}$$

where $y_e(\zeta, z)$ is the bunch envelope and $\Theta(x)$ is the Heaviside step function. This profile corresponds to a flat top with an evolving bunch radius where the charge per slice is conserved (see Fig. 2.1). In 2D Cartesian geometry, the wake potential has the solution (replace the Green's functions Eq. 2.7 and 2.11 in Eq. 2.5)

$$\psi(\zeta, y) = \frac{q_b}{e} \, \frac{n_{b0}}{n_0} \int_\zeta^\infty d\zeta' \sin(\zeta - \zeta') f(\zeta') \underbrace{\int_{-\infty}^\infty dy' \left(-\tfrac{1}{2}\right) \, e^{-y_>} \, e^{y_<} \, g(y', \zeta')}_{\tau(y, \zeta')} \ , \tag{2.18}$$

where the function $\tau(y, \zeta')$ has been defined for convenience. Using Eq. 2.16, the average transverse force is therefore given by

$$\langle F_y \rangle = -\left(\frac{q_b}{e}\right)^2 \, \frac{n_{b0}}{n_0} \int_\zeta^\infty d\zeta' \sin(\zeta - \zeta') f(\zeta') \, \langle \partial_y \tau(y, \zeta') \rangle \ . \tag{2.19}$$

For the sake of brevity, the independent variables of the beam envelope will be omitted in the following calculations: $y_e \equiv y_e(\zeta', z)$ and $y_{e0} \equiv y_e(\zeta', z = 0)$. The derivative of the transverse part of the solution for the wake potential $\tau(y, \zeta')$ can be simplified using the product rule and the first fundamental theorem of calculus:

$$\partial_y \tau(y, \zeta') = -\frac{1}{2} \, \partial_y \left[e^{-y} \int_{-\infty}^y dy' \, e^{y'} \, g(y', \zeta') + e^y \int_y^\infty dy' \, e^{-y'} \, g(y', \zeta') \right]$$

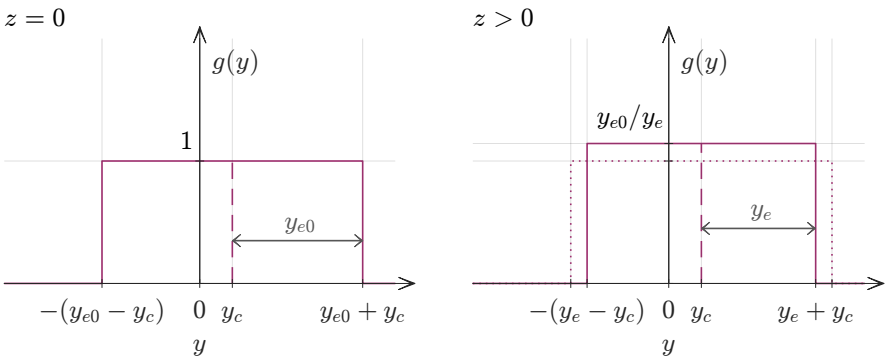

Figure 2.1: Flat-top transverse profile along y in Cartesian coordinates for a bunch with a centroid $y_c(\zeta, z)$ and an envelope $y_e(\zeta, z)$ (Eq. 2.17) at two different times. Note that y_{e0} corresponds to $y_e(\zeta, z = 0)$.

$$
\begin{aligned}
&= -\frac{1}{2}\left[-e^{-y}\int_{-\infty}^{y} dy'\, e^{y'}\, g(y',\zeta') + e^{-y}\,\partial_y\left(\int_{-\infty}^{y} dy'\, e^{y'}\, g(y',\zeta')\right)\right. \\
&\quad \left. + e^{y}\int_{y}^{\infty} dy'\, e^{-y'}\, g(y',\zeta') - e^{y}\,\partial_y\left(\int_{\infty}^{y} dy'\, e^{-y'}\, g(y',\zeta')\right)\right] \\
&= -\frac{1}{2}\left[-e^{-y}\int_{-\infty}^{y} dy'\, e^{y'}\, g(y',\zeta') + g(y,\zeta') + e^{y}\int_{y}^{\infty} dy'\, e^{-y'}\, g(y',\zeta') - g(y,\zeta')\right] \\
&= -\frac{1}{2}\left[-e^{-y}\int_{-\infty}^{y} dy'\, e^{y'}\, g(y',\zeta') + e^{y}\int_{y}^{\infty} dy'\, e^{-y'}\, g(y',\zeta')\right] .
\end{aligned}
\tag{2.20}
$$

Once the transverse profile is replaced, we obtain

$$
\begin{aligned}
\partial_y \tau(y,\zeta') &= -\frac{1}{2}\,\frac{y_{e0}}{y_e}\left[e^{y}\int_{y}^{y_e+y_c(\zeta')} dy'\, e^{-y'} - e^{-y}\int_{-y_e+y_c(\zeta')}^{y} dy'\, e^{y'}\right] \\
&= \frac{1}{2}\,\frac{y_{e0}}{y_e}\left(e^{y-y_c(\zeta')-y_e} - e^{-y+y_c(\zeta')-y_e}\right) .
\end{aligned}
\tag{2.21}
$$

Finally, it is necessary to take the average over the transverse profile $g(y,\zeta,z)$ of the expression $\partial_y\tau(y,\zeta')$. Applying the flat-top profile to the general definition in Eq. 2.14, we may simplify to:

$$
\begin{aligned}
\langle \partial_y \tau(y,\zeta')\rangle &= \frac{n_{b0}\, f(\zeta)\displaystyle\int_{-\infty}^{\infty} dy\, g(y,\zeta)\,\partial_y\tau(y,\zeta')}{n_{b0}\, f(\zeta)\displaystyle\int_{-\infty}^{\infty} dy\, g(y,\zeta)} = \frac{\dfrac{y_e(\zeta)}{y_{e0}(\zeta)}\displaystyle\int_{-y_e(\zeta)+y_c(\zeta)}^{y_e(\zeta)+y_c(\zeta)} dy\,\partial_y\tau(y,\zeta')}{\dfrac{y_e(\zeta)}{y_{e0}(\zeta)}\displaystyle\int_{-y_e(\zeta)+y_c(\zeta)}^{y_e(\zeta)+y_c(\zeta)} dy} \\
&= \frac{1}{2\, y_e(\zeta)}\int_{-y_e(\zeta)+y_c(\zeta)}^{y_e(\zeta)+y_c(\zeta)} dy\,\partial_y\tau(y,\zeta') .
\end{aligned}
\tag{2.22}
$$

We may now replace Eq. 2.21 and obtain $\langle\partial_y\tau(y,\zeta')\rangle$, being careful to retain the different dependences on ζ and ζ'.

$$
\begin{aligned}
\langle \partial_y \tau(y,\zeta')\rangle &= \frac{1}{4}\,\frac{y_{e0}(\zeta')}{y_e(\zeta)\, y_e(\zeta')}\int_{-y_e(\zeta)+y_c(\zeta)}^{y_e(\zeta)+y_c(\zeta)} dy\,\left(e^{y-y_c(\zeta')-y_e(\zeta')} - e^{-y+y_c(\zeta')-y_e(\zeta')}\right) \\
&= \frac{\sinh(y_e(\zeta))}{y_e(\zeta)}\, e^{-y_e(\zeta')}\,\frac{y_{e0}(\zeta')}{y_e(\zeta')}\,\sinh(y_c(\zeta)-y_c(\zeta')) ,
\end{aligned}
\tag{2.23}
$$

where $\sinh(x) = \frac{1}{2}(e^x - e^{-x})$ is the hyperbolic sine function. This latest equation provides the missing piece for the explicit form of the average transverse force:

$$
\langle F_y\rangle = -\left(\frac{q_b}{e}\right)^2\,\frac{n_{b0}}{n_0}\,\frac{\sinh(y_e(\zeta))}{y_e(\zeta)}\int_{\zeta}^{\infty} d\zeta'\,\sin(\zeta-\zeta')f(\zeta')\, e^{-y_e(\zeta')}\,\frac{y_{e0}(\zeta')}{y_e(\zeta')}\,\sinh(y_c(\zeta)-y_c(\zeta')) . \tag{2.24}
$$

The differential equation for the centroid in 2D Cartesian coordinates for a flat-top transverse profile [43, 44] is therefore (after replacing Eq. 2.24 in Eq. 2.15):

$$
\begin{aligned}
\frac{d^2 y_c}{dz^2} &= -\frac{m_e}{\gamma M_b}\left(\frac{q_b}{e}\right)^2\,\frac{n_{b0}}{n_0}\,\frac{\sinh(y_e(\zeta))}{y_e(\zeta)} \\
&\qquad \int_{\zeta}^{\infty} d\zeta'\,\sin(\zeta-\zeta')f(\zeta')\, e^{-y_e(\zeta')}\,\frac{y_{e0}(\zeta')}{y_e(\zeta')}\,\sinh(y_c(\zeta)-y_c(\zeta')) \\
&= -\,2\,\frac{k_\beta^2}{k_p^2}\,\frac{\sinh(y_e(\zeta))}{y_e(\zeta)}\int_{\zeta}^{\infty} d\zeta'\,\sin(\zeta-\zeta')f(\zeta')\, e^{-y_e(\zeta')}\,\frac{y_{e0}(\zeta')}{y_e(\zeta')}\,\sinh(y_c(\zeta)-y_c(\zeta')) ,
\end{aligned}
\tag{2.25}
$$

where we used the definition of the betatron wavenumber $k_\beta = \omega_\beta/c = \frac{1}{c\sqrt{2\gamma}}\sqrt{\frac{n_{b0}q_b^2}{\varepsilon_0 M_b}}$. This result

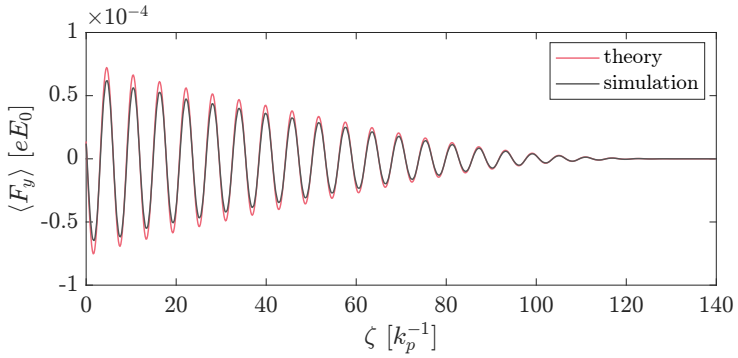

Figure 2.2: Initial plasma response to a hosing seed for a flat-top transverse profile in 2D Cartesian geometry according to simulation (grey) and Eq. 2.24 (red).

matches the one in Refs. [43, 44] (note that the transverse profile $g(y,\zeta,z)$ is incorrectly defined in both of these publications).

We can test the validity of the right-hand side of Eq. 2.25 by comparing the initial plasma response to a PIC simulation. In other words, we calculate the average transverse force in Eq. 2.24 for an initial centroid $y_{c0}(\zeta)$, and we compare this to $\langle F_y\rangle$ measured at the plasma entrance in a simulation with the same initial conditions. In this case we simulate a long, relativistic electron bunch with a flat-top transverse profile and cosine longitudinal profile in 2D Cartesian geometry, with $y_{c0}(\zeta) = 0.05\ \sin(1.07\ \zeta)$ (see Table A.1, item A.1.2, in Appx. A for the full simulation details). The result is shown in Fig. 2.2. Though this theory captures the plasma response reasonably well, there is a discrepancy that grows with ζ.

2D Cartesian, Gaussian transverse profile

Here we consider a Gaussian transverse profile, defined as $g(y,\zeta) = \exp\left[-\frac{(y-y_c(\zeta))^2}{2\,\sigma_y^2(\zeta,z)}\right]$, where $\sigma_y(\zeta,z)$ is the RMS bunch size in the y direction (its dependence on z will again be ommitted in the next steps). In 2D Cartesian coordinates, it is still possible to obtain a plasma response solution for this more realistic shape. Following the same procedure as before, we replace this transverse profile in $\partial_y\tau(y,\zeta')$, defined in Eq. 2.20:

$$\begin{aligned}\partial_y\tau(y,\zeta') =& -\frac{1}{2}\left[-e^{-y}\int_{-\infty}^{y} dy'\exp\left(y'-\frac{(y'-y_c(\zeta'))^2}{2\,\sigma_y^2(\zeta')}\right)+e^{y}\int_{y}^{\infty} dy'\exp\left(-y'-\frac{(y'-y_c(\zeta'))^2}{2\,\sigma_y^2(\zeta')}\right)\right]\\ =& -\frac{1}{2}\sqrt{\frac{\pi}{2}}\,\sigma_y(\zeta')\exp\left(-y-y_c(\zeta')+\frac{\sigma_y^2(\zeta')}{2}\right)\left[e^{2y}\ \mathrm{erfc}\left(\frac{y-y_c(\zeta')+\sigma_y^2(\zeta')}{\sqrt{2}\,\sigma_y(\zeta')}\right)\right.\\ &\left.-e^{2\,y_c(\zeta')}\ \mathrm{erfc}\left(\frac{y_c(\zeta')-y+\sigma_y^2(\zeta')}{\sqrt{2}\,\sigma_y(\zeta')}\right)\right]\ ,\end{aligned} \tag{2.26}$$

where $\mathrm{erfc}(x) = 1-\mathrm{erf}(x)$ is the complementary error function. The average over the transverse Gaussian profile simplifies to:

$$\begin{aligned}\langle\partial_y\tau(y,\zeta')\rangle =& \frac{\int_{-\infty}^{\infty} dy\ n_b(\zeta,y)\ \partial_y\tau(y,\zeta')}{\int_{-\infty}^{\infty} dy\ n_b(\zeta,y)} = \frac{n_{b0}f(\zeta)\int_{-\infty}^{\infty} dy\ g(y,\zeta)\ \partial_y\tau(y,\zeta')}{n_{b0}f(\zeta)\int_{-\infty}^{\infty} dy\ g(y,\zeta)}\\ =& \frac{1}{\sqrt{2\pi}\,\sigma_y(\zeta)}\int_{-\infty}^{\infty} dy\ g(y,\zeta)\ \partial_y\tau(y,\zeta')\ .\end{aligned} \tag{2.27}$$

The resulting integral, after replacing $\partial_y \tau(y,\zeta')$ and the transverse Gaussian profile, is:

$$\begin{aligned}\langle \partial_y \tau(y,\zeta')\rangle = &-\frac{1}{4}\frac{\sigma_y(\zeta')}{\sigma_y(\zeta)}\, e^{\sigma_y^2(\zeta')/2} \int_{-\infty}^{\infty} dy\ \exp\left[-\frac{(y-y_c(\zeta))^2}{2\,\sigma_y^2(\zeta)}\right] e^{-y-y_c(\zeta')} \\ &\left[e^{2y}\ \mathrm{erfc}\left(\frac{y-y_c(\zeta')+\sigma_y^2(\zeta')}{\sqrt{2}\,\sigma_y(\zeta')}\right) - e^{2\,y_c(\zeta')}\ \mathrm{erfc}\left(\frac{y_c(\zeta')-y+\sigma_y^2(\zeta')}{\sqrt{2}\,\sigma_y(\zeta')}\right)\right]\,,\end{aligned} \tag{2.28}$$

and can be written as four terms (by expanding the definition of $erfc(x)$). Two of these terms have the following solutions:

$$\begin{aligned}&\exp\left(-y_c(\zeta')-\frac{y_c^2(\zeta)}{2\sigma_y^2(\zeta)}\right)\int_{-\infty}^{\infty} dy\ \exp\left[-\frac{y^2}{2\sigma_y^2(\zeta)}+y\ \left(1+\frac{y_c(\zeta)}{\sigma_y^2(\zeta)}\right)\right] = \\ &\qquad\qquad \sqrt{2\pi}\ \sigma_y(\zeta)\ \exp\left(y_c(\zeta)-y_c(\zeta')+\frac{\sigma_y^2(\zeta)}{2}\right)\,,\end{aligned} \tag{2.29}$$

$$\begin{aligned}&-\exp\left(y_c(\zeta')-\frac{y_c^2(\zeta)}{2\sigma_y^2(\zeta)}\right)\int_{-\infty}^{\infty} dy\ \exp\left[-\frac{y^2}{2\sigma_y^2(\zeta)}-y\ \left(1-\frac{y_c(\zeta)}{\sigma_y^2(\zeta)}\right)\right] = \\ &\qquad\qquad -\sqrt{2\pi}\ \sigma_y(\zeta)\ \exp\left(y_c(\zeta')-y_c(\zeta)+\frac{\sigma_y^2(\zeta)}{2}\right)\,.\end{aligned} \tag{2.30}$$

The other two terms can be solved using the following identity [50]:

$$\int_{-\infty}^{\infty} \exp\left(-az^2+\beta z\right)\mathrm{erf}\left(a_1 z+\beta_1\right)dz = \sqrt{\frac{\pi}{a}}\exp\left(\frac{\beta^2}{4a}\right)\mathrm{erf}\left[\frac{2a\beta_1+a_1\beta}{2\sqrt{a^2+aa_1^2}}\right]\,,\quad a>0\,. \tag{2.31}$$

The two remaining terms of the integral in Eq. 2.28 therefore become

$$\begin{aligned}&\int_{-\infty}^{\infty}\exp\left[-\frac{(y-y_c(\zeta))^2}{2\,\sigma_y^2(\zeta)}\right]e^{-y-y_c(\zeta')}\ e^{2\,y_c(\zeta')}\ \mathrm{erf}\left(\frac{y_c(\zeta')-y+\sigma_y^2(\zeta')}{\sqrt{2}\,\sigma_y(\zeta')}\right)dy = \\ &\qquad \sqrt{2\pi}\ \sigma_y(\zeta)\ \exp\left(y_c(\zeta')-y_c(\zeta)+\frac{\sigma_y^2(\zeta)}{2}\right)\ \mathrm{erf}\left[\frac{y_c(\zeta')-y_c(\zeta)+\sigma_y^2(\zeta)+\sigma_y^2(\zeta')}{\sqrt{2\,\sigma_y^2(\zeta')-2\,\sigma_y^2(\zeta)}}\right]\,,\end{aligned} \tag{2.32}$$

$$\begin{aligned}&-\int_{-\infty}^{\infty}\exp\left[-\frac{(y-y_c(\zeta))^2}{2\,\sigma_y^2(\zeta)}\right]e^{-y-y_c(\zeta')}\ e^{2y}\ \mathrm{erf}\left(\frac{y-y_c(\zeta')+\sigma_y^2(\zeta')}{\sqrt{2}\,\sigma_y(\zeta')}\right)dy = \\ &\qquad -\sqrt{2\pi}\ \sigma_y(\zeta)\ \exp\left(y_c(\zeta)-y_c(\zeta')+\frac{\sigma_y^2(\zeta)}{2}\right)\ \mathrm{erf}\left[\frac{y_c(\zeta)-y_c(\zeta')+\sigma_y^2(\zeta)+\sigma_y^2(\zeta')}{\sqrt{2\,\sigma_y^2(\zeta')+2\,\sigma_y^2(\zeta)}}\right]\,.\end{aligned} \tag{2.33}$$

Replacing the solutions to the four integrals in Eq. 2.28, we obtain

$$\begin{aligned}\langle \partial_y \tau(\zeta',y)\rangle = &-\sqrt{\frac{\pi}{8}}\,\sigma_y(\zeta)\ \exp\left(\frac{\sigma_y^2(\zeta)+\sigma_y^2(\zeta')}{2}\right) \\ &\left\{e^{y_c(\zeta)-y_c(\zeta')}\ \mathrm{erfc}\left(\frac{y_c(\zeta)-y_c(\zeta')+\sigma_y^2(\zeta)+\sigma_y^2(\zeta')}{\sqrt{2\,\sigma_y^2(\zeta)+2\,\sigma_y^2(\zeta')}}\right)\right. \\ &\left. - e^{y_c(\zeta')-y_c(\zeta)}\ \mathrm{erfc}\left(\frac{y_c(\zeta')-y_c(\zeta)+\sigma_y^2(\zeta)+\sigma_y^2(\zeta')}{\sqrt{2\,\sigma_y^2(\zeta')-2\,\sigma_y^2(\zeta)}}\right)\right\}\,.\end{aligned} \tag{2.34}$$

This transverse solution for a Gaussian transverse profile in 2D Cartesian coordinates can now be substituted in Eq. 2.19 to obtain the average transverse force

$$\begin{aligned}\langle F_y \rangle = \sqrt{\frac{\pi}{8}}\,\frac{n_{b0}}{n_0}\left(\frac{q_b}{e}\right)^2 \int_\zeta^\infty d\zeta'\,\sin(\zeta-\zeta')\,f(\zeta')\exp\left(\frac{\sigma_y^2(\zeta)+\sigma_y^2(\zeta')}{2}\right) \\ \left\{ e^{y_c(\zeta)-y_c(\zeta')}\,\mathrm{erfc}\left(\frac{y_c(\zeta)-y_c(\zeta')+\sigma_y^2(\zeta)+\sigma_y^2(\zeta')}{\sqrt{2\,\sigma_y^2(\zeta)+2\,\sigma_y^2(\zeta')}}\right)\right. \\ \left. - e^{y_c(\zeta')-y_c(\zeta)}\,\mathrm{erfc}\left(\frac{y_c(\zeta')-y_c(\zeta)+\sigma_y^2(\zeta)+\sigma_y^2(\zeta')}{\sqrt{2\,\sigma_y^2(\zeta')-2\,\sigma_y^2(\zeta)}}\right)\right\}\,.\end{aligned} \tag{2.35}$$

and subsequently in Eq. 2.15 to arrive at the differential equation for the centroid:

$$\begin{aligned}\frac{d^2 y_c}{dz^2} = 2\,\frac{k_\beta^2}{k_p^2}\sqrt{\frac{\pi}{8}}\int_\zeta^\infty d\zeta'\,\sin(\zeta-\zeta')\,f(\zeta')\exp\left(\frac{\sigma_y^2(\zeta)+\sigma_y^2(\zeta')}{2}\right) \\ \left\{ e^{y_c(\zeta)-y_c(\zeta')}\,\mathrm{erfc}\left(\frac{y_c(\zeta)-y_c(\zeta')+\sigma_y^2(\zeta)+\sigma_y^2(\zeta')}{\sqrt{2\,\sigma_y^2(\zeta)+2\,\sigma_y^2(\zeta')}}\right)\right. \\ \left. - e^{y_c(\zeta')-y_c(\zeta)}\,\mathrm{erfc}\left(\frac{y_c(\zeta')-y_c(\zeta)+\sigma_y^2(\zeta)+\sigma_y^2(\zeta')}{\sqrt{2\,\sigma_y^2(\zeta')-2\,\sigma_y^2(\zeta)}}\right)\right\}\,.\end{aligned} \tag{2.36}$$

Equation 2.36 has not been previously derived or published.

In the case of a constant transverse size $\sigma_y(\zeta) = \sigma_y = \mathrm{const}$, Eq. 2.36 simplifies to

$$\begin{aligned}\frac{d^2 y_c}{dz^2} = 2\,\frac{k_\beta^2}{k_p^2}\sqrt{\frac{\pi}{8}}\sigma_y\,\exp(\sigma_y^2)\int_\zeta^\infty d\zeta'\,\sin(\zeta-\zeta')\,f(\zeta')\left\{\exp\left[y_c(\zeta')-y_c(\zeta)\right]\right. \\ \left.\mathrm{erfc}\left[\frac{y_c(\zeta')-y_c(\zeta)+2\,\sigma_y^2}{2\,\sigma_y}\right] - \exp\left[y_c(\zeta)-y_c(\zeta')\right]\,\mathrm{erfc}\left[\frac{y_c(\zeta)-y_c(\zeta')+2\,\sigma_y^2}{2\,\sigma_y}\right]\right\}\,.\end{aligned} \tag{2.37}$$

Figure 2.3 shows the initial plasma response for a long electron bunch with a Gaussian transverse profile, cosine longitudinal profile, and an initial centroid $y_{c0}(\zeta) = 0.05\,\sin(1.07\,\zeta)$, according to Eq. 2.35 and to a 2D Cartesian simulation (see Table A.1, item A.1.1, in Appx. A for the full simulation details). The theory matches the numerical data quite well.

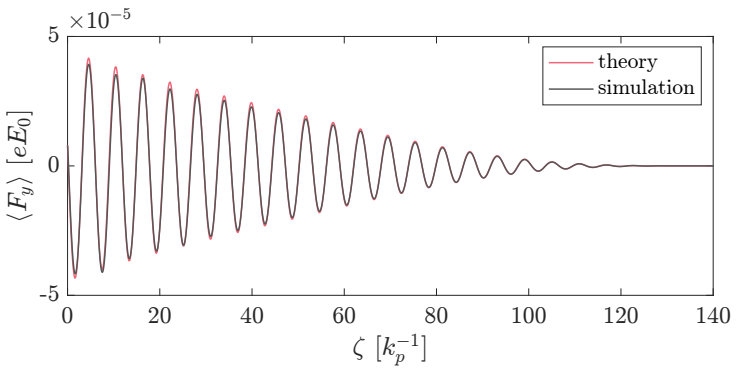

Figure 2.3: Initial plasma response to a hosing seed for a Gaussian transverse profile in 2D Cartesian geometry according to simulation (grey) and Eq. 2.35 (red).

2D cylindrical, flat-top transverse profile

The 2D cylindrical model for hosing allows us to more accurately represent the real geometry of a hosing bunch while avoiding the complexity of an exact three-dimensional description. The dimensionality of this model is reduced by assuming axisymmetry in cylindrical coordinates, which seems to preclude any description of hosing (which fundamentally requires some asymmetry along the propagation axis). However, the instability may still be represented by taking the approximation of small displacements and by expanding the azimuthal dependence into modes [43].

The general procedure will consist of using the axisymmetric cylindrical plasma response (along with the first Taylor-expanded azimuthal mode) and replacing it in the basic Cartesian equation for the centroid (Eq. 2.15). We will show that the existing version of this model [43] is incomplete, though it is accurate when the bunch radius is constant along ζ.

In order to keep the calculations workable, the transverse bunch profile is assumed to be a flat top with a small centroid offset along the y direction: $g(r,\theta,\zeta) = \hat{g}_0(r,\zeta) - \partial_r \hat{g}_0(r,\zeta)\, y_c(\zeta)\cos\theta$ [51]. The zero-mode ($m=0$) flat-top profile is defined as $\hat{g}_0(r,\zeta) = \left(\frac{r_{b0}(\zeta)}{r_b(\zeta)}\right)^2 \Theta\left[r_b(\zeta) - r\right]$, where $r_b(\zeta, z)$ is the bunch radius (the z dependence has been ommitted for simplicity) and $r_{b0}(\zeta) = r_b(\zeta, z=0)$.

As discussed in Sec. 2.1.1, when the bunch density profile can be expressed as a series of azimuthal modes, i.e., $n_b(\zeta,r,\theta) \propto \sum_{m=0}^{\infty} \hat{g}_m(r,\zeta)\cos(m\theta)$, the solution for the wake potential will also be of the form $\psi \propto \sum_{m=0}^{\infty} \hat{\psi}_m(r,\zeta)\cos(m\theta)$. In this case, we define the transverse profile as a sum of the $m=0$ and $m=1$ modes, i.e.,

$$g(r,\theta,\zeta) = \underbrace{\left(\frac{r_{b0}(\zeta)}{r_b(\zeta)}\right)^2 \Theta\left[r_b(\zeta) - r\right]}_{\hat{g}_0(r,\zeta)} + \underbrace{\left(\frac{r_{b0}(\zeta)}{r_b(\zeta)}\right)^2 \delta\left(r_b(\zeta) - r\right)\, y_c(\zeta)}_{\hat{g}_1(r,\zeta)}\, \cos\theta\,. \tag{2.38}$$

Putting together Eqs. 2.6, 2.10 and the profile $n_b(\zeta,r,\theta) = n_{b0}\cdot f(\zeta)\cdot g(r,\theta,\zeta)$, the wake potential is given by

$$\psi(\zeta,r,\theta) = \frac{q_b}{e}\,\frac{n_{b0}}{n_0}\int_{\zeta}^{\infty} d\zeta' \sin(\zeta-\zeta') f(\zeta') \left(\frac{r_{b0}(\zeta')}{r_b(\zeta')}\right)^2 \left[\hat{\psi}_0(r,\zeta') + \hat{\psi}_1(r,\zeta')\,\cos\theta\right]\,, \tag{2.39}$$

with

$$\begin{aligned}
\hat{\psi}_0(r,\zeta') &= K_0(r)\int_0^r dr'\, r'\, I_0(r')\,\Theta\left[r_b(\zeta') - r'\right] + I_0(r)\int_r^{\infty} dr'\, r'\, K_0(r')\,\Theta\left[r_b(\zeta') - r'\right]\,, \\
\hat{\psi}_1(r,\zeta') &= \left[K_1(r)\int_0^r dr'\, r'\, I_1(r')\,\delta\left(r_b(\zeta') - r'\right) + I_1(r)\int_r^{\infty} dr'\, r'\, K_1(r')\,\delta\left(r_b(\zeta') - r'\right)\right] y_c(\zeta')\,.
\end{aligned} \tag{2.40}$$

After computing the integrals in $\hat{\psi}_0(r,\zeta')$ and $\hat{\psi}_1(r,\zeta')$, we obtain

$$\hat{\psi}_0(r,\zeta') = \begin{cases} rI_1(r)K_0(r) + I_0(r)\Big[rK_1(r) - r_b(\zeta')K_1(r_b(\zeta'))\Big] \;:= \hat{\psi}_{0<}(r,\zeta') & r \le r_b(\zeta') \\ r_b(\zeta')I_1(r_b(\zeta'))K_0(r) \;:= \hat{\psi}_{0>}(r,\zeta') & r > r_b(\zeta') \end{cases} \tag{2.41}$$

$$\hat{\psi}_1(r,\zeta') = \begin{cases} I_1(r)r_b(\zeta')K_1(r_b(\zeta'))y_c(\zeta') \;:= \hat{\psi}_{1<}(r,\zeta') & r \le r_b(\zeta') \\ K_1(r)r_b(\zeta')I_1(r_b(\zeta'))y_c(\zeta') \;:= \hat{\psi}_{1>}(r,\zeta') & r > r_b(\zeta')\,. \end{cases} \tag{2.42}$$

Since the radial derivatives of $\hat{\psi}_0(r,\zeta')$ and $\hat{\psi}_1(r,\zeta')$ will be required later, we also note them here. It will prove more convenient for subsequent calculations to write the piecewise functions of the wake potential modes as $\hat{\psi}_i(r,\zeta') = \Theta[r_b(\zeta') - r]\,\hat{\psi}_{i<}(r,\zeta') + \Theta[r - r_b(\zeta')]\,\hat{\psi}_{i>}(r,\zeta')$, where $i = \{0,1\}$. In that case the radial derivatives will have the form $\partial_r\hat{\psi}_i(r,\zeta') = -\delta(r_b(\zeta') - r)\,\hat{\psi}_{i<} - \Theta[r_b(\zeta') -$

$r]\ \partial_r\hat{\psi}_{i<} + \delta(r - r_b(\zeta'))\ \hat{\psi}_{i>} + \Theta[r - r_b(\zeta')]\ \partial_r\hat{\psi}_{i>}$. The radial derivatives are therefore:

$$\begin{aligned}\partial_r\hat{\psi}_0(r,\zeta') =& -\delta(r_b(\zeta') - r)\ \hat{\psi}_{0<} - \Theta[r_b(\zeta') - r]\ r_b(\zeta')K_1(r_b(\zeta'))I_1(r) + \delta(r - r_b(\zeta'))\ \hat{\psi}_{0>} \\ &- \Theta[r - r_b(\zeta')]r_b(\zeta')I_1(r_b(\zeta'))K_1(r)\ ,\end{aligned} \tag{2.43}$$

$$\begin{aligned}\partial_r\hat{\psi}_1(r,\zeta') =& -\delta(r_b(\zeta') - r)\ \hat{\psi}_{1<} + \Theta[r_b(\zeta') - r]\ y_c(\zeta')r_b(\zeta')K_1(r_b(\zeta'))\tfrac{1}{2}\Big(I_0(r) + I_2(r)\Big) \\ &+ \delta(r - r_b(\zeta'))\ \hat{\psi}_{1>} - \Theta[r - r_b(\zeta')]\ y_c(\zeta')r_b(\zeta')I_1(r_b(\zeta'))\tfrac{1}{2}\Big(K_0(r) + K_2(r)\Big)\ .\end{aligned} \tag{2.44}$$

To compute the right-hand side of the centroid differential equation (Eq. 2.15), we need to determine $\langle\partial_y\psi\rangle$ (see Eq. 2.16). Replacing the bunch profile $n_b(\zeta, r, \theta)$ and the flat-top transverse part $\hat{g}_0(r,\zeta)$, the transverse average in cylindrical coordinates can be defined as

$$\begin{aligned}\langle\bullet\rangle &= \frac{n_{b0}\ f(\zeta)\displaystyle\int_0^\infty\int_0^{2\pi} d\theta\ dr\ \bullet\ r\ g(\zeta,r,\theta)}{n_{b0}\ f(\zeta)\displaystyle\int_0^\infty\int_0^{2\pi} d\theta\ dr\ r\ g(\zeta,r,\theta)} = \frac{\displaystyle\int_0^\infty\int_0^{2\pi} d\theta\ dr\ \bullet\ r\ \Big(\hat{g}_0(r,\zeta) + \hat{g}_1(r,\zeta)\cos\theta\Big)}{\displaystyle\int_0^\infty\int_0^{2\pi} d\theta\ dr\ r\ \Big(\hat{g}_0(r,\zeta) + \hat{g}_1(r,\zeta)\cos\theta\Big)} \\ &= \frac{\displaystyle\int_0^\infty\int_0^{2\pi} d\theta\ dr\ \bullet\ r\ \Big(\hat{g}_0(r,\zeta) + \hat{g}_1(r,\zeta)\cos\theta\Big)}{2\pi\displaystyle\int_0^\infty dr\ r\ \hat{g}_0(r,\zeta)} \\ &= \frac{\displaystyle\int_0^\infty\int_0^{2\pi} d\theta\ dr\ \bullet\ r\ \Big(\hat{g}_0(r,\zeta) + \hat{g}_1(r,\zeta)\cos\theta\Big)}{2\pi\left(\dfrac{r_{b0}(\zeta)}{r_b(\zeta)}\right)^2\displaystyle\int_0^\infty dr\ r\ \Theta\left[r_b(\zeta) - r\right]} \\ &= \frac{1}{\pi r_{b0}^2(\zeta)}\int_0^\infty\int_0^{2\pi} d\theta\ dr\ \bullet\ r\ \Big(\hat{g}_0(r,\zeta) + \hat{g}_1(r,\zeta)\cos\theta\Big)\ .\end{aligned} \tag{2.45}$$

Before proceeding to calculate $\langle\partial_y\psi\rangle$, we can make some further simplifications by considering the azimuthal dependence of ψ and $g(\zeta,r,\theta)$. The derivative ∂_y and the transverse average $\langle\bullet\rangle$ will only act on the transverse part of the wake potential $\psi_\perp = \hat{\psi}_0(r,\zeta') + \hat{\psi}_1(r,\zeta')\ \cos\theta$. Using the chain rule, we can translate the Cartesian derivative into $\partial_y = \cos\theta\ \partial_r - \sin\theta/r\ \partial_\theta$.

$$\begin{aligned}\partial_y\psi_\perp &= (\cos\theta\ \partial_r + \sin\theta\ \delta_\theta)\ \Big(\hat{\psi}_0(r,\zeta') + \hat{\psi}_1(r,\zeta')\ \cos\theta\Big) \\ &= \cos\theta\ \partial_r\hat{\psi}_0(r,\zeta') + \cos^2\theta\ \partial_r\hat{\psi}_1(r,\zeta') - \sin^2\theta\ \hat{\psi}_1(r,\zeta')\end{aligned} \tag{2.46}$$

Since the dependence of ψ on θ is exclusively in the form of trigonometric functions, we can further simplify our calculations of $\langle\partial_y\psi\rangle$ by performing the azimuthal integral over 2π:

$$\begin{aligned}\langle\partial_y\psi_\perp\rangle &\propto \int_0^{2\pi} d\theta\Big(\hat{g}_0(r,\zeta) + \hat{g}_1(r,\zeta)\cos\theta\Big)\ \Big(\cos\theta\ \partial_r\hat{\psi}_0(r,\zeta') + \cos^2\theta\ \partial_r\hat{\psi}_1(r,\zeta') - \sin^2\theta\ \hat{\psi}_1(r,\zeta')\Big) \\ &\propto \int_0^{2\pi} d\theta\ \Big(\cos\theta\ \hat{g}_0(r,\zeta)\ \partial_r\hat{\psi}_0(r,\zeta') + \cos^2\theta\ \hat{g}_0(r,\zeta)\ \partial_r\hat{\psi}_1(r,\zeta') + \frac{\sin^2\theta}{r}\ \hat{g}_0(r,\zeta)\ \hat{\psi}_1(r,\zeta') \\ &+ \cos^2\theta\ \hat{g}_1(r,\zeta)\ \partial_r\hat{\psi}_0(r,\zeta') + \cos^3\theta\ \hat{g}_1(r,\zeta)\ \partial_r\hat{\psi}_1(r,\zeta') + \frac{\sin^2\theta}{r}\cos\theta\ \hat{g}_1(r,\zeta)\ \hat{\psi}_1(r,\zeta')\Big) \\ &\propto \pi\left(\hat{g}_0(r,\zeta)\ \partial_r\hat{\psi}_1(r,\zeta') + \frac{\hat{g}_0(r,\zeta)}{r}\hat{\psi}_1(r,\zeta') + \hat{g}_1(r,\zeta)\ \partial_r\hat{\psi}_0(r,\zeta')\right)\ .\end{aligned} \tag{2.47}$$

Applying the partial derivative ∂_y and the transverse average to the wake potential defined in

Eq. 2.39, and after the previous simplifications, we have that

$$\langle \partial_y \psi \rangle = \frac{q_b}{e} \frac{n_{b0}}{n_0} \int_\zeta^\infty d\zeta' \sin(\zeta - \zeta') f(\zeta') \left(\frac{r_{b0}(\zeta')}{r_b(\zeta')} \right)^2 \langle \partial_y \psi_\perp \rangle \ , \tag{2.48}$$

with

$$\begin{aligned} \langle \partial_y \psi_\perp \rangle =& \frac{1}{r_{b0}^2(\zeta)} \int_0^\infty dr\ r\ \left(\hat{g}_0(r,\zeta)\, \partial_r \hat{\psi}_1(r,\zeta') + \frac{\hat{g}_0(r,\zeta)}{r} \hat{\psi}_1(r,\zeta') + \hat{g}_1(r,\zeta)\, \partial_r \hat{\psi}_0(r,\zeta') \right) \\ =& \frac{1}{r_b^2(\zeta)} \int_0^\infty dr\ r\ \left(\Theta\left[r_b(\zeta) - r\right] \partial_r \hat{\psi}_1(r,\zeta') + \Theta\left[r_b(\zeta) - r\right] \frac{\hat{\psi}_1(r,\zeta')}{r} \right. \\ & \left. +\ y_c(\zeta)\, \delta(r_b(\zeta) - r)\, \partial_r \hat{\psi}_0(r,\zeta') \right) . \end{aligned} \tag{2.49}$$

At this point it is necessary to go through the tedious process of calculating each term of the integral in $\langle \partial_y \psi_\perp \rangle$, being careful to separate $r_b(\zeta)$ and $r_b(\zeta')$, and minding the piecewise character of the wake potential modes $\hat{\psi}_0$ and $\hat{\psi}_1$ (see Eqs. 2.41–2.44). The result for each term will depend on whether $r_b(\zeta)$ is smaller or larger than $r_b(\zeta')$ (see Fig. 2.4). The following is a bulleted list of the results for each term once Eqs. 2.41–2.44 are replaced in the integral of Eq. 2.49.

- $\int_0^\infty dr\ r\ \Theta\left[r_b(\zeta) - r\right] \partial_r \hat{\psi}_1(r,\zeta')$
  - $-\int_0^\infty dr\ r\ \Theta\left[r_b(\zeta) - r\right]\ \delta(r_b(\zeta') - r)\ \hat{\psi}_{1<}$

$$\begin{aligned} &= -y_c(\zeta')\ r_b(\zeta')\ K_1(r_b(\zeta')) \int_0^\infty dr\ r\ \Theta\left[r_b(\zeta) - r\right]\ \delta(r_b(\zeta') - r)\ I_1(r) \\ &= -y_c(\zeta')\ r_b^2(\zeta')\ K_1(r_b(\zeta'))\ I_1(r_b(\zeta'))\ \Theta\left[r_b(\zeta) - r_b(\zeta')\right] \end{aligned} \tag{2.50}$$

  - $-\int_0^\infty dr\ r\ \Theta\left[r_b(\zeta) - r\right]\ \Theta[r_b(\zeta') - r]\ \partial_r \hat{\psi}_{1<}$

$$\begin{aligned} &= y_c(\zeta')\ r_b(\zeta') K_1(r_b(\zeta')) \int_0^\infty dr\ r\ \Theta\left[r_b(\zeta) - r\right]\ \Theta[r_b(\zeta') - r] \tfrac{1}{2} \Big(I_0(r) + I_2(r) \Big) \\ &= y_c(\zeta')\ r_b(\zeta') K_1(r_b(\zeta')) \begin{cases} \Big[1 - I_0(r_b(\zeta)) + r_b(\zeta) I_1(r_b(\zeta)) \Big] & r_b(\zeta) < r_b(\zeta') \\ \Big[1 - I_0(r_b(\zeta')) + r_b(\zeta') I_1(r_b(\zeta')) \Big] & r_b(\zeta) > r_b(\zeta') \end{cases} \end{aligned} \tag{2.51}$$

  - $\int_0^\infty dr\ r\ \Theta\left[r_b(\zeta) - r\right]\ \delta(r - r_b(\zeta'))\ \hat{\psi}_{1>}$

$$\begin{aligned} &= y_c(\zeta')\ r_b(\zeta')\ I_1(r_b(\zeta')) \int_0^\infty dr\ r\ \Theta\left[r_b(\zeta) - r\right]\ \delta(r - r_b(\zeta'))\ K_1(r) \\ &= y_c(\zeta')\ r_b^2(\zeta')\ I_1(r_b(\zeta'))\ K_1(r_b(\zeta'))\ \Theta\left[r_b(\zeta) - r_b(\zeta')\right] \end{aligned} \tag{2.52}$$

    This term cancels with Eq. 2.50.

  - $\int_0^\infty dr\ r\ \Theta\left[r_b(\zeta) - r\right]\ \Theta[r - r_b(\zeta')]\ \partial_r \hat{\psi}_{1>}$

$$\begin{aligned} &= -y_c(\zeta')\ r_b(\zeta')\ I_1(r_b(\zeta')) \int_0^\infty dr\ r\ \Theta\left[r_b(\zeta) - r\right]\ \Theta[r - r_b(\zeta')]\ \tfrac{1}{2} \Big(K_0(r) + K_2(r) \Big) \\ &= \begin{cases} 0 & r_b(\zeta) < r_b(\zeta') \\ -y_c(\zeta')\ r_b(\zeta')\ I_1(r_b(\zeta')) \int_{r_b(\zeta')}^{r_b(\zeta)} dr\ r\ \frac{1}{2} \Big(K_0(r) + K_2(r) \Big) & r_b(\zeta) > r_b(\zeta') \end{cases} \end{aligned}$$

    Using the identity $K_0(r) + K_2(r) = -2\ K_1'(r)$ [52, Eq. 10.29.1] and integrating by parts,

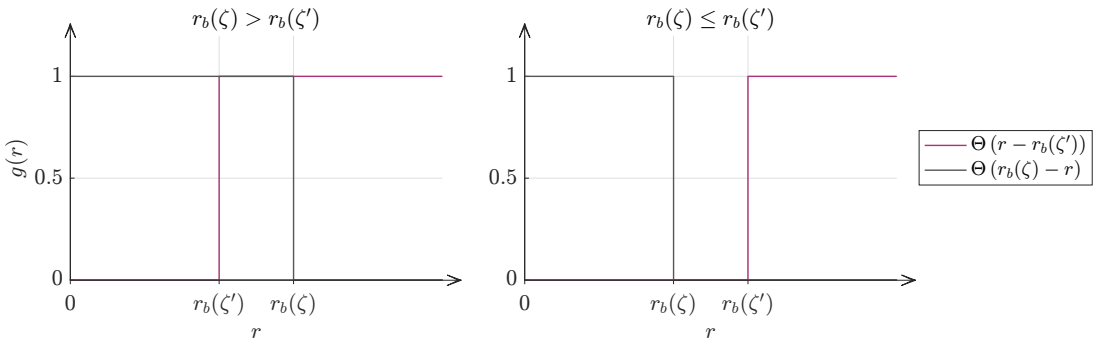

Figure 2.4: The two types of Heaviside function that must be integrated over in order to obtain a centroid differential equation for a flat-top transverse profile in cylindrical geometry, for two different relative cases for $r_b(\zeta)$ and $r_b(\zeta')$.

this term simplifies to

$$y_c(\zeta')\, r_b(\zeta')\, I_1(r_b(\zeta'))\Big[r_b(\zeta)\, K_1(r_b(\zeta)) - r_b(\zeta')\, K_1(r_b(\zeta')) + K_0(r_b(\zeta)) - K_0(r_b(\zeta'))\Big] \tag{2.53}$$

for $r_b(\zeta) > r_b(\zeta')$.

- $\int_0^\infty dr\; r\; \Theta\left[r_b(\zeta) - r\right] \frac{\hat{\psi}_1(r,\zeta')}{r}$
  - $\int_0^\infty dr \Theta\left[r_b(\zeta) - r\right]\; \Theta[r_b(\zeta') - r]\; \hat{\psi}_{1<}$

$$\begin{aligned} &= y_c(\zeta')\, r_b(\zeta')\, K_1(r_b(\zeta')) \int_0^\infty dr\; \Theta\left[r_b(\zeta) - r\right]\; \Theta[r_b(\zeta') - r]\; I_1(r) \\ &= \begin{cases} y_c(\zeta')\, r_b(\zeta')\, K_1(r_b(\zeta'))\, \Big[I_0(r_b(\zeta)) - 1\Big] & r_b(\zeta) < r_b(\zeta') \\ y_c(\zeta')\, r_b(\zeta')\, K_1(r_b(\zeta'))\, \Big[I_0(r_b(\zeta')) - 1\Big] & r_b(\zeta) > r_b(\zeta') \end{cases} \end{aligned} \tag{2.54}$$

  - $\int_0^\infty dr \Theta\left[r_b(\zeta) - r\right]\; \Theta[r - r_b(\zeta')]\; \hat{\psi}_{1>}$

$$\begin{aligned} &= y_c(\zeta')\, r_b(\zeta')\, I_1(r_b(\zeta')) \int_0^\infty dr\; \Theta\left[r_b(\zeta) - r\right]\; \Theta[r - r_b(\zeta')]\, K_1(r) \\ &= \begin{cases} 0 & r_b(\zeta) < r_b(\zeta') \\ y_c(\zeta')\, r_b(\zeta')\, I_1(r_b(\zeta'))\, \Big[K_0(r_b(\zeta')) - K_0(r_b(\zeta))\Big] & r_b(\zeta) > r_b(\zeta') \end{cases} \end{aligned} \tag{2.55}$$

  This term cancels with the last two terms of Eq. 2.53.

- $y_c(\zeta) \int_0^\infty dr\; r\; \delta(r_b(\zeta) - r)\; \partial_r \hat{\psi}_0(r, \zeta')$
  - $-y_c(\zeta) \int_0^\infty dr\; r\; \delta(r_b(\zeta) - r)\; \delta(r_b(\zeta') - r)\; \hat{\psi}_{0<}$

$$\begin{aligned} &= -y_c(\zeta) \int_0^\infty dr\; r\; \delta(r_b(\zeta) - r)\; \delta(r_b(\zeta') - r)\; \Big[rI_1(r)K_0(r) + I_0(r)\Big[rK_1(r) - r_b(\zeta')K_1(r_b(\zeta'))\Big]\Big] \\ &= -y_c(\zeta)\; r_{b=}^2\; I_1(r_{b=})\; K_0(r_{b=}) \end{aligned} \tag{2.56}$$

  Here $r_{b=}$ is the radius when $r_b(\zeta) = r_b(\zeta')$.

  - $-y_c(\zeta) \int_0^\infty dr\; r\; \delta(r_b(\zeta) - r)\; \Theta[r_b(\zeta') - r]\; \partial_r \hat{\psi}_{0<}$

$$= -y_c(\zeta)\; r_b(\zeta')\; K_1(r_b(\zeta')) \int_0^\infty dr\; r\; \delta(r_b(\zeta) - r)\; \Theta[r_b(\zeta') - r]\; I_1(r)$$

$$= \begin{cases} -y_c(\zeta)\; r_b(\zeta')\; K_1(r_b(\zeta'))\; r_b(\zeta)\; I_1(r_b(\zeta)) & r_b(\zeta) < r_b(\zeta') \\ 0 & r_b(\zeta) > r_b(\zeta') \end{cases} \tag{2.57}$$

✦ $y_c(\zeta) \int_0^\infty dr\; r\; \delta(r_b(\zeta) - r)\; \delta(r - r_b(\zeta'))\; \hat{\psi}_{0>}$

$$\begin{aligned} &= y_c(\zeta)\; r_b(\zeta')\; I_1(r_b(\zeta')) \int_0^\infty dr\; r\; \delta(r_b(\zeta) - r)\; \delta(r - r_b(\zeta'))\; K_0(r) \\ &= y_c(\zeta)\; r_{b=}^2\; I_1(r_{b=})\; K_0(r_{b=}) \end{aligned} \tag{2.58}$$

This term cancels with Eq. 2.56.

✦ $y_c(\zeta) \int_0^\infty dr\; r\; \delta(r_b(\zeta) - r)\; \Theta[r - r_b(\zeta')]\; \partial_r \hat{\psi}_{0>}$

$$\begin{aligned} &= -y_c(\zeta)\; r_b(\zeta')\; I_1(r_b(\zeta')) \int_0^\infty dr\; r\; \delta(r_b(\zeta) - r)\; \Theta[r - r_b(\zeta')]\; K_1(r) \\ &= \begin{cases} 0 & r_b(\zeta) < r_b(\zeta') \\ -y_c(\zeta)\; r_b(\zeta')\; I_1(r_b(\zeta'))\; r_b(\zeta)\; K_1(r_b(\zeta)) & r_b(\zeta) > r_b(\zeta') \end{cases} \end{aligned} \tag{2.59}$$

Collecting all the terms in Eqs. 2.50–2.59 and replacing them in Eq. 2.49 leads to the result

$$\langle \partial_y \psi_\perp \rangle = \begin{cases} \dfrac{r_b(\zeta')}{r_b(\zeta)}\; K_1(r_b(\zeta'))\; I_1(r_b(\zeta)) \left(y_c(\zeta') - y_c(\zeta) \right) & r_b(\zeta) < r_b(\zeta') \\ \dfrac{r_b(\zeta')}{r_b(\zeta)}\; I_1(r_b(\zeta'))\; K_1(r_b(\zeta)) \left(y_c(\zeta') - y_c(\zeta) \right) & r_b(\zeta) > r_b(\zeta') \end{cases} . \tag{2.60}$$

By putting together Eqs. 2.60, 2.48, 2.16 and 2.15, we finally arrive at the average transverse force

$$\langle F_y \rangle = -\frac{n_{b0}}{n_0} \left(\frac{q_b}{e} \right)^2 \int_\zeta^\infty d\zeta' \sin(\zeta - \zeta') f(\zeta') \frac{r_{b0}^2(\zeta')}{r_b(\zeta') r_b(\zeta)}\; I_1(r_{b<})\; K_1(r_{b>}) \left(y_c(\zeta') - y_c(\zeta) \right) \tag{2.61}$$

and the differential equation for the centroid in 2D cylindrical coordinates for a flat-top transverse profile:

$$\frac{d^2 y_c}{dz^2} = -2\; \frac{k_\beta^2}{k_p^2} \int_\zeta^\infty d\zeta' \sin(\zeta - \zeta') f(\zeta') \frac{r_{b0}^2(\zeta')}{r_b(\zeta') r_b(\zeta)}\; I_1(r_{b<})\; K_1(r_{b>}) \left(y_c(\zeta') - y_c(\zeta) \right) , \tag{2.62}$$

where $r_{b<}$ ($r_{b>}$) is the smallest (largest) of $r_b(\zeta)$ and $r_b(\zeta')$.

As mentioned before, the right-hand side of Eq. 2.62 is more general than the one in Ref. [43], where only the $r_b(\zeta) < r_b(\zeta')$ branch of the piecewise plasma response is considered. Naturally, this is only important when the bunch radius is not constant, i.e. $r_b = r_b(\zeta)$.

This is demonstrated in Fig. 2.5, where we validate the different versions of the theoretical plasma response in this geometry against 3D PIC simulations (see Table A.2, items A.2.1–A.2.2, in Appx. A for the full simulation details). Here we consider the initial centroid perturbation $y_{c0}(\zeta) = 0.01\; \sin(\zeta)$. In Fig. 2.5a), the initial bunch radius is constant ($r_{b0} = \text{const}$), and both Eq. 2.61 and Ref. [43] match the simulation data very closely. When we assume a varying initial bunch radius $r_{b0}(\zeta)$, however, the average transverse force can only be described accurately by the full piecewise right-hand side represented by Eq. 2.61, as exemplified in Fig. 2.5b) for $r_{b0}(\zeta) = 0.1[1 + 0.4\cos(\zeta)]$.

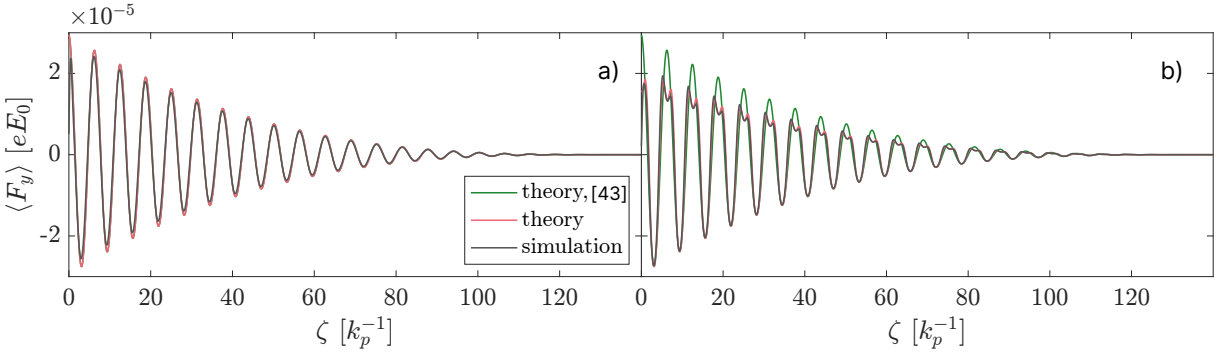

Figure 2.5: Initial plasma response to a hosing seed for a flat-top transverse profile in cylindrical coordinates according to a 3D simulation (grey), to Eq. 2.61 (red), and to Ref. [43] (green), with an initial bunch radius that is either constant (a) or oscillating (b).

2.2.2 Radius (SMI)

Long, relativistic bunches are subject to the focusing forces of the plasma wave driven by themselves. These wakefields therefore modulate the envelope of the bunch, in a process designated as the self-modulation instability. To describe this instability, we require an equation that relates the beam envelope (in this case, the RMS transverse size) to the forces due to the plasma wakefields. This equation can be derived by averaging the equation of motion for a bunch particle (Eq. 2.13) over the transverse bunch profile, such that the equation can be written in terms of the RMS size.

We once again choose the y dimension to set up the envelope differential equation. The RMS size is therefore defined as $\sigma_y = \sqrt{\langle (y-y_c)^2 \rangle}$, where $y_c = \langle y \rangle$ is the bunch centroid. As a first step, we subtract the term $d^2 y_c/dz^2$ from the y component of Eq. 2.13.

$$\begin{aligned} \frac{d^2 y}{dz^2} &= \frac{m_e}{\gamma M_b} F_y \\ \Leftrightarrow \quad \frac{d^2}{dz^2}(y-y_c) &= \frac{m_e}{\gamma M_b} F_y - \frac{d^2 y_c}{dz^2} \end{aligned} \tag{2.63}$$

Using the identity $\partial_x(\partial_x f) = 2\,(\partial_x f)^2 + 2\,f\,\partial_x^2 f$, we may write the left-hand side as

$$\frac{d^2}{dz^2}(y-y_c) = \frac{1}{2\,(y-y_c)} \left[\frac{d^2}{dz^2}(y-y_c)^2 - 2\,\left(\frac{d}{dz}(y-y_c) \right)^2 \right] . \tag{2.64}$$

Replacing this expression in Eq. 2.63, rearranging in terms of $\frac{d^2}{dz^2}(y-y_c)^2$ and averaging over the transverse bunch profile, we obtain

$$\frac{d^2}{dz^2} \left\langle (y-y_c)^2 \right\rangle = \frac{2\,m_e}{\gamma M_b} \left\langle (y-y_c) F_y \right\rangle - 2 \left\langle y-y_c \right\rangle \frac{d^2 y_c}{dz^2} + 2 \left\langle \left(\frac{d(y-y_c)}{dz} \right)^2 \right\rangle , \tag{2.65}$$

where the second term on the right-hand side vanishes, since $\langle y - y_c \rangle = \langle y \rangle - y_c = 0$.

Once again using the identity $\partial_x \sqrt{f} = \frac{1}{2} \partial_x f / \sqrt{f}$ and thus $\partial_x(\partial_x \sqrt{f}) = \frac{1}{4} f^{-3/2} [2\,f\,\partial_x^2 f - (\partial_x f)^2]$, the left-hand side of Eq. 2.65 may be written as

$$\begin{aligned} \frac{d^2}{dz^2} \left\langle (y-y_c)^2 \right\rangle &= \frac{1}{2\left\langle (y-y_c)^2 \right\rangle} \left[4 \left\langle (y-y_c)^2 \right\rangle^{3/2} \frac{d^2}{dz^2} \sqrt{\langle (y-y_c)^2 \rangle} + \left(\frac{d}{dz} \left\langle (y-y_c)^2 \right\rangle \right)^2 \right] \\ \Leftrightarrow \quad \frac{d^2}{dz^2} \sigma_y^2 &= \frac{1}{2\sigma_y^2} \left[4\,\sigma_y^3 \frac{d^2}{dz^2} \sigma_y + \left(\frac{d}{dz} \sigma_y^2 \right)^2 \right] . \end{aligned} \tag{2.66}$$

Once again, after replacing this expression and rearranging, Eq. 2.65 becomes

$$\frac{d^2\sigma_y}{dz^2} = \frac{m_e}{\gamma M_b}\frac{\langle (y-y_c)F_y\rangle}{\sigma_y} + \frac{1}{\sigma_y}\left\langle \left(\frac{d(y-y_c)}{dz}\right)^2 \right\rangle - \frac{1}{4\sigma_y^3}\left(\frac{d}{dz}\sigma_y^2\right)^2 . \tag{2.67}$$

Using the fact that $\partial_x f^2 = 2f\partial_x f$, the last two terms can be rewritten as

$$\frac{\sigma_y^2}{\sigma_y^3}\left\langle \left(\frac{d(y-y_c)}{dz}\right)^2 \right\rangle - \frac{1}{4\sigma_y^3}\left(\frac{d}{dz}\left\langle (y-y_c)^2\right\rangle\right)^2 = \\ \frac{1}{\sigma_y^3}\left[\left\langle (y-y_c)^2\right\rangle \left\langle \left(\frac{d(y-y_c)}{dz}\right)^2 \right\rangle - \left\langle (y-y_c)\frac{d}{dz}(y-y_c)\right\rangle^2\right] = \frac{\varepsilon_y^2}{\sigma_y^3} , \tag{2.68}$$

where ε_y is the RMS geometric emittance along y. We therefore arrive at the differential equation for the beam envelope:

$$\frac{d^2\sigma_y}{dz^2} - \frac{\varepsilon_y^2}{\sigma_y^3} = \frac{m_e}{\gamma M_b}\frac{\langle (y-y_c)F_y\rangle}{\sigma_y} . \tag{2.69}$$

Similarly to the differential equation for the bunch centroid, the specific form of the right-hand side in the presence of plasma wakefields will depend on the transverse profile of the bunch. This calculation has only been done for a flat-top transverse profile, since the required integrals for more complicated profiles do not have straightforward solutions.

2D cylindrical, flat-top transverse profile

Cylindrical coordinates are the natural choice to describe the self-modulation instability, since it arises from the axisymmetric component of the wakefields. In order to retain axisymmetry, we will assume small centroid displacements y_c. We therefore have $\langle (y-y_c)F_y\rangle \approx \langle y\ F_y\rangle$. Due to the axisymmetry, we can now write σ_y, y and F_y in terms of their radial components in cylindrical coordinates, e.g. $\sigma_y = \sigma_x = \sigma_r/\sqrt{2}$. Making these substitutions, we obtain

$$\frac{d^2\sigma_r}{dz^2} - \frac{4\ \varepsilon_y^2}{\sigma_r^3} = \frac{m_e}{\gamma M_b}\frac{\langle r\ F_r\rangle}{\sigma_r} , \tag{2.70}$$

where the geometric emittance along y will be simplified later.

The bunch profile is defined as $n_b(\zeta, r) = n_{b0}\cdot f(\zeta)\cdot g(r,\zeta)$, with $g(r,\zeta) = \left(\frac{r_{b0}(\zeta)}{r_b(\zeta)}\right)^2 \Theta\left[r_b(\zeta) - r\right]$, where once again $r_b(\zeta, z)$ is the bunch radius and $r_{b0}(\zeta) = r_b(\zeta, z=0)$. In this case, the average along the transverse bunch profile is defined as

$$\langle \bullet\rangle = \frac{n_{b0}\ f(\zeta)\displaystyle\int_0^\infty\int_0^{2\pi} d\theta\ dr\ \bullet\ r\ g(\zeta,r)}{n_{b0}\ f(\zeta)\displaystyle\int_0^\infty\int_0^{2\pi} d\theta\ dr\ r\ g(\zeta,r)} = \frac{2\pi\left(\frac{r_{b0}(\zeta)}{r_b(\zeta)}\right)^2\displaystyle\int_0^\infty dr\ \bullet\ r\ \Theta\left[r_b(\zeta)-r\right]}{2\pi\left(\frac{r_{b0}(\zeta)}{r_b(\zeta)}\right)^2\displaystyle\int_0^\infty dr\ r\ \Theta\left[r_b(\zeta)-r\right]} \\ = \frac{2}{r_b^2(\zeta)}\int_0^\infty dr\ \bullet\ r\ \Theta\left[r_b(\zeta)-r\right] . \tag{2.71}$$

In order to express Eq. 2.70 in terms of $r_b(\zeta, z)$, we replace the RMS radius of $g(r,\zeta)$, i.e. $\sigma_r = r_b/\sqrt{2}$. After some rearranging, we obtain the envelope equation in terms of the flat-top radius

$$\frac{d^2 r_b}{dz^2} - \frac{\varepsilon^2}{r_b^3} = \frac{2\ m_e}{\gamma M_b}\frac{\langle r\ F_r\rangle}{r_b} , \tag{2.72}$$

where we used the definition for the effective or RMS emittance $\varepsilon = 4\,\varepsilon_y$ [53]. This definition of the emittance is particularly appropriate for beams that are subject to nonlinear forces [as an example, ε_y vanishes for an S-shaped distribution in (y, y') phase space, while ε remains finite] [54, 55].

To calculate the right-hand side of Eq. 2.72, we must determine $\langle r\ F_r \rangle$ and therefore F_r, which is connected to the wake potential via (see Eq. 2.2)

$$F_r = -\frac{q_b}{e}\,\partial_r \psi\ . \tag{2.73}$$

The wake potential for an axisymmetric profile in cylindrical coordinates is given by the Green's function solutions in Eqs. 2.8 and 2.6. Replacing the flat-top transverse profile, the wake potential is therefore

$$\psi(\zeta, r) = \frac{q_b}{e}\,\frac{n_{b0}}{n_0}\int_\zeta^\infty d\zeta' \sin(\zeta - \zeta') f(\zeta') \left(\frac{r_{b0}(\zeta')}{r_b(\zeta')}\right)^2 \underbrace{\left[K_0(r)\int_0^r dr'\ r'\ I_0(r')\,\Theta\left[r_b(\zeta') - r'\right] + I_0(r)\int_r^\infty dr'\ r'\ K_0(r')\,\Theta\left[r_b(\zeta') - r'\right]\right]}_{\psi_r(r,\zeta')}\ , \tag{2.74}$$

where the radial dependence is confined to what we designated as $\psi_r(r, \zeta')$. The transverse averaging of the wakefield force only acts on the r-dependent part of F_r, i.e., $\langle r\ F_r \rangle \propto \langle r\ \partial_r \psi_r(r, \zeta') \rangle$. We will therefore compute these integrals separately and plug them into our desired expression later, using

$$\langle r\ F_r \rangle = -\frac{n_{b0}}{n_0}\ \left(\frac{q_b}{e}\right)^2 \int_\zeta^\infty d\zeta' \sin(\zeta - \zeta') f(\zeta') \left(\frac{r_{b0}(\zeta')}{r_b(\zeta')}\right)^2 \langle r\ \partial_r \psi_r(r, \zeta') \rangle\ . \tag{2.75}$$

As calculated before in Sec. 2.2.1 (see Eqs. 2.41 and 2.43), ψ_r and $\partial_r \psi_r$ can be written as

$$\psi_r(r, \zeta') = \begin{cases} rI_1(r)K_0(r) + I_0(r)\Big[rK_1(r) - r_b(\zeta')K_1(r_b(\zeta'))\Big]\ := \psi_{r<}(r, \zeta') & r \le r_b(\zeta') \\ r_b(\zeta')I_1(r_b(\zeta'))K_0(r)\ := \psi_{r>}(r, \zeta') & r > r_b(\zeta') \end{cases}, \tag{2.76}$$

$$\partial_r \psi_r(r, \zeta') = -\delta(r_b(\zeta') - r)\,\psi_{r<} - \Theta[r_b(\zeta') - r]\,\partial_r \psi_{r<} + \delta(r - r_b(\zeta'))\,\psi_{r>} + \Theta[r - r_b(\zeta')]\,\partial_r \psi_{r>}\ . \tag{2.77}$$

We must now compute the radial integral in Eq. 2.71 for all the terms in $\partial_r \psi_r(r, \zeta')$, once again carefully distinguishing between $r_b(\zeta)$ and $r_b(\zeta')$ (see Fig. 2.4 on p. 21).

■ $-\int_0^\infty dr\ r^2\ \Theta\left[r_b(\zeta) - r\right]\ \delta(r_b(\zeta') - r)\ \psi_{r<}$

$$\begin{aligned} &= -\int_0^\infty dr\ r^2\ \Theta\left[r_b(\zeta) - r\right]\ \delta(r_b(\zeta') - r)\ \Big(rI_1(r)K_0(r) + I_0(r)\Big[rK_1(r) - r_b(\zeta')K_1(r_b(\zeta'))\Big]\Big) \\ &= -r_b^3(\zeta')\ I_1(r_b(\zeta'))\ K_0(r_b(\zeta'))\ \Theta[r_b(\zeta) - r_b(\zeta')] \end{aligned} \tag{2.78}$$

■ $-\int_0^\infty dr\ r^2\ \Theta\left[r_b(\zeta) - r\right]\ \Theta[r_b(\zeta') - r]\ \partial_r \psi_{r<}$

$$\begin{aligned} &= -r_b(\zeta')\ K_1(r_b(\zeta'))\int_0^\infty dr\ r^2\ \Theta\left[r_b(\zeta) - r\right]\ \Theta[r_b(\zeta') - r]\ I_1(r) \\ &= \begin{cases} -r_b(\zeta')\ K_1(r_b(\zeta'))\ r_b^2(\zeta)\ I_2(r_b(\zeta)) & r_b(\zeta) < r_b(\zeta') \\ -r_b^3(\zeta')\ K_1(r_b(\zeta'))\ I_2(r_b(\zeta')) & r_b(\zeta) > r_b(\zeta') \end{cases} \end{aligned} \tag{2.79}$$

■ $\int_0^\infty dr\ r^2\ \Theta\left[r_b(\zeta)-r\right]\ \delta(r-r_b(\zeta'))\ \psi_{r>}$

$$\begin{aligned}&= r_b(\zeta')\ I_1(r_b(\zeta'))\int_0^\infty dr\ r^2\ \Theta\left[r_b(\zeta)-r\right]\ \delta(r-r_b(\zeta'))\ K_0(r)\\&= r_b^3(\zeta')\ I_1(r_b(\zeta'))\ K_0(r_b(\zeta'))\ \Theta[r_b(\zeta)-r_b(\zeta')]\end{aligned} \tag{2.80}$$

This term cancels with Eq. 2.78.

■ $\int_0^\infty dr\ r^2\ \Theta\left[r_b(\zeta)-r\right]\ \Theta[r-r_b(\zeta')]\ \partial_r\psi_{r>}$

$$\begin{aligned}&= -r_b(\zeta')\ I_1(r_b(\zeta'))\int_0^\infty dr\ r^2\ \Theta\left[r_b(\zeta)-r\right]\ \Theta[r-r_b(\zeta')]\ K_1(r)\\&= \begin{cases}0 & r_b(\zeta)<r_b(\zeta')\\ -r_b(\zeta')\ I_1(r_b(\zeta'))\displaystyle\int_{r_b(\zeta')}^{r_b(\zeta)} dr\ r^2\ K_1(r) & r_b(\zeta)>r_b(\zeta')\end{cases}\end{aligned}$$

The integral has the solution $\int dr\ r^2 K_1(r) = -r^2\ K_2(r)$ [52, Eq. 10.43.1], which leads to

$$r_b(\zeta')\ I_1(r_b(\zeta'))\left[r_b^2(\zeta)\ K_2(r_b(\zeta)) - r_b^2(\zeta')\ K_2(r_b(\zeta'))\right] \tag{2.81}$$

for $r_b(\zeta) > r_b(\zeta')$.

Collecting all the terms in Eqs. 2.78–2.81, we obtain

$$\begin{aligned}\langle r\ \partial_r\psi_r(r,\zeta')\rangle &= \frac{2}{r_b^2(\zeta)}\begin{cases}-r_b(\zeta')\ K_1(r_b(\zeta'))\ r_b^2(\zeta)\ I_2(r_b(\zeta)) & r_b(\zeta)<r_b(\zeta')\\ r_b(\zeta')\left[r_b^2(\zeta)\ K_2(r_b(\zeta))\ I_1(r_b(\zeta')) - r_b(\zeta')\right] & r_b(\zeta)>r_b(\zeta')\end{cases}\\&= \begin{cases}-2\ r_b(\zeta')\ K_1(r_b(\zeta'))\ I_2(r_b(\zeta)) & r_b(\zeta)<r_b(\zeta')\\ 2\ r_b(\zeta')\ I_1(r_b(\zeta'))\ K_2(r_b(\zeta)) - 2\ \dfrac{r_b^2(\zeta')}{r_b^2(\zeta)} & r_b(\zeta)>r_b(\zeta')\end{cases}.\end{aligned} \tag{2.82}$$

With this result, which we substitute in Eq. 2.75, we have determined the force that drives the SMI:

$$\begin{aligned}\frac{\langle r\ F_r\rangle}{r_b} = 2\ \frac{n_{b0}}{n_0}\ \left(\frac{q_b}{e}\right)^2 &\int_\zeta^\infty d\zeta' \sin(\zeta-\zeta')f(\zeta')\\ &\begin{cases}\dfrac{r_{b0}^2(\zeta')}{r_b(\zeta)r_b(\zeta')}\ K_1(r_b(\zeta'))\ I_2(r_b(\zeta)) & r_b(\zeta)<r_b(\zeta')\\ \dfrac{r_{b0}^2(\zeta')}{r_b^3(\zeta)} - \dfrac{r_{b0}^2(\zeta')}{r_b(\zeta)r_b(\zeta')}\ I_1(r_b(\zeta'))\ K_2(r_b(\zeta)) & r_b(\zeta)>r_b(\zeta')\end{cases}.\end{aligned} \tag{2.83}$$

We may now replace this force in Eq. 2.72, thus obtaining the differential equation for the bunch radius $r_b(\zeta, z)$ in axisymmetric cylindrical coordinates for a flat-top transverse profile.

$$\frac{d^2r_b}{dz^2} - \frac{\varepsilon^2}{r_b^3} = 8\ \frac{k_\beta^2}{k_p^2}\frac{I_2(r_b(\zeta))}{r_b(\zeta)}\int_\zeta^\infty d\zeta' \sin(\zeta-\zeta')f(\zeta')\ \frac{r_{b0}^2(\zeta')}{r_b(\zeta')}\ K_1(r_b(\zeta'))\ , \quad \text{for} \quad r_b(\zeta)<r_b(\zeta') \tag{2.84}$$

$$\begin{aligned}\frac{d^2r_b}{dz^2} - \frac{\varepsilon^2}{r_b^3} = 8\ &\frac{k_\beta^2}{k_p^2}\frac{1}{r_b^3(\zeta)}\int_\zeta^\infty d\zeta' \sin(\zeta-\zeta')f(\zeta')\ r_{b0}^2(\zeta')\\ &- 8\ \frac{k_\beta^2}{k_p^2}\frac{K_2(r_b(\zeta))}{r_b(\zeta)}\int_\zeta^\infty d\zeta' \sin(\zeta-\zeta')f(\zeta')\ \frac{r_{b0}^2(\zeta')}{r_b(\zeta')}\ I_1(r_b(\zeta'))\ , \quad \text{for} \quad r_b(\zeta)>r_b(\zeta')\end{aligned} \tag{2.85}$$

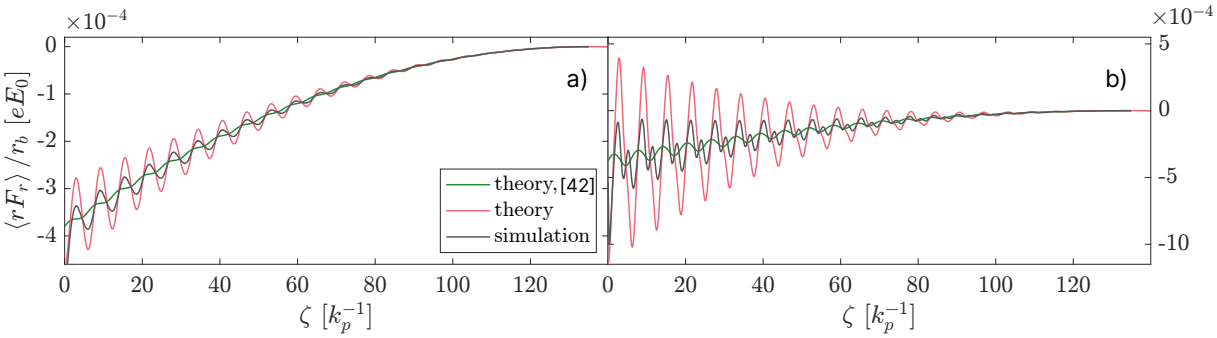

Figure 2.6: Initial plasma response to an SMI seed for a flat-top transverse profile in axisymmetric cylindrical coordinates according to simulation (grey), to Eq. 2.83 (red), and to Ref. [42] (green), for $\delta_r/r_{b0} = 0.01$ (a) and $\delta_r/r_{b0} = 0.1$ (b).

Equation 2.84 corresponds to what is available in the literature [42]. However, we note that the other branch, Eq. 2.85, of the piecewise differential equation has not been discussed in previous work. We can evaluate this result by seeding the SMI in an axisymmetric PIC simulation (in 2D cylindrical coordinates) and comparing the initial plasma response $\langle r\ F_r\rangle / r_b$ to Eq. 2.83. For this we initialize a long, relativistic positron bunch with a flat-top transverse profile and cosine longitudinal profile, and with a bunch radius perturbation given by $r_b(\zeta) = r_{b0} + \delta_r \sin(\zeta - \zeta_s)$, where δ_r is the perturbation amplitude and ζ_s is the location of the bunch front (see Table A.3, items A.3.1–A.3.2, in Appx. A for the full simulation details).

Figure 2.6 shows the comparison between the initial plasma response according to Eq. 2.83, Ref. [42], and simulations. The relative perturbation amplitude is $\delta_r/r_{b0} = 0.01$ in Fig. 2.6a) and $\delta_r/r_{b0} = 0.1$ in Fig. 2.6b). Although neither of the two versions of the theory can accurately reproduce the amplitude of the initial plasma response, the full piecewise version in Eq. 2.83 is able to capture the correct phase, as well as some of the nonlinearity (or harmonics) that appears for a larger radius perturbation [see non-sinusoidal shape of the red and grey curves in Fig. 2.6b)]. The reason for the discrepancy between theory and simulation is still unclear, although we were able to rule out the possibility that the assumption of linear wakefields ($n_{b0}/n_0 \ll 1$) was not met in the simulations.

2.3 Asymptotic models

So far we have determined different versions of differential equations that describe the HI and SMI. We still have no information about the growth rates of these instabilities, or how they evolve qualitatively along z and ζ. An analytical expression for the centroid $y_c(\zeta, z)$ and the bunch radius $r_b(\zeta, z)$ can be found using the following prescription:

1. Find a simplified partial differential equation by assuming a long-bunch, adiabatic regime (where the bunch changes slowly over many betatron periods)
2. Assume a slowly varying envelope and establish a partial differential equation for the envelope
3. Define initial conditions, and Laplace-transform the equation in z
4. Find the solution for the equation in Laplace space
5. Approximate the inverse Laplace transform of the solution using the method of steepest descent

This is the procedure used in several published works [42–44] where the evolution of the HI and SMI has been described using asymptotic methods. In this section, we reproduce those results, including their detailed derivation, and we discuss the advantages and limitations of these asymptotic models.

2.3.1 Centroid (HI)

In the following, we will derive the asymptotic model for the evolution of the bunch centroid in 2D cylindrical geometry for a flat-top transverse profile. Starting from Eq. 2.62, we assume a constant bunch radius $r_b(\zeta) = r_{b0} = \text{const}$. We therefore have

$$\frac{d^2 y_c}{dz^2} = -2\,\hat{k}_\beta^2\; I_1(r_{b0})\; K_1(r_{b0}) \int_\zeta^\infty d\zeta' \sin(\zeta - \zeta')\; f(\zeta')\; \Big(y_c(\zeta') - y_c(\zeta)\Big)\;, \tag{2.86}$$

where we have defined $\hat{k}_\beta^2 = k_\beta^2/k_p^2$. We may rewrite this equation as

$$\begin{aligned}\left(\partial_z^2 - \mu\hat{k}_\beta^2 \int_\zeta^\infty d\zeta' \sin(\zeta - \zeta')\; f(\zeta')\right) y_c(\zeta) &= -\mu\hat{k}_\beta^2 \int_\zeta^\infty d\zeta' \sin(\zeta - \zeta')\; f(\zeta')\; y_c(\zeta') \\ \Leftrightarrow \qquad \Big(\partial_z^2 + \mu\hat{k}_\beta^2\; f(\zeta)\Big)\, y_c(\zeta) &= -\mu\hat{k}_\beta^2 \int_\zeta^\infty d\zeta' \sin(\zeta - \zeta')\; f(\zeta')\; y_c(\zeta')\;,\end{aligned} \tag{2.87}$$

where we defined $\mu = 2I_1(r_{b0})K_1(r_{b0})$. To simplify the left-hand side we used integration by parts:

$$\int_\zeta^\infty d\zeta' \sin(\zeta - \zeta')\; f(\zeta') = \left[\cos(\zeta - \zeta') f(\zeta')\right]_\zeta^\infty - \int_\zeta^\infty d\zeta' \cos(\zeta - \zeta')\; \frac{\partial f(\zeta')}{\partial \zeta'}\;, \tag{2.88}$$

and assumed a long-bunch adiabatic regime, such that $\partial_\zeta f(\zeta) \to 0$. This assumption amounts to considering a very long, smooth bunch with respect to the typical length scale of the development of the HI (k_p^{-1}). Further noting that $f(\zeta \to \infty) = 0$, since the bunch distribution must be finite, Eq. 2.88 reduces to $-f(\zeta)$.

We now apply the longitudinal plasma operator $(\partial_\zeta^2 + 1)$ (see Sec. 2.1.1) to both sides of Eq. 2.87, while also setting $f(\zeta) \approx 1$ [42, 43] (consistent with the long-bunch adiabatic regime and especially valid close to the center of the bunch):

$$\Big(\partial_\zeta^2 + 1\Big)\Big(\partial_z^2 + \mu\hat{k}_\beta^2\Big)\, y_c = \mu\hat{k}_\beta^2\; y_c\;, \tag{2.89}$$

where we used the fact that $L_\zeta \int_{D_\zeta} d\zeta'\; G(\zeta', \zeta) F(\zeta') = F(\zeta)$. Note that the minus sign on the right-hand side cancels because $G(\zeta', \zeta) = \sin(\zeta' - \zeta) = -\sin(\zeta - \zeta')$ (for $\zeta' \geq \zeta$).

Having obtained a partial differential equation for the centroid $y_c(\zeta, z)$, we will now assume that the centroid behaves according to $y_c(\zeta, z) = \hat{y}_c/2 \cdot \exp(i\zeta) + \text{c.c.}$, where $\hat{y}_c(\zeta, z)$ is the envelope and c.c. denotes the complex conjugate. Note that we are assuming an oscillation at k_p, which is hidden in the normalized ζ variable. After replacing our assumed form of the centroid, we are left with an equation for the envelope $\hat{y}_c(\zeta, z)$. After some rearranging, and assuming a slowly varying envelope, i.e., applying the approximations $|\partial_\zeta \hat{y}_c| \ll |\hat{y}_c|$ and $|\partial_z \hat{y}_c| \gg \mu\hat{k}_\beta^2 |\hat{y}_c|$, we obtain

$$\begin{aligned}\partial_z^2 \partial_\zeta(\partial_\zeta + 2i)\; \hat{y}_c + \mu\hat{k}_\beta^2\; \partial_\zeta(\partial_\zeta + 2i)\; \hat{y}_c - \mu\hat{k}_\beta^2\; \hat{y}_c &= 0 \\ \Leftrightarrow \quad 2i\; \partial_\zeta \left(\partial_z^2 + \mu\hat{k}_\beta^2\right)\; \hat{y}_c - \mu\hat{k}_\beta^2\; \hat{y}_c &= 0 \\ \Leftrightarrow \quad \left(\partial_\zeta \partial_z^2 + \frac{i}{2}\mu\hat{k}_\beta^2\right)\; \hat{y}_c &= 0\;.\end{aligned} \tag{2.90}$$

In order to solve Eq. 2.90, we perform a Laplace transform in the z variable, choosing the following initial conditions: $\hat{y}_c(\zeta=0,z)=\delta_c\Theta(z)$, $\hat{y}_c(\zeta,z=0)=\delta_c$ and $\partial_z\hat{y}_c|_{z=0}=0$. These conditions correspond to a constant offset δ_c of the bunch centroid being turned on at $z=0$, where the leading slice of the bunch (at $\zeta=0$) remains fixed. The resulting equation for the Laplace-transformed centroid $Y(\zeta,s)=\mathcal{L}\{\hat{y}_c(\zeta,z)\}(\zeta,s)$ is

$$\partial_\zeta Y+\frac{i}{2}\frac{\mu\hat{k}_\beta^2}{s^2}\,Y=0\,, \tag{2.91}$$

which has the solution

$$Y(\zeta,s)=\frac{\delta_c}{s}\exp\left(-\frac{i}{2}\frac{\mu\hat{k}_\beta^2}{s^2}\zeta\right)\,. \tag{2.92}$$

To determine the expression for the centroid we would need to find the inverse Laplace transform of the envelope solution in Eq. 2.92. The inverse Laplace transform can be defined via the Bromwich integral

$$f(t)=\mathcal{L}^{-1}\{F(s)\}(t)=\frac{1}{2\pi i}\int_{\gamma-i\infty}^{\gamma+i\infty}e^{st}F(s)ds\,, \tag{2.93}$$

where the real-valued γ should be greater than the real part of all singularities of $F(s)$. Since the only singularity of $Y(\zeta,s)$ is at $s=0$, γ should be greater than zero. In this case, the envelope in real space is given by

$$\hat{y}_c(\zeta,z)=\frac{\delta_c}{2\pi i}\int_{\gamma-i\infty}^{\gamma+i\infty}\frac{1}{s}\exp\left(sz-\frac{i}{2}\frac{\mu\hat{k}_\beta^2}{s^2}\zeta\right)ds\,. \tag{2.94}$$

We will use the method of steepest descent [56, Sec. 13.2] to find the approximate solution of the integral in Eq. 2.94. This method approximates an integral along a complex contour C of the form $I(s)=\int_C f(s)\exp\left[\lambda\,g(s)\right]ds$, where $s\in\mathbb{C}$, λ is a large real number, $f(s)$ and $g(s)$ are analytical functions and $f(s)$ varies slowly, by deforming the contour C such that an extremum of $g(s)$ (a saddle point in the complex plane) is crossed. All other contributions to the integral besides the saddle point s_0 will be exponentially smaller, such that the integral can be approximated as

$$I(s)\approx f(s_0)\,e^{\lambda g(s_0)}e^{i\alpha_0}\sqrt{\frac{2\pi}{\lambda\,G_0''}}\,, \tag{2.95}$$

where we have defined $\frac{d^2g}{ds^2}|_{s=s_0}=G_0''\,e^{i\theta_0}$ (in exponential notation), and $\alpha_0=\frac{-\theta_0\pm\pi}{2}$ determines the direction of the deformed contour. The larger λ is, the better this approximation is.

In this case, we choose:

$$\lambda=\mu\hat{k}_\beta^2\,,\quad f(s)=\frac{\delta_c}{2\pi i}\,\frac{1}{s}\,,\quad g(s)=\frac{sz}{\lambda}-\frac{i}{2}\frac{\zeta}{s^2}\,. \tag{2.96}$$

Setting $\frac{dg}{ds}=0$, we find three saddle points for $g(s)$ [see Fig. 2.7a)]:

$$s_1=\left(\lambda\frac{|\zeta|}{z}\right)^{1/3}e^{i\frac{\pi}{2}}\,,\quad s_2=\left(\lambda\frac{|\zeta|}{z}\right)^{1/3}e^{i\frac{7\pi}{6}}\,,\quad s_3=\left(\lambda\frac{|\zeta|}{z}\right)^{1/3}e^{i\frac{11\pi}{6}}\,. \tag{2.97}$$

Since s_1 and s_2 lie in $\gamma\leq 0$, we choose the saddle point $s_0=s_3$. Taking the second derivative of $g(s)$, we have $G_0''=3\,\zeta^{-1/3}(z/\lambda)^{4/3}$ and $\theta_0=\pi/6$. The two possible values for α_0 are therefore $5\pi/12$ and $-7\pi/12$. Both of these angles correspond to the white dash-dotted line in Fig. 2.7b), the difference being the direction in which s_3 is crossed. The most sensible way to deform C such that it crosses the saddle point s_3 along the dash-dotted line [see Fig. 2.7b)] is from south to north

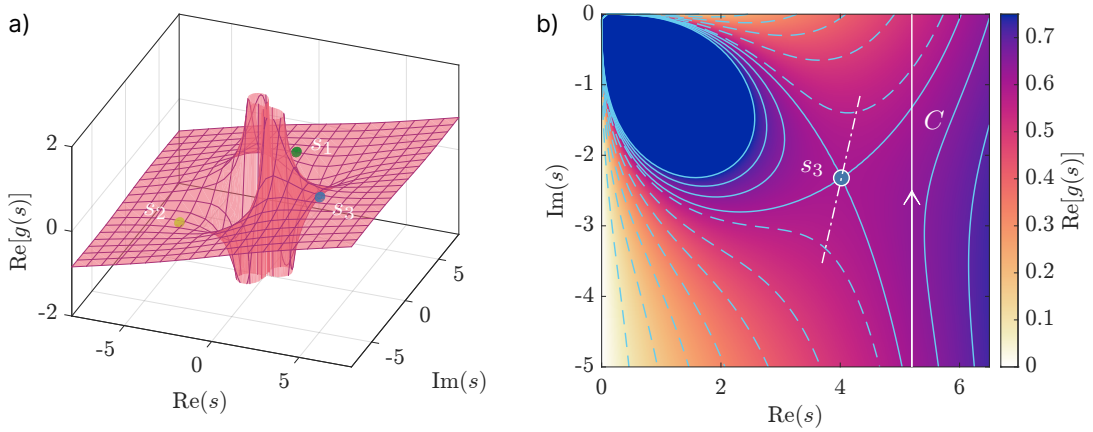

Figure 2.7: Visualization of the function $g(s)$ and the contour integral for the method of steepest descent. a) Real part of $g(s)$ on the complex plane (pink surface) and the three saddle points found for $g(s)$ (colored spheres). b) Real part of $g(s)$ (color scale and blue contour lines) in the vicinity of s_3 (blue circle). Dashed contour lines represent values $\mathrm{Re}[g(s)] < \mathrm{Re}[g(s_3)]$, while solid contour lines correspond to $\mathrm{Re}[g(s)] \geq \mathrm{Re}[g(s_3)]$. The integration contour from $\gamma - i\infty$ to $\gamma + i\infty$ is represented by the solid white vertical arrow. The dash-dotted white line crossing s_3 corresponds to the angles $\alpha_0 = 5\pi/12$ and $\alpha_0 = -7\pi/12$.

($\alpha_0 = 5\pi/12$), rather than north to south ($\alpha_0 = -7\pi/12$). We therefore choose $\alpha_0 = 5\pi/12$. Lastly, we are only missing $f(s_0)$ and $g(s_0)$, which are given by

$$f(s_0) = \frac{\delta_c}{2\pi} z\, N_h^{-1}\, e^{-i\frac{\pi}{3}}\,, \quad g(s_0) = \frac{3}{2}\,\frac{N_h}{\lambda}\, e^{-i\frac{\pi}{6}}\,, \tag{2.98}$$

where we have defined $N_h = \left(\lambda|\zeta|z^2\right)^{1/3} = \left(\mu\hat{k}_\beta^2|\zeta|z^2\right)^{1/3}$. Putting these results together and after some simplification, the approximate result of Eq. 2.94 is

$$\begin{aligned}\hat{y}_c(\zeta, z) &\approx \frac{\delta_c}{2\pi} z\, N_h^{-1}\, e^{-i\frac{\pi}{3}} \exp\left(\frac{3}{2}\, N_h\, e^{-i\frac{\pi}{6}}\right) e^{i\frac{5\pi}{12}} \sqrt{\frac{2\pi}{3\, z^2 N_h^{-1}}} \\ &\approx \frac{\delta_c}{\sqrt{6\pi}}\, N_h^{-1/2} \exp\left[\frac{3}{2} N_h \left(\frac{\sqrt{3}}{2} + \frac{i}{2}\right) + i\frac{\pi}{12}\right]\,. \end{aligned} \tag{2.99}$$

We may now substitute Eq. 2.99 into the assumed form of the centroid $y_c(\zeta, z) = \hat{y}_c/2 \cdot \exp(i\zeta) + \text{c.c.} = \mathrm{Re}[\hat{y}_c \cdot \exp(i\zeta)]$ and obtain an asymptotic model for the evolution of the centroid [43]:

$$y_c(\zeta, z) = \delta_c\, \frac{3^{1/4}}{\sqrt{8\pi}}\, \frac{e^{\Gamma_{\mathrm{HI}}}}{\sqrt{\Gamma_{\mathrm{HI}}}} \cos\left(\frac{\pi}{12} + \zeta - \frac{\Gamma_{\mathrm{HI}}}{\sqrt{3}}\right)\,, \tag{2.100}$$

where we defined the HI growth rate $\Gamma_{\mathrm{HI}} = (3^{3/2}/4) N_h = (3^{3/2}/4)\left(\mu\hat{k}_\beta^2|\zeta|z^2\right)^{1/3}$. Note that the sign of ζ in the argument of the cosine differs from Ref. [43] due to ζ being defined there as $\zeta \in]-\infty, 0]$, whereas this formulation is general (ζ may be either positive or negative).

2.3.2 Radius (SMI)

An asymptotic model for the SMI can be established using the same method as above, and making some stronger assumptions about the bunch radius. We start from the differential equation for the bunch radius for a flat-top transverse profile Eq. 2.84 (taking only the branch $r_b(\zeta) < r_b(\zeta')$ into account) and assume a small radius perturbation r_1 around a radius r_0 which evolves slowly at the

betatron time scale, with $r_1/r_0 \ll 1$. Substituting $r_b(\zeta, z) = r_0(\zeta, z) + r_1(\zeta, z)$ in Eq. 2.84, we obtain

$$\frac{d^2}{dz^2}(r_0 + r_1) - \frac{\varepsilon^2}{(r_0 + r_1)^3} = 8\,\hat{k}_\beta^2 \frac{I_2(r_0 + r_1)}{r_0 + r_1} \int_\zeta^\infty d\zeta' \sin(\zeta - \zeta') f(\zeta')\, \frac{r_{b0}^2(\zeta')}{r_0' + r_1'}\, K_1(r_0' + r_1') \,, \tag{2.101}$$

where we are using the shorthand $r_i = r_i(\zeta)$ and $r_i' = r_i(\zeta')$, with $i = \{0, 1\}$. Note that, strictly speaking, r_{b0} corresponds to $r_b(\zeta, 0)$ and should therefore be expressed in terms of the linear expansion $r_0(\zeta, 0) + r_1(\zeta, 0)$, which ultimately leads to the same result. We therefore keep the variable r_{b0} for now and eliminate it later with a more direct approximation. To simplify Eq. 2.101 we will linearize the following terms as a function of $r_1/r_0 \ll 1$.

$$(r_0 + r_1)^{-3} = r_0^{-3} \left(1 + \frac{r_1}{r_0}\right)^{-3} \approx r_0^{-3} \left(1 - 3\,\frac{r_1}{r_0}\right) \tag{2.102}$$

$$\frac{I_2(r_0 + r_1)}{r_0 + r_1} = \frac{I_2\left(r_0\left(1 + \frac{r_1}{r_0}\right)\right)}{r_0\left(1 + \frac{r_1}{r_0}\right)} \approx \frac{I_2(r_0)}{r_0}\left(1 + \frac{r_1}{r_0}\right) + I_3(r_0)\,\frac{r_1}{r_0} \tag{2.103}$$

$$\frac{K_1(r_0' + r_1')}{r_0' + r_1'} = \frac{K_1\left(r_0'\left(1 + \frac{r_1'}{r_0'}\right)\right)}{r_0'\left(1 + \frac{r_1'}{r_0'}\right)} \approx \frac{K_1(r_0')}{r_0'} - K_2(r_0')\,\frac{r_1'}{r_0'} \tag{2.104}$$

The term $\partial_z^2 r_0$ is given by the envelope equation itself (Eq. 2.84):

$$\frac{d^2 r_0}{dz^2} = \frac{\varepsilon^2}{r_0^3} + 8\,\hat{k}_\beta^2 \frac{I_2(r_0)}{r_0} \int_\zeta^\infty d\zeta' \sin(\zeta - \zeta') f(\zeta')\, \frac{r_{b0}^2(\zeta')}{r_0'}\, K_1(r_0') \,. \tag{2.105}$$

At this point, we will take a brief detour to demonstrate that we can remove r_0 from the integration in ζ' by assuming that $\partial_\zeta r_0 \to 0$. Let us consider the integral $\int_\zeta^\infty d\zeta'\, p(\zeta')\, q(r_0(\zeta'))$ with the arbitrary functions p and q. Applying integration by parts, this can be written as

$$\int_\zeta^\infty d\zeta'\, p(\zeta')\, q(r_0(\zeta')) = \left[P(\zeta')\, q(r_0(\zeta'))\right]_\zeta^\infty - \int_\zeta^\infty d\zeta' P(\zeta')\, \frac{\partial q(r_0(\zeta'))}{\partial \zeta'} \,, \tag{2.106}$$

where $P(\zeta')$ is the indefinite integral of $p(\zeta')$. Bearing in mind the domain $\zeta \in [0, \infty[$ (see Sec. 2.1.1), we may write $P(\zeta') = -\int_{\zeta'}^\infty d\tau\, p(\tau)$, using the fundamental theorem of calculus and an appropriate change of variables. By the chain rule of differentiation we know that $\partial_\zeta q(r_0) \propto \partial_\zeta r_0$ and therefore $\partial_\zeta q(r_0) \to 0$. We are thus left with

$$\begin{aligned} & \int_\zeta^\infty d\zeta'\, p(\zeta')\, q(r_0(\zeta')) = P(\zeta' \to \infty)\, q(r_0(\zeta' \to \infty)) + q(r_0(\zeta)) \int_\zeta^\infty d\tau\, p(\tau) \\ \Leftrightarrow \quad & \int_\zeta^\infty d\zeta'\, p(\zeta')\, q(r_0(\zeta')) = q(r_0(\zeta)) \int_\zeta^\infty d\zeta'\, p(\zeta') \,, \end{aligned} \tag{2.107}$$

where we used the fact that the bunch is finite and that $r_0(\zeta \to \infty) = 0$.

We can now replace the expansions in Eqs. 2.102–2.105 in Eq. 2.101 and apply Eq. 2.107, producing

$$\begin{aligned} & \frac{\varepsilon^2}{r_0^3} + 8\,\hat{k}_\beta^2 \frac{I_2(r_0) K_1(r_0)}{r_0^2} \int_\zeta^\infty d\zeta' \sin(\zeta - \zeta') f(\zeta')\, r_{b0}^2(\zeta') + \frac{d^2 r_1}{dz^2} - \frac{\varepsilon^2}{r_0^3}\left(1 - 3\,\frac{r_1}{r_0}\right) = \\ & 8\,\hat{k}_\beta^2 \left[\frac{I_2(r_0)}{r_0}\left(1 + \frac{r_1}{r_0}\right) + I_3(r_0)\,\frac{r_1}{r_0}\right] \int_\zeta^\infty d\zeta' \sin(\zeta - \zeta') f(\zeta')\, r_{b0}^2(\zeta') \left[\frac{K_1(r_0)}{r_0} - K_2(r_0)\,\frac{r_1'}{r_0}\right] \,. \end{aligned} \tag{2.108}$$

The right-hand side includes a term proportional to $I_2(r_0) K_1(r_0)/r_0^2$, which cancels with the second term on the left-hand side. This leaves five further terms on the right-hand side, two

of which are proportional to $(r_1/r_0)^2$ and which we neglect. Note that one of these terms ($\propto K_2(r_0)I_3(r_0)\, r_{b0}^2(\zeta')\, r_1 r_1'/r_0^2$) may only be neglected with the added assumption that $r_1(\zeta) \ll 1$. We also neglect the emittance term proportional to r_1/r_0^4, which can be shown graphically to be comparatively small. Finally, we assume that, within the fast timescale of the development of the SMI, $r_0 \approx r_{b0} = r_b(\zeta, z=0)$. After some simplification, Eq. 2.108 becomes

$$\frac{d^2 r_1}{dz^2} = -8\,\hat{k}_\beta^2 I_2(r_0)K_2(r_0)\int_\zeta^\infty d\zeta' \sin(\zeta-\zeta')f(\zeta')\,r_1' + 8\,\hat{k}_\beta^2\,K_1(r_0)\,r_1\left[\frac{I_2(r_0)}{r_0}+I_3(r_0)\right]\int_\zeta^\infty d\zeta'\sin(\zeta-\zeta')f(\zeta')\,. \quad (2.109)$$

Similarly to the previous section, we assume a long-bunch adiabatic regime, setting $f(\zeta)\approx 1$, and thus replace $\int_\zeta^\infty d\zeta' \sin(\zeta-\zeta')f(\zeta') \approx -f(\zeta) \approx -1$ (see Eq. 2.88 on p. 28). After resetting Eq. 2.109, we obtain a differential equation for the bunch radius perturbation $r_1(\zeta,z)$:

$$\begin{aligned} &\left(\frac{d^2}{dz^2}+4\,\kappa^2\hat{k}_\beta^2\right) r_1(\zeta,z) = -2\,\nu\hat{k}_\beta^2\int_\zeta^\infty d\zeta'\sin(\zeta-\zeta')\,r_1(\zeta',z) \\ \Leftrightarrow\quad &\left(\partial_\zeta^2+1\right)\left(\partial_z^2+4\,\kappa^2\hat{k}_\beta^2\right) r_1(\zeta,z) = 2\,\nu\hat{k}_\beta^2\,r_1(\zeta,z) \end{aligned} \quad (2.110)$$

where we defined[1] $\kappa^2 = 2\,K_1(r_0)\,[I_2(r_0)/r_0 + I_3(r_0)]$ and $\nu = 4\,I_2(r_0)K_2(r_0)$, and where we applied the longitudinal plasma operator to both sides of the equation (see Eq. 2.89 on p. 28). Note that a complete version of Eq. 2.110, where both branches are contemplated (for $r_b(\zeta) < r_b(\zeta')$ and $r_b(\zeta) > r_b(\zeta')$), can be found on p. 66.

We now assume that the bunch radius perturbation oscillates at k_p and has the form $r_1(\zeta,z) = \hat{r}/2\cdot\exp(i\zeta) + \text{c.c.}$, where $\hat{r}$ is a slowly varying envelope, such that $|\partial_\zeta\hat{r}| \ll |\hat{r}|$ and $|\partial_z\hat{r}| \gg 2\,\kappa\hat{k}_\beta|\hat{r}|$. Applying these assumptions to Eq. 2.110, we obtain after some simplification

$$\begin{aligned} &\partial_z^2\partial_\zeta\,(\partial_\zeta+2i)\;\hat{r} + 4\,\kappa^2\hat{k}_\beta^2\,\partial_\zeta\,(\partial_\zeta+2i)\;\hat{r} = 2\,\nu\hat{k}_\beta^2\,\hat{r} \\ \Leftrightarrow\quad &2i\,\partial_\zeta\left(\partial_z^2+4\,\kappa^2\hat{k}_\beta^2\right)\;\hat{r} = 2\,\nu\hat{k}_\beta^2\,\hat{r} \\ \Leftrightarrow\quad &\left(\partial_\zeta\partial_z^2 + i\,\nu\hat{k}_\beta^2\right)\;\hat{r} = 0\,. \end{aligned} \quad (2.111)$$

Following the prescription outlined in the introduction to Sec. 2.3, we apply a Laplace transform in z to Eq. 2.111. With the initial conditions $\hat{r}(\zeta=0,z) = \delta_r\Theta(z)$, $\hat{r}(\zeta,z=0) = \delta_r$ and $\partial_z\hat{r}|_{z=0} = 0$, where δ_r is the initial oscillation amplitude, the Laplace-transformed equation for $R(\zeta,s) = \mathcal{L}\{\hat{r}(\zeta,z)\}(\zeta,s)$ is

$$\partial_\zeta R + i\,\frac{\nu\hat{k}_\beta^2}{s^2}\,R = 0\,. \quad (2.112)$$

The solution to this equation is given by

$$R(\zeta,s) = \frac{\delta_r}{s}\exp\left(-i\,\frac{\nu\hat{k}_\beta^2}{s^2}\zeta\right) \quad (2.113)$$

in Laplace space and by

$$\hat{r}(\zeta,z) = \frac{\delta_r}{2\pi i}\int_{\gamma-i\infty}^{\gamma+i\infty}\frac{1}{s}\exp\left(sz - i\,\frac{\nu\hat{k}_\beta^2}{s^2}\zeta\right)ds \quad (2.114)$$

[1] Note that the definition of κ^2 in Ref. [42] is incorrect.

in (ζ, z) space, where γ should be larger than the real singularity of $R(\zeta, s)$ at $s = 0$.

We once again approximate the inverse Laplace transform of the solution, Eq. 2.114, with the method of steepest descent (see p. 29). Choosing

$$\lambda = \nu \hat{k}_\beta^2 \,, \quad f(s) = \frac{\delta_r}{2\pi i} \, \frac{1}{s} \,, \quad g(s) = \frac{sz}{\lambda} - i \, \frac{\zeta}{s^2} \,, \tag{2.115}$$

we follow the same procedure as in the previous section. Since the calculation details are almost identical, we allow ourselves to skip to the final result. The asymptotic model for the evolution of the bunch radius perturbation $r_1(\zeta, z) = r_b(\zeta, z) - r_{b0}(\zeta)$ for a flat-top transverse bunch profile is [42]

$$r_1(\zeta, z) = \delta_r \, \frac{3^{1/4}}{\sqrt{8\pi}} \, \frac{e^{\Gamma_{\mathrm{SMI}}}}{\sqrt{\Gamma_{\mathrm{SMI}}}} \, \cos\left(\frac{\pi}{12} + \zeta - \frac{\Gamma_{\mathrm{SMI}}}{\sqrt{3}} \right) \,, \tag{2.116}$$

where the SMI growth rate is defined as $\Gamma_{\mathrm{SMI}} = (3^{3/2}/4) \, N_{\mathrm{sm}} = (3^{3/2}/4) \left(2 \, \nu \hat{k}_\beta^2 |\zeta| z^2 \right)^{1/3}$.

2.3.3 Discussion

Following the algebraic recipe outlined at the beginning of this section has awarded us with an analytical expression both for the evolution of the bunch centroid and radius, and for the spatiotemporal growth rates of both instabilities.

In order to obtain the asymptotic models, it was necessary to make several assumptions. To recapitulate, we list the approximations underlying the models in this section:

- Linear wakefield theory ($\delta n / n_0 \ll 1$, where δn is the plasma density perturbation)
- Flat-top transverse bunch profile with bunch radius r_b
- Constant ($r_b = r_{b0} = \mathrm{const}$) or slowly evolving ($\partial_\zeta r_{b0} \to 0$) bunch radius
- Linear stage of instability development ($y_c \ll 1$, $r_1 / r_{b0} \ll 1$, and $r_1 \ll 1$), meaning for example that saturation mechanisms are not contemplated
- Initial sinusoidal perturbation at the plasma wavelength (k_p)
- Slowly varying envelope: $k_p |\hat{x}| \gg |\partial_{\zeta_*} \hat{x}|$ and $k_\beta |\hat{x}| \ll |\partial_{z_*} \hat{x}|$, where $\hat{x}$ is the envelope of a fast oscillation and ζ_* and z_* are not normalized (see paragraphs before Eqs. 2.90 and 2.111)
- Long-bunch, adiabatic regime ($\partial_\zeta f(\zeta) \to 0$ and $f(\zeta) \approx 1$)
- Parameter λ for the method of steepest descent (Eq. 2.95) is large ($\lambda \gg 1$)

We also point out that this description precludes any coupling between the HI and SMI.

The approximation of a slowly varying envelope, in particular, may be expressed in alternative terms. If we use the fact that $\hat{x} \propto e^\Gamma / \sqrt{\Gamma}$, where Γ is a growth rate, it follows that

$$\frac{e^\Gamma}{\sqrt{\Gamma}} \gg \frac{e^\Gamma}{\sqrt{\Gamma}} \, \frac{(2\Gamma - 1) \, \partial_\zeta \Gamma}{2\Gamma} \qquad \Leftrightarrow \qquad 1 \gg \partial_\zeta \Gamma \,. \tag{2.117}$$

Both factors μ and $2\,\nu$ are ~ 1 for $r_{b0} \lesssim 10 \, k_p^{-1}$, so we can assume $\Gamma \approx (3^{3/2}/4) \left(\hat{k}_\beta^2 |\zeta| z^2 \right)^{1/3}$. Taking the partial derivative of Γ in ζ, we obtain

$$1 \gg \frac{\sqrt{3}}{4} \left(\hat{k}_\beta^2 z^2 \right)^{1/3} |\zeta|^{-2/3} \qquad \Leftrightarrow \qquad |\zeta| \gg \left(\frac{\sqrt{3}}{4} \right)^{3/2} \hat{k}_\beta \, |z|$$

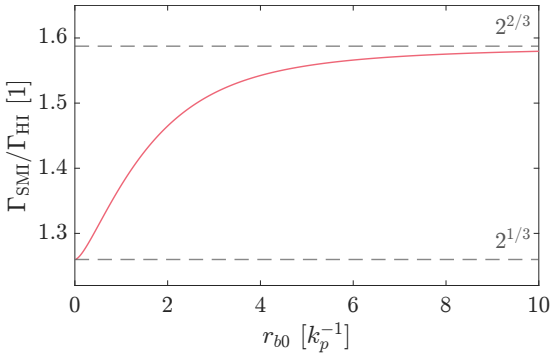

Figure 2.8: Ratio of the SMI growth rate to the HI growth rate as a function of the initial bunch radius, according to the asymptotic models.

$$\Leftrightarrow \qquad |\zeta| \gg \hat{k}_\beta \, |z| \qquad \Leftrightarrow \qquad k_p \, |\zeta_*| \gg k_\beta \, |z_*| \, , \tag{2.118}$$

since $(\sqrt{3}/4)^{3/2} \approx 0.3$. The condition in Eq. 2.118 is associated with the so-called long-bunch, early-time regime, meaning that the asymptotic models above are valid early enough and far enough along the bunch. In particular, these models are not applicable to the front of the bunch. (Note that, regardless of how the ζ-domain is defined, the front of the bunch is where $\zeta \to 0$, and the back of the bunch is in the direction of $\zeta \to \pm\infty$.)

We can compare the two spatiotemporal growth rates obtained with the asymptotic approach for the hosing and self-modulation instabilities. Under the assumptions made above, the ratio between both growth rates depends simply on the initial bunch radius r_{b0}:

$$\frac{\Gamma_{\mathrm{SMI}}}{\Gamma_{\mathrm{HI}}} = \left(\frac{2\nu}{\mu}\right)^{1/3} = \left(\frac{4\, I_2(r_{b0}) K_2(r_{b0})}{I_1(r_{b0}) K_1(r_{b0})}\right)^{1/3} . \tag{2.119}$$

This dependence is illustrated in Fig. 2.8. In the limits where $r_{b0} \to 0$ and $r_{b0} \to \infty$, the ratio in Eq. 2.119 is $2^{1/3} \approx 1.26$ and $2^{2/3} \approx 1.59$, respectively (see dashed lines in Fig. 2.8). This means that, given equivalent initial conditions, the growth rates for the HI and SMI are of the same order, and these instabilities are liable to compete with each other, though Γ_{SMI} is always larger than Γ_{HI}.

2.4 Power series model

An alternative model for the onset of the HI and SMI can be found using a power series approach, which has been utilized before in the context of conventional accelerator physics [57]. This model has the advantage of being flexible with respect to the initial conditions, as well as applying to the front of the bunch. On the other hand, its range of validity is relatively limited in terms of the propagation distance.

In Sections 2.2 and 2.3 we have derived several differential equations to describe different moments of the bunch profile (e.g. the centroid or the RMS size). For a general moment $m(\zeta, z)$, these differential equations may be expressed as

$$\frac{d^2 m}{dz^2} = \mathcal{R}\{m\} \, , \tag{2.120}$$

where $\mathcal{R}$ is an operator in the ζ variable and contains the plasma response. For the power series approach to be tractable, $\mathcal{R}$ should be a linear function of m. This is always the case when we assume to be in the linear stage of instability development ($y_c \ll 1$ or $r_1/r_{b0} \ll 1$), since $\mathcal{R}$ may

then be approximated by the first order of its Taylor expansion in terms of m (i.e., $\mathcal{R} \propto m$).

If we write m as a power series in z, $m(\zeta, z) = \sum_{n=0}^{\infty} a_n(\zeta)\, z^n$, and substitute this in Eq. 2.120, we obtain a recurrence relation for the coefficients a_n:

$$\begin{aligned} \sum_{n=2}^{\infty} a_n\, n(n-1)\, z^{n-2} &= \sum_{n=0}^{\infty} \mathcal{R}\{a_n\}\, z^n \\ \Leftrightarrow \quad \sum_{n=0}^{\infty} a_{n+2}\, (n+2)(n+1)\, z^n &= \sum_{n=0}^{\infty} \mathcal{R}\{a_n\}\, z^n \\ \Leftrightarrow \quad a_{n+2} &= \frac{\mathcal{R}\{a_n\}}{(n+2)(n+1)}\,. \end{aligned} \tag{2.121}$$

Assuming some arbitrary initial conditions, $m(\zeta, z=0) = m_0(\zeta)$ and $m'(\zeta, z=0) = \partial_z m|_{z=0} = m_0'(\zeta)$, we can define the first two coefficients: $a_0 = m_0(\zeta)$ and $a_1 = m_0'(\zeta)$. This allows us to frame the recurrence relation in Eq. 2.121 as a general formula that depends on the initial conditions. After some algebraic consolidation, we can express the evolution of the general moment $m(\zeta, z)$ and its z-derivative $m'(\zeta, z)$ as

$$m(\zeta, z) = \sum_{n=0}^{\infty} \frac{z^n}{n!} \begin{cases} \mathcal{R}^{(\frac{n}{2})}\{m_0\}\,, & n \text{ is even} \\ \mathcal{R}^{(\frac{n-1}{2})}\{m_0'\}\,, & n \text{ is odd} \end{cases}, \tag{2.122}$$

$$m'(\zeta, z) = \sum_{n=0}^{\infty} \frac{z^n}{n!} \begin{cases} \mathcal{R}^{(\frac{n}{2})}\{m_0'\}\,, & n \text{ is even} \\ \mathcal{R}^{(\frac{n+1}{2})}\{m_0\}\,, & n \text{ is odd} \end{cases}, \tag{2.123}$$

where the superscript in the operator $\mathcal{R}$ signifies consecutive applications (e.g. $\mathcal{R}^{(2)}\{m\} = \mathcal{R}\{\mathcal{R}\{m\}\}$ and $\mathcal{R}^{(0)}\{m\} = m$). By truncating Eqs. 2.122 and 2.123 at an adequate order, we obtain an approximate power series model for the evolution of $m(\zeta, z)$. Note that truncation at $n = 2$ corresponds to holding the plasma response to the initial conditions m_0 and m_0' constant (the right-hand side in Eq. 2.120 becomes constant in z and the solution will be proportional to z^2).

The right-hand side of the beam moment differential equations in this chapter, which determine the development of the hosing and self-modulation instabilities, is invariably proportional to k_β^2. This means that the typical length scale for the evolution of m along z is the betatron period k_β^{-1}. Since the power series model in Eqs. 2.122 and 2.123 is valid for the linear stage of instability development, we can conclude that the model is valid for $z \lesssim k_\beta^{-1}$.

In the following, we will discuss two specific cases of the right-hand side operator $\mathcal{R}$ which can be used to describe the early evolution of the HI and SMI.

2.4.1 Centroid (HI)

To demonstrate how the power series model can be applied to hosing, we choose two cases: 2D Cartesian geometry with a Gaussian transverse profile and 2D cylindrical geometry with a flat-top transverse profile. For simplicity, we assume constant transverse bunch sizes in both cases ($\sigma_y = \text{const}$ and $r_b = \text{const}$).

2D Cartesian, Gaussian transverse profile

In this case, and bearing in mind the constant beam envelope, the bunch centroid y_c is described by Eq. 2.37. The right-hand side operator is therefore

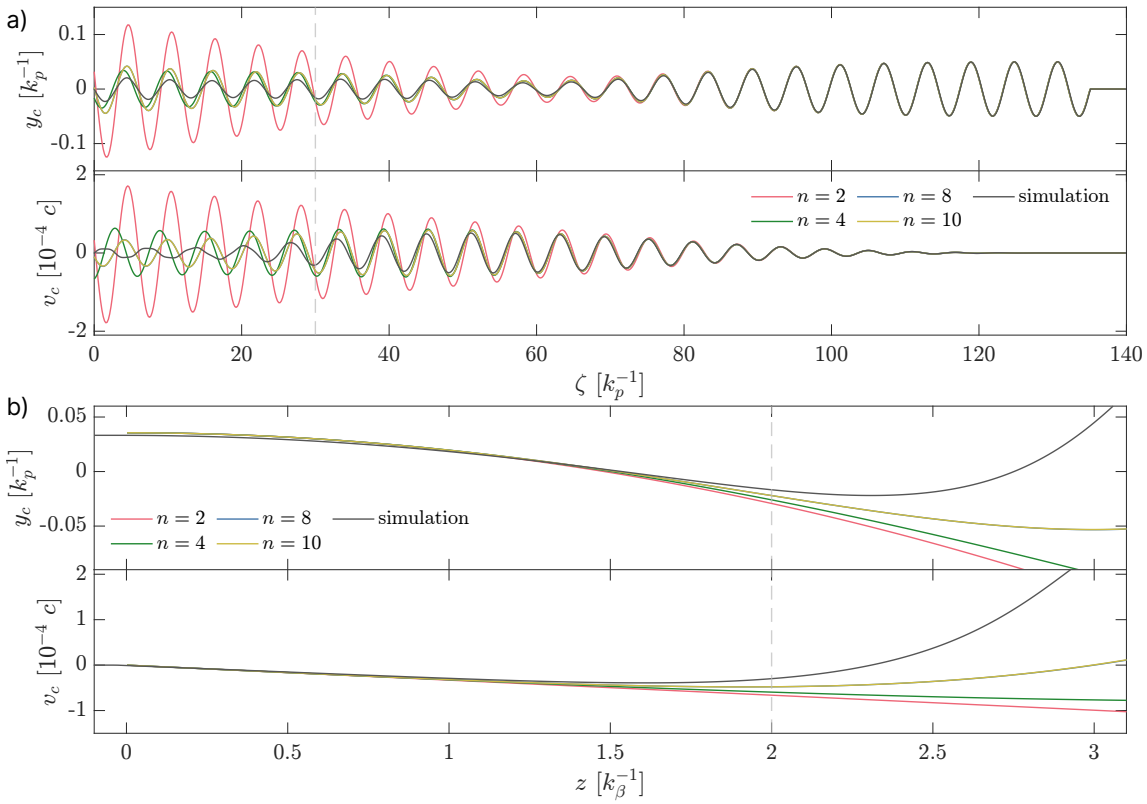

Figure 2.9: Line-outs of the centroid y_c and centroid velocity v_c along ζ at $z = 2\,k_\beta^{-1}$ (a) and along z at $\zeta = 30\,k_p^{-1}$ (b) for a Gaussian transverse profile in 2D Cartesian geometry according to simulation (dark grey) and the power series model truncated at different terms (colors). The vertical grey dashed lines indicate the position of the line-out along the other dimension. Note that the curves for $n = 8$ and $n = 10$ overlap almost completely.

$$\mathcal{R}\{y_c\} = 2\,\hat{k}_\beta^2 \sqrt{\frac{\pi}{8}}\sigma_y\ \exp(\sigma_y^2) \int_\zeta^\infty d\zeta'\,\sin(\zeta-\zeta')\,f(\zeta') \left\{ \exp\left[y_c(\zeta') - y_c(\zeta)\right] \right.$$
$$\left. \operatorname{erfc}\left[\frac{y_c(\zeta') - y_c(\zeta) + 2\,\sigma_y^2}{2\,\sigma_y}\right] - \exp\left[y_c(\zeta) - y_c(\zeta')\right]\ \operatorname{erfc}\left[\frac{y_c(\zeta) - y_c(\zeta') + 2\,\sigma_y^2}{2\,\sigma_y}\right] \right\}, \quad (2.124)$$

which is manifestly not a linear function of y_c. We must expand $\mathcal{R}$ in terms of y_c (assuming $y_c \ll 1$). To first order, and treating $y_c(\zeta') - y_c(\zeta) \propto y_c$ as the expansion variable,

$$\exp\left[y_c(\zeta') - y_c(\zeta)\right] \operatorname{erfc}\left[\frac{y_c(\zeta') - y_c(\zeta) + 2\,\sigma_y^2}{2\,\sigma_y}\right] - \exp\left[y_c(\zeta) - y_c(\zeta')\right]\ \operatorname{erfc}\left[\frac{y_c(\zeta) - y_c(\zeta') + 2\,\sigma_y^2}{2\,\sigma_y}\right]$$
$$\approx \left[2\operatorname{erfc}(\sigma_y) - \frac{2}{\sqrt{\pi}\,\sigma_y}\,e^{-\sigma_y^2}\right]\left(y_c(\zeta') - y_c(\zeta)\right). \quad (2.125)$$

For small centroid displacements, we can therefore define the right-hand side operator as

$$\mathcal{R}\{y_c\} = \sqrt{2}\,\hat{k}_\beta^2 \left[1 - \sqrt{\pi}\,\sigma_y\,e^{\sigma_y^2}\operatorname{erfc}(\sigma_y)\right] \int_\zeta^\infty d\zeta'\,\sin(\zeta-\zeta')\,f(\zeta')\left(y_c(\zeta') - y_c(\zeta)\right). \quad (2.126)$$

Plugging this operator into Eqs. 2.122 and 2.123 and truncating at $n = 4$, for example, we have

$$y_c(\zeta, z) = y_{c0}(\zeta) + \quad v_{c0}(\zeta)\cdot z + \mathcal{R}\{y_{c0}\}\cdot\frac{z^2}{2} + \quad \mathcal{R}\{v_{c0}\}\cdot\frac{z^3}{6} + \mathcal{R}^{(2)}\{y_{c0}\}\cdot\frac{z^4}{24}, \quad (2.127)$$

$$v_c(\zeta, z) = v_{c0}(\zeta) + \mathcal{R}\{y_{c0}\}\cdot z + \mathcal{R}\{v_{c0}\}\cdot\frac{z^2}{2} + \mathcal{R}^{(2)}\{y_{c0}\}\cdot\frac{z^3}{6} + \mathcal{R}^{(2)}\{v_{c0}\}\cdot\frac{z^4}{24}, \quad (2.128)$$

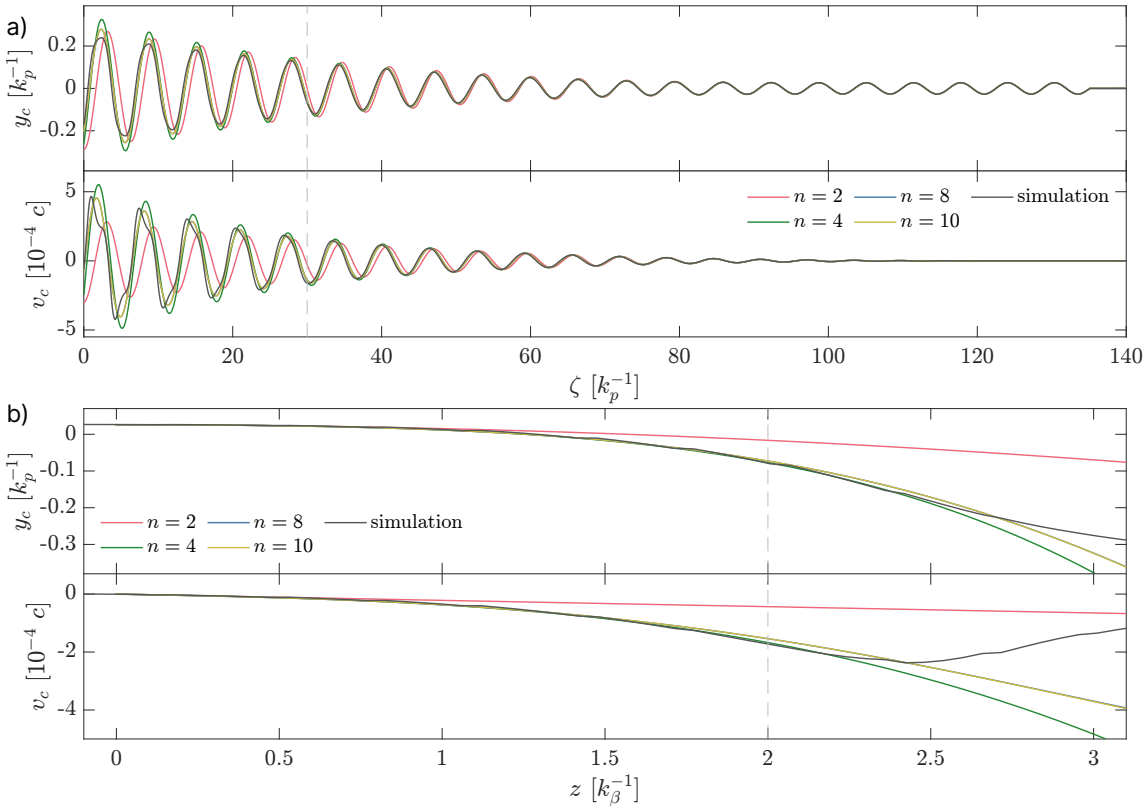

Figure 2.10: Line-outs of the centroid y_c and centroid velocity v_c along ζ at $z = 2\ k_\beta^{-1}$ (a) and along z at $\zeta = 30\ k_p^{-1}$ (b) for a flat-top transverse profile in cylindrical coordinates according to a 3D simulation (dark grey) and the power series model truncated at different terms (colors). The vertical grey dashed lines indicate the position of the line-out along the other dimension. Note that the curves for $n = 8$ and $n = 10$ overlap almost completely.

where $v_c = v_{c,*}/c = dy_c/dz$ is the normalized centroid velocity ($v_{c,*}$ is not normalized), and $y_{c0}(\zeta)$ and $v_{c0}(\zeta)$ are arbitrary initial conditions for the centroid and centroid velocity, respectively.

Figure 2.9 shows a comparison of the power series model truncated at different series terms with a PIC simulation in 2D Cartesian geometry, with $y_{c0}(\zeta) = 0.05 \sin(1.07\ \zeta)$ and $v_{c0}(\zeta) = 0$ (see Table A.1, item A.1.1, in Appx. A for the full simulation details). For the range in ζ we are considering, the truncated solutions are valid up to propagation distances $z \approx k_\beta^{-1}$ [see Fig. 2.9b)]. As expected, a larger number of series terms improves the agreement between the model and simulation, although the improvement seems to saturate at eight series terms (note the overlap between the curves for $n = 8$ and $n = 10$ in Fig. 2.9).

2D cylindrical, flat-top transverse profile

For a flat-top transverse profile, the right-hand side of the centroid differential equation already depends linearly on y_c (see Eq. 2.62). We can define the operator as

$$\mathcal{R}\{y_c\} = 2\ \hat{k}_\beta^2\ I_1(r_b)\ K_1(r_b) \int_\zeta^\infty d\zeta' \sin(\zeta - \zeta') f(\zeta') \left(y_c(\zeta) - y_c(\zeta')\right) , \tag{2.129}$$

and once again replace it in the general model (Eqs. 2.122 and 2.123). Note that the branches of Eq. 2.62 are continuous at $r_b(\zeta) = r_b(\zeta')$ (which is also the case when r_b is constant).

The power series model in this geometry is compared to a 3D PIC simulation in Fig. 2.10, with the initial conditions $y_{c0}(\zeta) = 0.027 \sin(\zeta)$ and $v_{c0}(\zeta) = 0$ (see Table A.2, item A.2.1, in Appx. A for the

full simulation details). Here the accuracy of the model extends to longer distances (both along the bunch and along the propagation distance) than in Fig. 2.9. Figure 2.10b), for example, indicates reasonable agreement can be maintained up to $z \approx 2\,k_\beta^{-1}$, although some signs of nonlinearity have begun to appear at this point [see Fig. 2.10a) for $\zeta = [0, 20]\ k_p^{-1}$].

2.5 Comparison of evolution models

In the last two sections, we have presented two analytical models that can describe the evolution of the bunch centroid as the particle bunch undergoes the HI. Each of these models has different underlying assumptions, as well as advantages and disadvantages. Here we briefly compare the asymptotic and power series models to a 3D PIC simulation with parameters that are representative of the remainder of this dissertation.

It is only possible to compare the asymptotic and power series model directly for a flat-top transverse profile in cylindrical coordinates, and assuming an initial centroid perturbation at k_p. We once again assume the initial centroid $y_{c0}(\zeta) = 0.027\sin(\zeta)$.

To quantify the accuracy of the theoretical models, we average the amplitude of the theoretical ($y_{c,\mathrm{th}}$) and numerical ($y_{c,\mathrm{sim}}$) centroid oscillation over one period (λ_p) and calculate the relative difference between the simulation and the model. The relative error $\Delta|y_c|$ is therefore defined as

$$\Delta|y_c| = \frac{\langle|y_{c,\mathrm{th}}|\rangle_{\lambda_p} - \langle|y_{c,\mathrm{sim}}|\rangle_{\lambda_p}}{\langle|y_{c,\mathrm{sim}}|\rangle_{\lambda_p}}\,. \tag{2.130}$$

Figure 2.11 displays the relative error obtained in this case for the asymptotic model [Fig. 2.11a)] and the power series model truncated at $n = 8$ [Fig. 2.11b)]. Though the asymptotic model can accurately describe the centroid along most of the ζ-range we are considering early in the development of the instability ($z \lesssim 0.2\,k_\beta^{-1}$), the oscillation amplitude quickly explodes along the propagation. We also note that this model diverges at the front of the bunch, as mentioned before (here, for $\zeta \to \zeta_s = 135\ k_p^{-1}$). The power series model, on the other hand, can reproduce the behavior of the centroid to within a few percent accuracy up to $z \lesssim 2\,k_\beta^{-1}$.

We may therefore conclude that asymptotic models are extremely useful to understand qual-

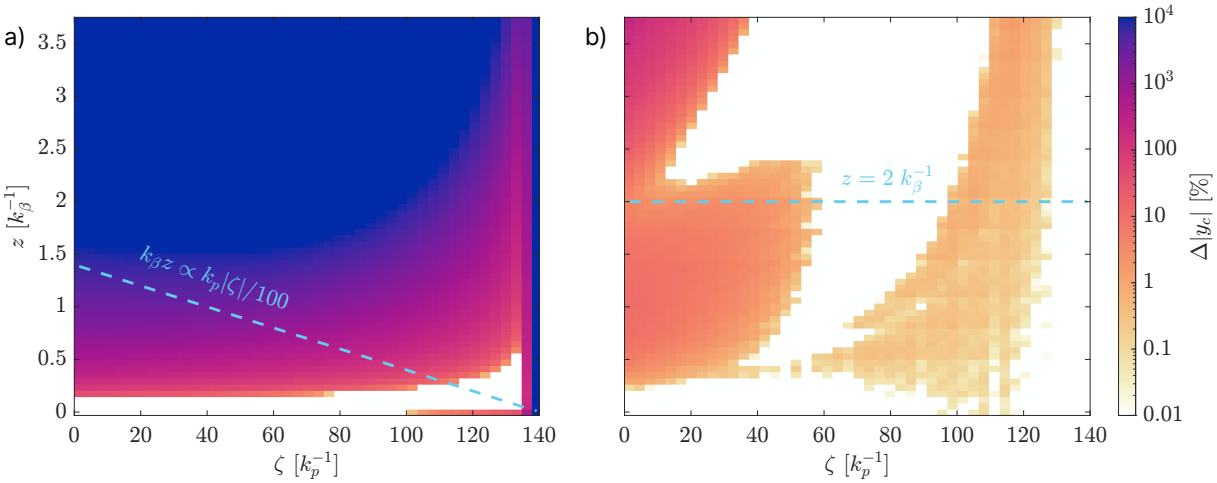

Figure 2.11: Relative error of the asymptotic model (a) and power series model truncated at 8 terms (b) for the evolution of the bunch centroid from an initial seed with respect to a 3D simulation. The approximate validity regions for each model are located beneath the cyan dashed lines. Note that the color scale does not cover the entire range of values in the data.

itatively and analytically the growth rates and development of the hosing and self-modulation instabilities. For a more flexible and quantitative modeling, the power series approach should be the method of choice.

Chapter 3

Properties of the hosing instability

The development of the hosing instability in a particle bunch leads to an increased emittance, and hosing has therefore been seen as a major hindrance for high-quality plasma-based acceleration. In contrast to the self-modulation instability, the unstable oscillation of a bunch centroid can also arise for short bunches (with respect to the wakefield wavelength). In the (short-bunch) blow-out regime [58, 59], there is an assortment of proposed mitigation approaches to choose from [60]. In this regime, hosing may be suppressed through an energy spread (both an initial chirp or inherently induced by the driven wakefields) [61], ion motion [62], or tailored plasma ramps [61].

Currently, fewer mitigation options have been put forward for hosing in the linear wakefield regime. For long bunches there is the additional complexity of the self-modulation instability, which can couple to the long-bunch, linear-wakefield HI and whose growth rate is comparable (see Eq. 2.119). Nevertheless, hosing can be avoided in a fully self-modulated bunch. This requires strongly seeding the SMI [45], which has been accomplished in experiments by letting an ionizing laser pulse propagate with the proton bunch and create the plasma [63]. In the future, SMI seeding may be achieved with a preceding short electron bunch, such that the entire proton bunch self-modulates [40, 64]. When misaligned, this arrangement may seed the growth of hosing. In the case of a short bunch (e.g. a witness bunch) in a linear wake, it has been shown that the HI will naturally saturate at modest levels [65]. However, saturation in the long-bunch case is not yet well understood, both in the presence and absence of the SMI. It would therefore be useful to develop further mitigation methods for hosing in the linear wakefield regime.

Besides mitigation, there are reasons to believe that we may not yet grasp some aspects of the long-bunch HI fully, most prominently the fact that a long-wavelength regime of hosing in long laser pulses was predicted [66] and observed experimentally [67] in the past. Despite some subtle differences, such as the different driver velocity and evolution, the physical and mathematical apparatus that describes the HI and SMI in long laser pulses is analogous enough to long particle bunches that it is worth investigating whether the same conclusions follow.

In this context, the first step in this chapter will be to obtain the dispersion relation for the long-bunch HI, a result that should be analogous to the one for long laser pulses [66]. Following this, we explore the dependence of the hosing growth rate on the seed frequency from a more dynamic perspective that places particular emphasis on the instability's onset, using novel methods and reaching novel conclusions.

3.1 Adiabatic dispersion relation

Our approach to obtain a dispersion relation for the hosing instability is relatively established in plasma physics. Starting from a partial differential equation for the instability in question in the beam co-moving frame, we transform the variables back into the laboratory frame and substitute a plane wave solution.

In this case we start from Eq. 2.89, which assumes a constant bunch radius $r_b(\zeta) = r_{b0} = \text{const}$ and the long-bunch, adiabatic regime ($\partial_\zeta f(\zeta) \to 0$ and $f(\zeta) \approx 1$). We would like to note that Eq. 2.89 can be formulated as two coupled equations for the bunch centroid y_c and the plasma centroid y_ψ [45, 68]:

$$\begin{aligned} \left(\partial_z^2 + \mu\hat{k}_\beta^2\right) y_c &= \mu\hat{k}_\beta^2\, y_\psi \\ \left(\partial_\zeta^2 + 1\right) y_\psi &= y_c\ . \end{aligned} \tag{3.1}$$

Although this step is not necessary to derive the dispersion relation, this formulation makes it clear that the HI can be understood as a coupling between the bunch and plasma centroids in the adiabatic regime and in the limit of small centroid displacements ($y_c \ll 1$).

The theory presented in Ch. 2 was described in the co-moving coordinates (z, ζ), given by $\zeta = z' - c\,t$ and $z = z'$, where (z', t) are the coordinates in the laboratory frame. Before transforming Eq. 2.89 into the laboratory frame, we express it in terms of the unnormalized variables (z_*, ζ_*):

$$\left(\partial_{\zeta_*}^2 + k_p^2\right)\left(\partial_{z_*}^2 + \mu k_\beta^2\right) y_c = \mu k_\beta^2\, k_p^2\, y_c\ . \tag{3.2}$$

Using the chain rule, we can substitute the derivatives in Eq. 3.2 by

$$\partial_{\zeta_*} = -\frac{1}{c}\,\partial_t \tag{3.3}$$

$$\partial_{z_*} = \frac{1}{c}\,\partial_t + \partial_{z'} \tag{3.4}$$

and transform it into the laboratory frame:

$$\left(\partial_t^2 + \omega_p^2\right)\left(\frac{1}{c^2}\partial_t^2 + \frac{2}{c}\,\partial_t\partial_{z'} + \partial_{z'}^2 + \mu k_\beta^2\right) y_c = \mu k_\beta^2\, \omega_p^2\, y_c\ . \tag{3.5}$$

After substituting plane wave solutions of the form $y_c \propto \exp[i(kz' - \omega t)]$ in Eq. 3.5 and rearranging, we obtain the HI dispersion relation:

$$\left(\hat{\omega}^2 - 1\right)\left(\hat{\omega} - \hat{k}\right)^2 - \mu\hat{k}_\beta^2\,\hat{\omega}^2 = 0\ , \tag{3.6}$$

where $\hat{\omega} = \omega/\omega_p$ and $\hat{k} = k/k_p$ are the normalized angular frequency and wavenumber, respectively. Note that this dispersion relation is equivalent to the one for the hosing instability in laser pulses [66], with the exception of the factor $\mu\hat{k}_\beta^2$. We remind the reader that this factor depends on the bunch parameters and is given by

$$\mu\hat{k}_\beta^2 = I_1(r_{b0})\,K_1(r_{b0})\,\frac{n_{b0}}{n_0}\left(\frac{q_b}{e}\right)^2\frac{m_e}{M_b}\,\frac{1}{\gamma}\ . \tag{3.7}$$

We can obtain the growth rate for the HI as a function of the wavenumber k by solving the dispersion relation for ω and taking the imaginary part of $\omega(k)$. The resulting curve is plotted in Fig. 3.1 for different bunch parameters, assuming $n_{b0}/n_0 = 0.001$ and $r_{b0} \approx 0.266\ k_p^{-1}$: for an electron

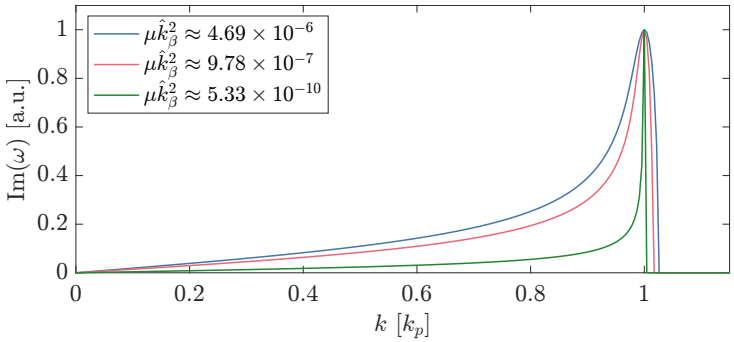

Figure 3.1: Hosing growth rate as a function of the wavenumber for three different bunch parameters, according to the dispersion relation Eq. 3.6.

bunch with $\gamma = 480$ (red) and $\gamma = 100$ (blue), and for a proton bunch with $\gamma = 480$ (green). All three growth rate curves have a maximum at the plasma frequency ($k = k_p$), as expected. In addition, there is a tail that extends to long wavelengths ($k < k_p$, $\lambda > \lambda_p$) and which has been described as long-wavelength hosing in the context of lasers [66]. This tail indicates that oscillations in the bunch centroid may grow at frequencies other than the plasma frequency.

By assuming that the centroid takes the form of a plane wave, which extends infinitely in space and whose time and space dependences are factorable, this approach precludes any spatiotemporal effects (like the ones built into the asymptotic growth rates discussed in Sec. 2.3). Though the result we obtained in Eq. 3.6 and Fig. 3.1 is significant for the understanding of the HI in particle bunches, we will show in the next section how this is not a complete picture of the instability's frequency response.

3.2 Dynamic amplitude response

In Sec. 2.4 we discussed the general form of the differential equations for the beam moments $m(\zeta, z)$ associated with the HI and SMI and we pointed out that the right-hand side of these equations is always proportional to $m(\zeta, z)$ when we assume to be in the initial stage of the instability (see p. 34). More specifically, the integral over ζ' in the right-hand side will consist of two terms that are proportional to either $m(\zeta)$ or $m(\zeta')$ (see Eq. 2.62 or Eq. 2.109). This means that these equations can be written in the form of a harmonic oscillator in z. For hosing in cylindrical geometry and a flat-top transverse profile, for example, we can write Eq. 2.62 as

$$\left(\frac{d^2}{dz^2} + k_{\mathrm{HO}}^2(\zeta, z)\right) y_c(\zeta, z) = F(\zeta, z, y_c) \,, \tag{3.8}$$

where $k_{\mathrm{HO}}^2(\zeta, z)$ corresponds to a natural frequency (note that k may be interpreted as a frequency via $f = \frac{k\,c}{2\pi}$) and $F(\zeta, z, y_c)$ to a driving force. In this case these quantities are given by

$$k_{\mathrm{HO}}^2(\zeta, z) = -2\,\hat{k}_\beta^2 \int_\zeta^\infty d\zeta' \sin(\zeta - \zeta') f(\zeta') \frac{r_{b0}^2(\zeta')}{r_b(\zeta') r_b(\zeta)}\, I_1(r_{b<})\, K_1(r_{b>}) \tag{3.9}$$

$$F(\zeta, z, y_c) = -2\,\hat{k}_\beta^2 \int_\zeta^\infty d\zeta' \sin(\zeta - \zeta') f(\zeta') \frac{r_{b0}^2(\zeta')}{r_b(\zeta') r_b(\zeta)}\, I_1(r_{b<})\, K_1(r_{b>})\, y_c(\zeta') \,. \tag{3.10}$$

Strictly speaking, Eq. 3.8 corresponds to a parametric oscillator, i.e., a harmonic oscillator whose system parameters (resonance frequency and/or damping) are allowed to vary periodically. This degree of freedom can lead to amplifying or damping behavior, depending on the tuning of the

system parameter oscillation.

On the other hand, if we decouple the bunch and the plasma (see Eq. 3.1), and purely consider the initial plasma response to a bunch density perturbation, we can identify the simpler case of a sinusoidally driven harmonic oscillator. To demonstrate this, let us recall that the plasma density perturbation $\delta n/n_0$ induced by the presence of a particle bunch is given by [9]:

$$\left(\frac{d^2}{d\zeta^2}+1\right)\frac{\delta n}{n_0}=q_b\frac{n_b}{n_0}\ . \tag{3.11}$$

If we assume that the bunch profile n_b contains an initial centroid perturbation of the form $y_{c0}(\zeta)\propto \sin(k\,\zeta)$, this dependence will be encoded in the right-hand side to Eq. 3.11, which will act as a sinusoidal force driving the harmonic oscillator δn (with its resonant frequency k_p). By varying the frequency of the driving force in such a system, once again, it is possible to obtain different growth behaviors (amplifying or damping).

Both of these interpretations of the theory that describes the HI motivate us to map the dependence of the oscillation amplitude on a hosing seed frequency. Before we explore this dependence using a different, transient approach with respect to the previous section, we would like to briefly revisit some key properties of the sinusoidally driven harmonic oscillator.

3.2.1 Sinusoidally driven damped harmonic oscillator

Consider the case of a simple damped harmonic oscillator driven by a sinusoidal force with frequency ω:

$$\left(\partial_t^2+2D\,\partial_t+\omega_0^2\right)x(t)=A\,\cos(\omega t)\ , \tag{3.12}$$

where D is the damping constant, ω_0 is the resonant frequency of the oscillator, $x(t)$ is the position, and A is the amplitude of the driving force. The solution for large t is given by (see for example [69, pp. 111-115])

$$x(t)=A\,\Pi(\omega)\cos\Big(\omega t-\phi(\omega)\Big)\ , \tag{3.13}$$

where the amplitude response $\Pi(\omega)$ and the phase shift $\phi(\omega)$ are defined by

$$\Pi(\omega)=\frac{1}{\sqrt{\left(\omega_0^2-\omega^2\right)^2+\left(2D\,\omega\right)^2}}\ , \tag{3.14}$$

$$\tan\phi=\frac{2D\,\omega}{\omega_0^2-\omega^2}\ . \tag{3.15}$$

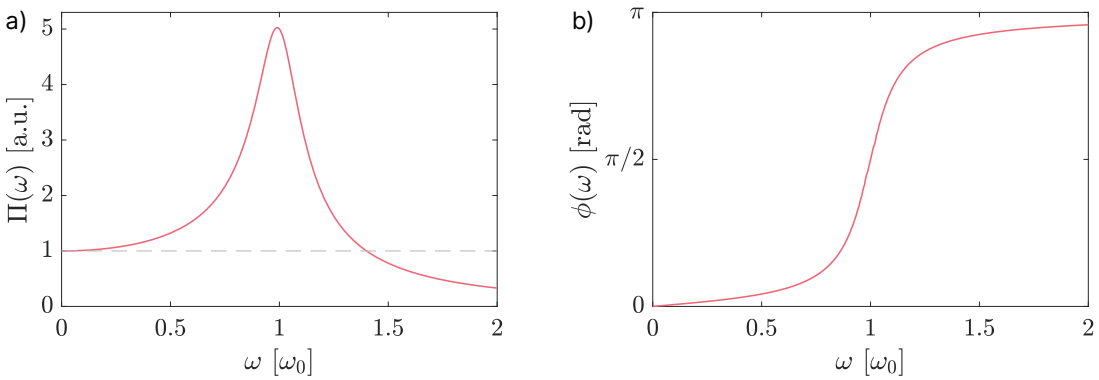

Figure 3.2: Amplitude response (a) and phase shift (b) of a sinusoidally driven damped harmonic oscillator, for a damping constant $D/\omega_0=0.1$.

When the driving frequency matches the resonant frequency ($\omega = \omega_0$), the oscillation amplitude is of course maximum [see Fig. 3.2a)] and the oscillation lags the driving force by $\pi/2$ [see Fig. 3.2b)]. Note that the "phase jump" illustrated in Fig. 3.2b), from 0 to π, is characteristic of this system.

3.2.2 The hosing amplitude response

Our goal is to measure the amplitude response (or growth rate) of the HI as a function of the seed frequency. We will again consider a sinusoidal hosing seed, $y_{c0}(\zeta, k) = 0.05 \sin(\zeta\ k/k_p)$, where k is an arbitrary wavenumber. In order to measure the HI amplitude response, we calculate the ratio between the centroid after the propagation distance z and the initial centroid. The measured amplitude response is therefore defined as

$$\Pi(k, z) = \frac{\int_L |y_c(z, \zeta)|\, d\zeta}{\int_L |y_{c0}(\zeta, k)|\, d\zeta}\ , \tag{3.16}$$

where L is the length of some region of interest along the bunch. Here we will consider a window measuring $L = 140\ k_p^{-1}$, which represents around $22\ \lambda_p$. Note that this amplitude response does not correspond to the one defined in Eq. 3.14, which contains no information about the phase (as opposed to Eq. 3.16).

We can determine the amplitude response $\Pi(k, z)$ theoretically as long as we can describe the evolution of the centroid and replace it for $y_c(z, \zeta)$. During the initial propagation in plasma, we can assume a constant (z-independent) plasma response, which we can designate $\langle F_{y0} \rangle$, driven by the centroid perturbation y_{c0}. The solution to Eq. 2.15 (the differential equation for the bunch centroid) is then simply:

$$y_c(\zeta, z) = y_{c0}(\zeta) + \tfrac{1}{2}\ z^2 \cdot \left(\frac{m_e}{\gamma M_b}\ \langle F_{y0} \rangle \right)\ . \tag{3.17}$$

Note that this corresponds to the power series model described in Sec. 2.4 truncated to first order (at $n = 2$). This assumption is valid within the typical timescale for bunch evolution, given by the betatron period $k_\beta^{-1} = c/\omega_\beta$.

For our analysis of the transient amplitude response we will consider a relativistic ($\gamma = 480$) electron bunch with $n_{b0} = 0.001\ n_0$ in 2D Cartesian geometry and with a Gaussian transverse profile, with the RMS transverse size $\sigma_y \approx 0.27\ k_p^{-1}$. The longitudinal component of the bunch profile $n_b(\zeta, y) = n_{b0} \cdot f(\zeta) \cdot g(y, \zeta)$ is defined as

$$f(\zeta) = \frac{1}{2}\ \left(1 + \cos\left(\sqrt{\frac{\pi}{2}} \frac{\zeta - \zeta_c}{\sigma_z} \right) \right)\ , \tag{3.18}$$

where $\sigma_z \approx 160\, k_p^{-1}$ is the RMS longitudinal size, $\zeta_c = \zeta_s - \sqrt{2\pi}\sigma_z$ is the location of the bunch center, $\zeta_s = 135\ k_p^{-1}$ is the location of the bunch front, and $f(\zeta)$ is bounded by the limits $\zeta = \pm\sqrt{2\pi}\sigma_z + \zeta_c$. In this case, and assuming that the bunch envelope stays constant at σ_y, the plasma response is given by (see p. 17)

$$\begin{aligned} \langle F_y \rangle = \sqrt{\frac{\pi}{8}} \frac{n_{b0}}{n_0} \left(\frac{q_b}{e} \right)^2 \sigma_y\ \exp(\sigma_y^2) \int_\zeta^\infty d\zeta' \sin(\zeta - \zeta')\, f(\zeta') \\ \left\{ \exp\left[y_c(\zeta') - y_c(\zeta) \right]\ \operatorname{erfc}\left[\frac{y_c(\zeta') - y_c(\zeta) + 2\,\sigma_y^2}{2\,\sigma_y} \right] \right. \\ \left. - \exp\left[y_c(\zeta) - y_c(\zeta') \right]\ \operatorname{erfc}\left[\frac{y_c(\zeta) - y_c(\zeta') + 2\,\sigma_y^2}{2\,\sigma_y} \right] \right\}\ . \end{aligned} \tag{3.19}$$

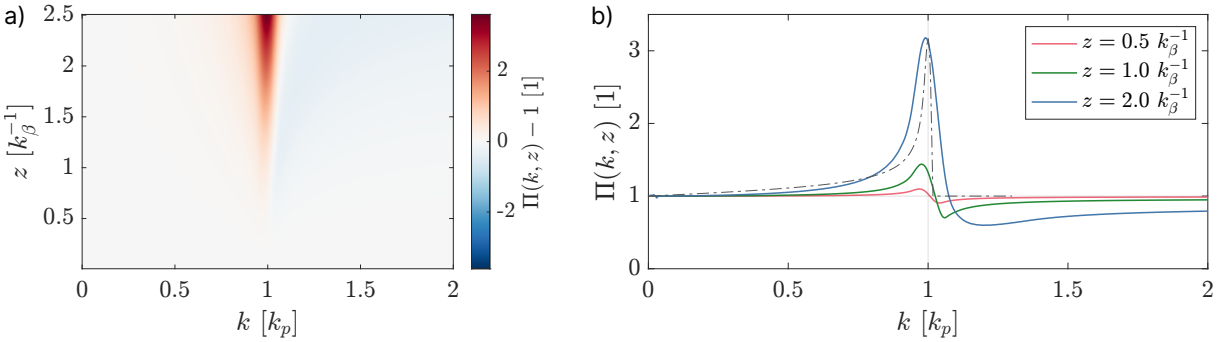

Figure 3.3: Hosing amplitude response as a function of seed wavenumber and propagation distance according to theory: full evolution (a) and line-outs at different distances (b), where the grey dash-dotted line represents the dispersion relation Eq. 3.6 in arbitrary units.

The resulting amplitude response $\Pi(k, z)$ according to theory (calculated numerically) is shown in Fig. 3.3a), where 1 has been subtracted from the data in order to clearly distinguish between areas where the initial oscillation amplitude has grown (red) or decreased (blue). This damping effect for short wavelengths ($k > k_p$), in fact, has not been previously predicted, either in the context of the HI in particle beams or laser pulses. As expected, the maximum growth is progressively observed at the plasma frequency ($k = k_p$), which is also evident in the line-outs of Fig. 3.3b) (see blue curve).

The amplitude response corresponding to the adiabatic dispersion relation in Eq. 3.6, which is proportional to $\exp[\mathrm{Im}(\omega)]$, has been included in Fig. 3.3b) as a grey dash-dotted line for comparison. Although this method of computing the hosing amplitude response has equally yielded a long-wavelength tail, there are obvious differences between this amplitude response at later times [see blue curve in Fig. 3.3b)] and the adiabatic dispersion relation, which, for example, does not predict a damping regime ($\Pi(k, z) < 1$). Additionally, note that the late-time curve for $\Pi(k, z)$ (at $z = 2\ k_\beta^{-1}$) bears both similarities and differences with respect to the harmonic oscillator case in Fig. 3.2a): though both amplitude responses peak at the resonance frequency and are unity for a zero frequency, the HI amplitude response does not converge to zero for infinitely large frequencies [see blue curve in Fig. 3.3b) as $k \to \infty$].

A particularly interesting aspect of Fig. 3.3b) is the shape of the early amplitude response ($z \lesssim k_\beta^{-1}$, red and green curves). We take a closer look at this regime in Fig. 3.4a), and validate the curve at $z = k_\beta^{-1}$ against 2D Cartesian PIC simulations with the same bunch parameters as above (see Table A.1, item A.1.3, in Appx. A for the full simulation details). There is excellent agreement between theory and simulations. We note that an identical theoretical curve can be obtained

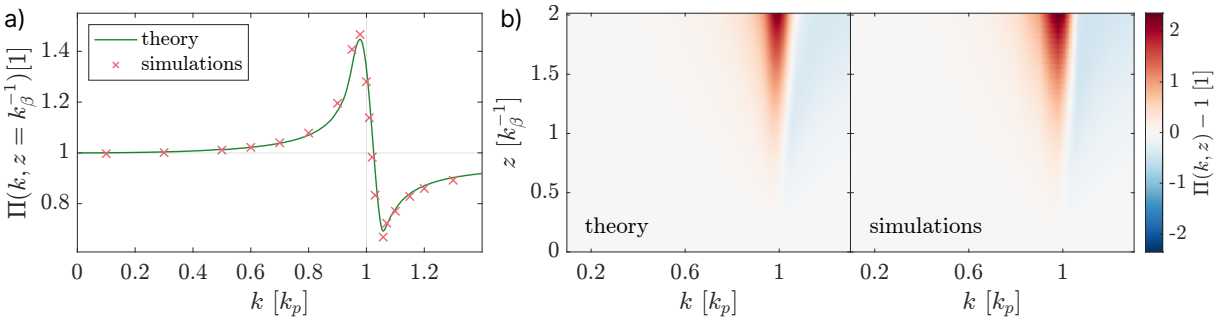

Figure 3.4: a) Hosing amplitude response according to theory (green line) and simulations (red crosses) at $z = k_\beta^{-1}$, where each cross symbol represents a simulation initialized with a centroid perturbation at k. b) Comparison of the amplitude response along z according to theory and simulations (interpolated linearly along k).

in cylindrical coordinates (assuming $y_c \ll 1$), but a comparison to 3D simulations would have been much more computationally expensive. These effects are therefore not limited to a 2D slab geometry and in fact we use 3D simulations later in this dissertation to explore the implications of this result.

In contrast to later times, the magnitudes of maximum growth ($\Pi(k,z) > 1$) and damping ($\Pi(k,z) < 1$) in Fig. 3.4a) are identical, and their locations on the k spectrum in close proximity. This means that these two radically different growth regimes are potentially accessible with only a small amount of detuning, or frequency shift (in k). After some propagation in plasma not only does the magnitude of resonant growth ($k \approx k_p$) become several times that of maximum damping, but the locations of both extrema, $k_{\max}$ and $k_{\min}$, shift with increasing z, with $k_{\max} \to k_p$ and $k_{\min} \to \infty$ [see Fig. 3.3a)]. A further observation is that the maximum growth is not attained for $k = k_p$ (as generally assumed for the HI) during this initial phase of propagation, but at a slightly lower value ($k \approx 0.98\, k_p$, estimated numerically). Note that the location of this maximum depends on the particular bunch and plasma parameters, and moves along the propagation distance.

Figure 3.4b) demonstrates that the power-series-based theoretical model can accurately reproduce the amplitude response up to two betatron periods of propagation. Note that the simulation data, which is very sparse along the k axis, has been interpolated linearly to render a comparable image.

The explanation for the behavior displayed on Fig. 3.4a) is connected to the phases of the oscillations of the bunch centroid and the plasma response, which will be demonstrated in the following section.

3.2.3 The hosing phase response

To understand the early amplitude response of the HI, we can study the immediate plasma response to a centroid perturbation, i.e., $\langle F_{y0} \rangle$. We are particularly interested in the relative phase shift between this oscillation and the "force" driving it (the initial perturbation y_{c0}).

Figure 3.5a) shows the initial centroid and the initial plasma response $\langle F_{y0} \rangle$ for three different seed wavenumbers, as obtained from the 2D PIC simulations represented in Fig. 3.4. These three wavenumbers illustrate the three different growth regimes we can identify in the hosing amplitude response [see Figs. 3.3 and 3.4]:

- slow growth ($k < k_p$),
- resonant growth ($k = k_p$),
- damping ($k > k_p$).

For $k = 0.9\, k_p$ (slow growth), the plasma response is almost in phase with the centroid perturbation [see Fig. 3.5a), top]. Conversely, $\langle F_{y0} \rangle$ is almost fully out of phase for $k = 1.1\, k_p$ [see Fig. 3.5a), bottom], thus acting in the opposite direction of the perturbation y_{c0} at every slice and justifying the damping effect. For $k = k_p$ (resonant growth), the wakefield response lags the centroid perturbation by $\pi/2$, which we might expect based on the phase behavior of the sinusoidally driven damped harmonic oscillator (see p. 44).

Since $\langle F_y \rangle$ initially oscillates at k (along ζ), a phase shift $\Delta\phi$ between both periodic curves can be measured straightforwardly. The relationship between $\Delta\phi$ and k is shown in Fig. 3.5b), as obtained from the 2D simulations and the theoretical $\langle F_{y0} \rangle$, using a cross-correlation method (see Appx. B for further details).

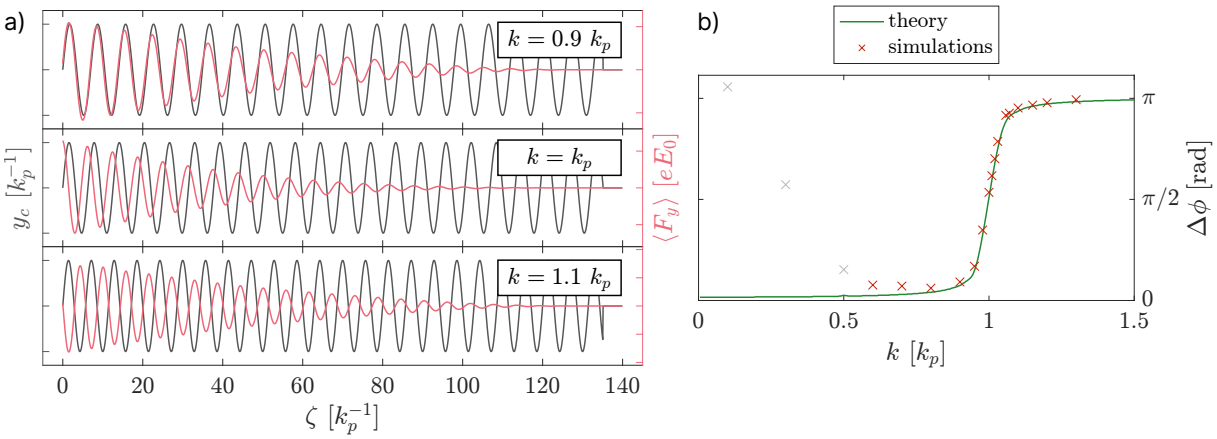

Figure 3.5: a) Initial centroid (dark grey) and average transverse force (red) for three different seed wavenumbers, obtained from 2D simulations at $z = 0$. b) Phase shift between the initial y_c and $\langle F_y \rangle$ as a function of the seed wavenumber, obtained from theory (green) and simulations (red cross symbols).

There is excellent agreement between theory and simulations for $k > 0.5\ k_p$. The simulation data points for $k \leq 0.5\ k_p$ [grey cross symbols in Fig. 3.5b)] are not valid, since the simulation window length becomes comparable to the perturbation wavelength ($L/\lambda \lesssim 10$). The theoretical curve was obtained by scaling the nominal window and bunch lengths ($L = 140\ k_p^{-1}$ and $\sigma_z \approx 160\ k_p^{-1}$) by $1/k$, thereby encompassing several periods in the analysis.

The three growth regimes are again evident in Fig. 3.5b): two asymptotes at $\Delta\phi = 0$ and $\Delta\phi = \pi$, corresponding to the slow growth and damping regimes, respectively, and a transition region where $\Delta\phi$ crosses $\pi/2$, corresponding to the resonant regime. Note that the phase behavior of the sinusoidally driven damped harmonic oscillator illustrated in Fig. 3.2b) is identical to the phase shift curve obtained in Fig. 3.5b).

3.3 A new mitigation method

Figure 3.3 suggests that there is a range of wavenumbers where the amplitude response is, either temporarily or consistently, below one. This leads to the following immediate question: can this damping regime be used to suppress the hosing instability?

One might consider operating exclusively in the damping regime, thereby not only preventing the growth of hosing but also even reducing the initial seed amplitude. This does not work, however, as we demonstrate in the following.

Let us assume that that the centroid evolves as $y_c(\zeta, z) = A(z)\ \sin[k\zeta - \varphi(z)]$, where $A(z)$ and $\varphi(z)$ are a time-evolving oscillation amplitude and phase shift, respectively. The corresponding (normalized) centroid velocity, defined as $v_c = v_{c,*}/c = dy_c/dz$, would therefore evolve according to

$$\begin{aligned} v_c(\zeta, z) &= A'(z)\ \sin[k\zeta - \varphi(z)] - A(z)\ \varphi'(z)\ \cos[k\zeta - \varphi(z)] \\ &= A'(z)\ \sin[k\zeta - \varphi(z)] + A(z)\ \varphi'(z)\ \sin[k\zeta - \varphi(z) - \frac{\pi}{2}]\,, \end{aligned} \tag{3.20}$$

where the prime denotes a derivative in z. Early in the propagation, the amplitude varies slowly and we can neglect the first term in Eq. 3.20. The centroid velocity $v_c \propto \sin[k\zeta - \varphi(z) - \frac{\pi}{2}]$ and the centroid $y_c \propto \sin[k\zeta - \varphi(z)]$ are therefore shifted with respect to each other by $\frac{\pi}{2}$. Since what determines the growth regime is the relative phase shift between each quantity and $\langle F_y \rangle$, this means that the initial plasma response will impact y_c and v_c differently. Along the propagation, the

phase-shifted term of v_c (second term of Eq. 3.20) may become less dominant.

Naturally, we have not avoided the HI by eliminating the centroid displacement yet allowing significant transverse momentum to build (in the form of the centroid velocity). The reasoning above demonstrates that we must alternate between the two non-resonant growth regimes in order for an attempt at mitigation to work, such that we can suppress both y_c and v_c. To evaluate the degree of hosing mitigation, we must define a measure that takes both of these quantities into account.

An energy conservation equation can be obtained by multiplying Eq. 3.8 by v_c:

$$\frac{d}{dz}\Big(\underbrace{\tfrac{1}{2}\, v_c^2(\zeta,z)}_{\mathcal{E}_{\mathrm{kin}}(\zeta,z)} + \underbrace{\tfrac{1}{2}\, k_{\mathrm{HO}}^2(\zeta,z)\, y_c^2(\zeta,z)}_{\mathcal{E}_{\mathrm{pot}}(\zeta,z)} \Big) = v_c(\zeta,z)\; F(\zeta,z,y_c)\;, \tag{3.21}$$

which allows us to define a kinetic and a potential energy $\mathcal{E}_{\mathrm{kin}}$ and $\mathcal{E}_{\mathrm{pot}}$, respectively, in analogy with a conventional harmonic oscillator. The energy source term (the right-hand side of Eq. 3.21) represents an effective force acting on each slice of the bunch centroid, which moves with v_c. In reality, energy conservation is not guaranteed by Eq. 3.21 due to the same assumptions underlying Eq. 3.8, namely that k_p, k_β and the bunch density profile do not change over time. This equation is nevertheless useful to us since it provides an overall measure of the transverse energy associated with the growth of the HI, defined as

$$\begin{aligned} \mathcal{E}(\zeta,z) &= \mathcal{E}_{\mathrm{kin}}(\zeta,z) + \mathcal{E}_{\mathrm{pot}}(\zeta,z) \\ &= \tfrac{1}{2}\, v_c^2(\zeta,z) + \tfrac{1}{2}\, k_{\mathrm{HO}}^2(\zeta,z)\, y_c^2(\zeta,z)\;. \end{aligned} \tag{3.22}$$

The ensuing issue is how to access the different growth regimes. In a realistic set-up, although we might conceivably choose the seed wavenumber (the initial perturbation frequency), we cannot control k as the bunch evolves in the plasma. However, we can control the local plasma density and therefore the ratio of k (fixed in the centroid perturbation) to the local plasma wavenumber k_p, thereby operating in different growth regimes.

For this shifted perspective, let us consider a reference plasma density n_0 (e.g. $n_0 = 0.5 \cdot 10^{-14}\ \mathrm{cm}^{-3}$) and a bunch with fixed, physical-unit parameters (e.g. $\sigma_z = 12\ \mathrm{cm}$), seeded with a centroid perturbation at the plasma frequency corresponding to n_0, which we can define as $k_{p,0}$. If we now vary the density n_p of the plasma in which this bunch propagates, the seed at $k_{p,0}$ will be either above or below the resonant wavenumber k_p given by n_p, which means that we can probe the amplitude response at different frequencies in that plasma. Note that the normalized bunch parameters will equally scale with n_p (e.g. $\frac{n_{b0}}{n_p} \neq \frac{n_{b0}}{n_0}$ or $k_p\sigma_z \neq k_{p,0}\sigma_z$), which impacts the wakefield properties.

We can obtain the theoretical amplitude response as a function of the local plasma density n_p using the same procedure as in Fig. 3.3. Here, the bunch has the parameters described on p. 45 at a plasma density $n_0 = 0.5 \cdot 10^{-14}\ \mathrm{cm}^{-3}$. The amplitude of the initial centroid perturbation is the only quantity which is not fixed in physical units, and is instead kept at the same normalized value ($0.01\ k_p$) for all densities n_p. The result is shown in Fig. 3.6a). The shape of the early amplitude response is visible in Fig. 3.6b), where line-outs were taken at $z = 0.5\ k_\beta^{-1}$ (red) and $z = k_\beta^{-1}$ [green, compare with Fig. 3.4a)]. Note that the locations of the maximum growth and maximum damping at $z = k_\beta^{-1}$ are more asymmetric with respect to the resonance as a function of n_p than as a function of k [Fig. 3.4a)].

As argued above, a mitigation set-up would require propagating the hosed or seeded bunch through plasma sections with different densities. In fact, “plasma density detuning” has been

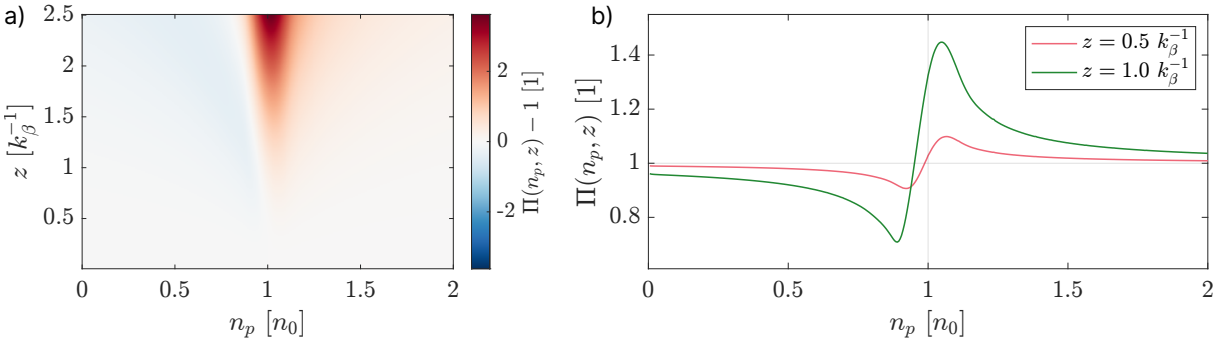

Figure 3.6: Hosing amplitude response as a function of relative plasma density and propagation distance according to theory: full evolution (a) and line-outs at different distances (b).

mentioned before as a way to potentially mitigate the HI in laser pulses [70] and, more specifically, the use of a plasma density step has been proposed to control the SMI in particle bunches [71, 72].

The power series model can be applied to a varying plasma density n_p as long as we assume that the density does not change at the length scale of k_β^{-1}. Our goal is to treat the plasma density changes as instant and therefore neglect the dependence of n_p on z. In that case, we can normalize the entire model to the local plasma density in each section, and use it to estimate the optimal density profile for mitigation purposes. If we assume a simple step-like profile, for example, the free parameters are the "height" of each step, Δn_i, its length, Δz_i, and the total number of steps. A set of optimal parameters can be found through a numerical parameter scan based on the power series model, although there is a significant limitation in the fact that the model is only valid for $z \lesssim k_\beta^{-1}$.

As a proof of concept, we present two configurations based on one and two pairs of plasma density steps, shown in the inset of Fig. 3.7a). The parameters for these density steps were found by experimenting with the power series model. In order to test the effect of these density profiles, we simulate the propagation of an electron bunch seeded at $k_{p,0}$ either through the density steps or through resonant plasma (at the constant density n_0) in 3D geometry (see Table A.2,

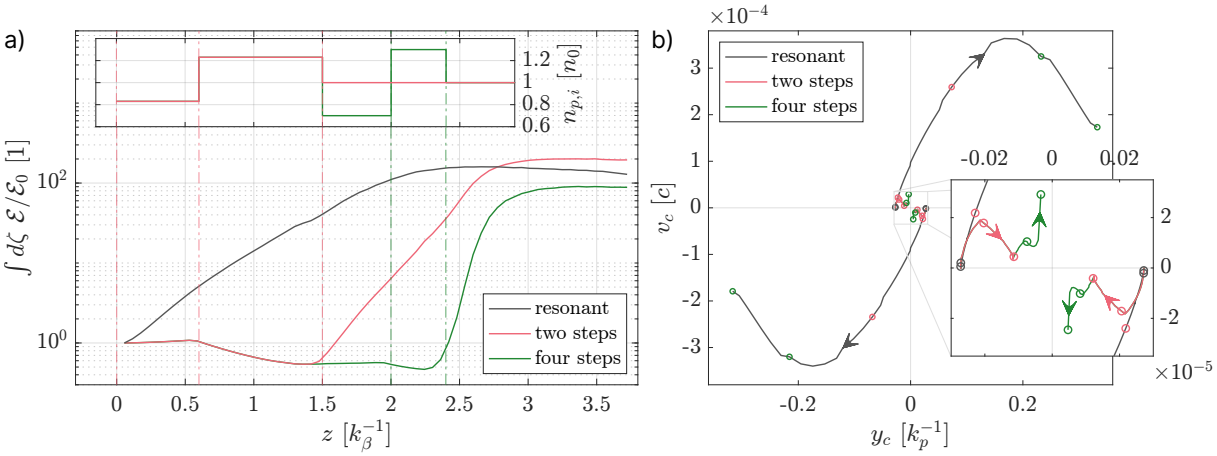

Figure 3.7: Centroid data obtained from three OSIRIS 3D simulations. a) Transverse energy of the bunch relative to the initial value along the plasma (integrated over the simulation domain): plasma at n_0 (grey), with two density steps (red), and with four density steps (green). Inset: plasma density profiles of the two density step configurations. The vertical dash-dotted lines indicate the boundaries of each density step. b) Centroid phase space at two neighboring positions along the bunch, $\zeta \approx 1.5\ k_p^{-1}$ and $\zeta \approx 4.7\ k_p^{-1}$, for all three cases, up to either $z = 2.4\ k_\beta^{-1}$ (grey and green curves) or $z = 1.5\ k_\beta^{-1}$ (red curve). The unfilled circles represent the beginning of the plasma (grey) and the locations of each density step (red and green). Inset: magnified view of central region.

items A.2.1–A.2.3, in Appx. A for the full simulation details). The bunch profile is transversely a flat top with $r_{b0} \approx 0.27\ k_{p,0}^{-1}$ and longitudinally cosinusoidal, and the inital centroid is given by $y_{c0}(\zeta) = 0.027 \sin(\zeta)$ (note that ζ is normalized to $k_{p,0}^{-1}$). Note that, for an arbitrarily shaped initial centroid, the fastest growing mode is sinusoidal, which means that this strategy would suppress the growing component of any seed. Once again, the simulation domain comprises only the head of the bunch, with a length $L = 140\ k_p^{-1}$, corresponding to around $22\ \lambda_{p,0}$.

Figure 3.7a) displays the the resulting transverse energy as a function of the propagation distance. The wavenumber $k_{\mathrm{HO}}^2(\zeta, z)$, necessary for obtaining $\mathcal{E}(\zeta, z)$ (see Eq. 3.22), is computed directly from the z-evolving simulation data. In this geometry, $k_{\mathrm{HO}}^2(\zeta, z)$ is given by Eq. 3.9, where the normalized longitudinal profile $f(\zeta', z)$ is measured on axis. For a complete picture of the beam at every time step, we normalize $\mathcal{E}(\zeta, z)$ to the initial energy $\mathcal{E}_0(\zeta)$ and integrate this along ζ over the simulation window.

After two density steps [compare grey and red curves in Fig. 3.7a), at $z = 1.5\ k_\beta^{-1}$], the energy is smaller than in the resonant case by almost two orders of magnitude (and lower than $\mathcal{E}_0$, the initial value associated with the seed). It is possible to extend this suppressive effect by stacking a further pair of density steps with specific parameters, as demonstrated by the green curve in Fig. 3.7a), where the transverse energy has been lowered even further after four density steps. The full bunch distribution as well as the centroid after each pair of density steps is visible in Fig. 3.8 (first three rows). Note the increasing effect of self-focusing after $z \sim 2\ k_\beta^{-1}$ (see xz projections in Fig. 3.8).

The effect each detuned section has on the bunch centroid and centroid velocity is illustrated in Fig. 3.7b), where the evolution of these quantities along the density steps is plotted as a "centroid phase space". Two locations along the bunch are represented in Fig. 3.7b), corresponding to a consecutive peak and trough in the initial centroid oscillation (shown in Fig. 3.8 as two grey dashed lines in the xy projection at $z = 0$). The first density step prevents some growth in v_c, while the second step decreases the amplitudes of both y_c and v_c [compare grey and red curves in the magnified inset of Fig. 3.7b)]. A third density step can suppress some of the centroid displacement at the expense of a small momentum increase, but it is clear that the fourth step is approaching the limits of this suppression mechanism, since the momentum is now allowed to rise quickly [see green curves in the magnified inset of Fig. 3.7b)].

After both density step configurations, however, the growth rate tends to be exacerbated and saturation is reached at similar transverse energy levels as in the resonant case, as made obvious in Fig. 3.7a) or Fig. 3.8 (bottom row).

3.3.1 Limitations

The analysis performed in Fig. 3.7 suggests that the growth of the HI is temporarily delayed rather than fully avoided. To try to understand the reason for this, we can analyze the behavior of the plasma response along the propagation.

The transition from the density steps back to resonant plasma seems to be associated with a sudden increase of the average transverse force acting on the bunch centroid, as demonstrated in Fig. 3.9a) (solid lines). This field increase can be at least partly explained by the higher degree of self-focusing observed with any of the density step configurations in comparison to the constant-density case [see dashed curves in Fig. 3.9a)].

A further explanation for the increase likely stems from the realignment of the "suppressed" centroid with the plasma response after each density step configuration, at an ideally resonant phase shift of $\pi/2$. This is visible in Fig. 3.9b), which displays the relative phase shift between $\langle F_y \rangle$

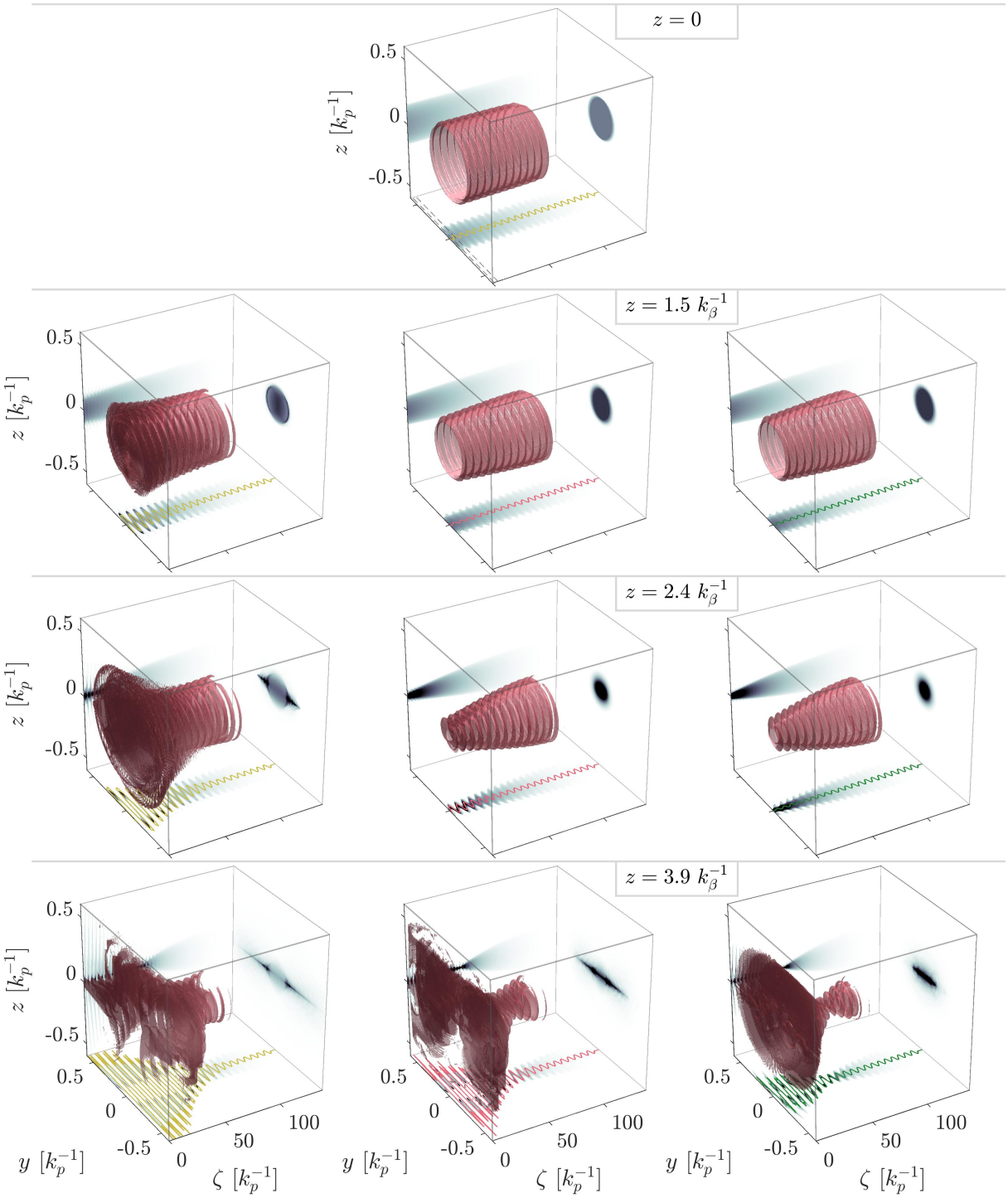

Figure 3.8: Bunch distribution data from three OSIRIS 3D simulations. Isosurfaces (pink volume) and projections (grey color scale) of the bunch density at four different propagation distances (rows) in resonant plasma (left column, yellow curves), with two density steps (center column, red curves), and with four density steps (right column, green curves). The centroid for each case is plotted on the xy projection. The two grey dashed lines in the xy projection at $z = 0$ mark the positions along ζ at which the centroid phase space of Fig. 3.7b) is measured.

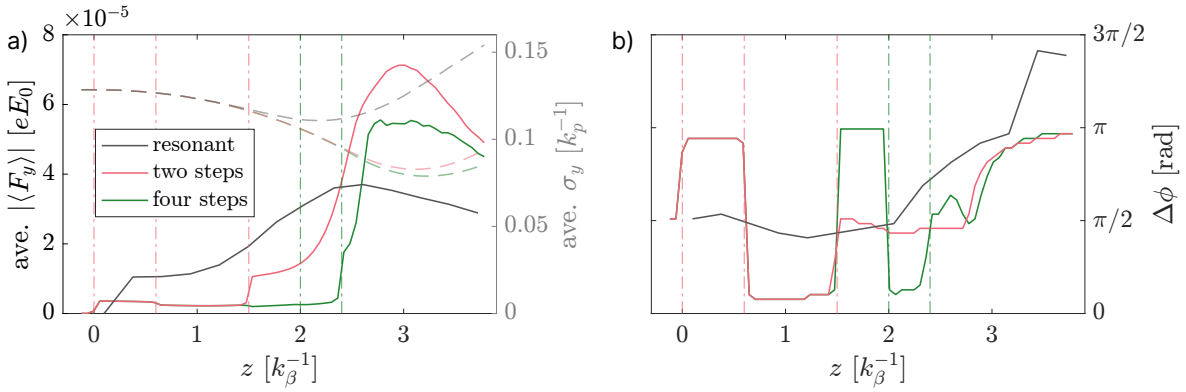

Figure 3.9: Analysis of the transverse wakefield forces in three OSIRIS 3D simulations: resonant plasma (dark grey curves), two-step density profile (red curves) and four-step density profile (green curves). a) Amplitude of $\langle F_y \rangle$ (solid lines), and RMS bunch size along y (dashed, semi-opaque lines), both averaged longitudinally over the simulation domain. b) Relative phase shift between $\langle F_y \rangle$ and the centroid y_c. The vertical dash-dotted lines indicate the density-step transitions in the plasma density profile.

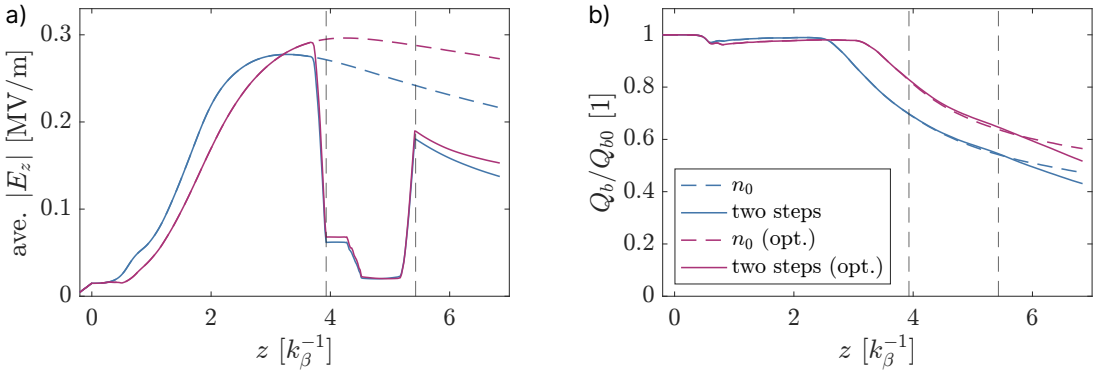

Figure 3.10: Impact of a two-step configuration for hosing mitigation [see inset of Fig. 3.7a), red line] on a self-modulated bunch, measured in four OSIRIS 2D cylindrical simulations. Average amplitude of the longitudinal wakefields (a) and relative bunch charge (b) along the plasma, with (solid lines) and without (dashed lines) the two-step configuration, and with (purple) and without (blue) an early SMI-optimizing density step. The vertical grey dashed lines delimit the two density steps (for hosing mitigation). The average of $|E_z|$ is taken longitudinally over the simulation domain and up to a radius $r = k_p^{-1}$ and the bunch charge is summed up to $r = k_p^{-1}$.

and y_c along the propagation, at $z = 1.5\ k_\beta^{-1}$ for the two-step configuration (red line) and $z = 2.4\ k_\beta^{-1}$ for the four-step configuration (green line). Eventually, however, saturation is reached, and this seems to be associated with the phase shift converging to π [compare with the energy saturation levels observed in Fig. 3.7a)].

A realistic set-up where linear, long-bunch hosing would need to be suppressed would likely involve the self-modulation instability as a desirable method to manipulate the wakefield driver. It would therefore be important for this mitigation approach not to have a large impact on the benefits brought on by the SMI. However, this is not exactly the case, according to Fig. 3.10a), and this therefore constitutes a further limitation of this hosing mitigation approach.

Using simulations in 2D cylindrical axisymmetric geometry, where hosing is unobservable, we can test the direct impact of the two-step configuration [red line in the inset of Fig. 3.7a)] on a self-modulated bunch. We let the electron bunch self-modulate approximately until the instability's saturation and then traverse the two density steps. The simulation parameters are identical as before, with the exception of the bunch profile (transversely Gaussian, cut abruptly at the bunch center to emulate an ionization front) and the longitudinal window size ($L = 280\ k_p^{-1}$) (see Table A.4 in Appx. A for the full simulation details). We also consider the case where a small density step is introduced early in the SMI development with the purpose of extending the high field amplitude after its saturation [71, 72].

The resulting accelerating field amplitude is plotted in Fig. 3.10a) for all cases. Even though the average amplitude recovers after the steps (bounded by the vertical dashed lines), there is still a decrease of around 36% (blue curves, no SMI optimization) or even 44% (purple curves, with SMI-optimizing density step) by the end of the simulation. Part of this fall could be due to the loss of bunch electrons previously in focusing phases of the wakefields. Surprisingly, however, Fig. 3.10b) suggests that the impact of the density steps on the bunch charge is rather limited.

Chapter 4

Properties of the self-modulation instability

Self-modulation was initially observed in simulations of long, intense laser pulses propagating in plasma [73, 74]. The resonant excitation mechanism it entails, whereby the envelope of the driver becomes modulated, leads to very high wakefield amplitudes, which can be exploited for acceleration. Though self-modulated laser drivers have meanwhile fallen out of favor[1], the self-modulation instability in long, highly energetic, relativistic particle bunches is currently being explored as an option for plasma-based acceleration.

The onset of an instability can be due either to noise or to a seed, i.e., a signal of higher amplitude than the noise level. When the SMI begins to grow from noise, both the phase of the wakefields along the bunch as well as their amplitude vary randomly from event to event and thus prevent the reliable acceleration of injected particles. In principle, seeding the instability is a means to fix the final phase and amplitude of the wakefields once the process has saturated. Seeded self-modulation was demonstrated by the AWAKE experiment both using a relativistic ionization front (RIF) [63, 77], which is created by an optical laser, and a short electron bunch as the seed [64].

The development of the SMI in a particle bunch carries an important drawback. Although the driver propagates relativistically through the plasma, it has been shown both theoretically [42] and through numerical simulations [78] that the phase velocity of the wakefields sinks below c during the instability's growth. This makes it unworkable to accelerate electrons from the beginning of the plasma, since they can easily slip into defocusing or decelerating phases and be lost. Electrons must therefore be externally injected near or after saturation of the SMI, when the wakefield phase velocity has converged to the driver velocity [42, 78].

In the first part of this chapter, we investigate how the seeded SMI is impacted by noisy initial conditions, where there is a direct connection with the AWAKE experiment and its parameters. In the second part, we delve into more fundamental aspects of the instability, where the goal is to map out its response, or growth, as a function of arbitrary perturbation frequencies.

[1] Note that a recently proposed scheme called "plasma-modulated plasma accelerator" (P-MoPA) [75, 76] aims to generate wakefields resonantly by modulating a long laser pulse in plasma. This modulation technique, however, is based on photon acceleration (i.e., spectral modulation) and dispersive optics, which is entirely different from the self-modulation instability.

4.1 Influence of proton bunch parameters on the saturated SMI

One of the key requirements for high-energy-physics accelerators is reliability. Every machine is subject to fluctuations, but for a mechanism based on the development of an instability, the immediate question is whether reasonable fluctuations of the initial conditions can disable the accelerator. In the case of AWAKE, the characteristics and timing of the driver bunch may vary from shot to shot, which could impact the development of the SMI and the resulting accelerating structure.

It is therefore crucial to ensure the stability of the wakefield amplitude and phase in the presence of input fluctuations. Phase stability is especially critical since the accelerated electrons may otherwise slip into defocusing and decelerating regions of the wakefields and be lost. The transverse component of the wakefields lags the longitudinal component by a fourth of a period, which is a consequence of the Panofsky-Wenzel theorem [79]. This means that the regions of the wakefields which are both accelerating and focusing are only $\lambda_p/4$ long (in the linear regime).

In this section, we will focus on the effects of bunch parameter and plasma radius fluctuations on the amplitude and phase of the wakefields after saturation of the SMI, where acceleration over a long distance can in principle start. We then use test electron calculations to infer the same effects on the energy of the accelerated electrons, and to study the optimal injection conditions that lead to the highest acceleration.

4.1.1 Methodology and simulation parameters

The effects of initial bunch parameter variations are studied through PIC simulations in two-dimensional, axisymmetric cylindrical coordinates. The values of a set of proton bunch parameters are varied independently and the respective simulations are compared to a baseline simulation with parameters similar to those of AWAKE. Note that the hosing instability, which may compete with the seeded SMI, cannot be described in a cylindrical, axisymmetric geometry. We therefore assume here that the self-modulation seed is large enough to prevent the growth of the HI [45] within 10 m of propagation.

In the simulations used for this work, a moving window approximately 33 cm long and 1.6 mm high moves at c, containing a proton bunch (moving at $\sim c$) as the latter propagates through the ten-meter-long plasma. The proton beam has a Lorentz factor $\gamma_b \approx 480$ (corresponding to 450 GeV), an energy spread of 0.035%, and a normalized emittance of 2.5 mm mrad. The RIF seeding is modeled as a sharp rising edge at the center of the proton bunch density profile, which is given by

$$n_b(\zeta, r) = \frac{n_{b0}}{2}\left[1 + \cos\left(\sqrt{\frac{\pi}{2}}\frac{\zeta - \zeta_c}{\sigma_{zb}}\right)\right] e^{-r^2/\sigma_{rb}^2}\,, \tag{4.1}$$

for $\zeta_c - \sqrt{2\pi}\sigma_{zb} \leq \zeta \leq \zeta_s$, where ζ_c is the position of the center of the bunch, ζ_s is the position of the RIF, and σ_{zb} and σ_{rb} are the RMS bunch length and radius, respectively. When the RIF is located at the center of the profile, $\zeta_s = \zeta_c$. The plasma fills the simulation window up to the ionization radius $r_p = 1.5\ \mathrm{mm}$. The remaining simulation parameters can be found in Table A.5, item A.5.1, in Appx. A.

The following physical parameters were used in the simulations: $n_0 = 7\times10^{14}\ \mathrm{cm}^{-3}$, $\sigma_{zb} = 12.6\ \mathrm{cm}$, and $\sigma_{rb} = 283\ \mu\mathrm{m}$. The peak density in Eq. 4.1 is calculated by rearranging the fully integrated bunch profile (which equals the total number of bunch particles N_b), i.e.,

$$n_{b0} = \frac{2N_b}{(2\pi)^{3/2}\,\sigma_{rb}^2\,\sigma_{zb}}\,, \tag{4.2}$$

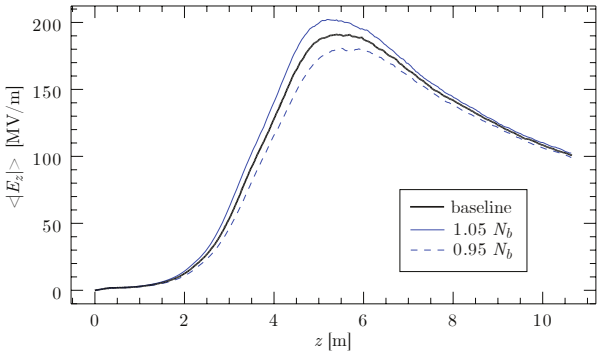

Figure 4.1: Average absolute value of E_z for $r < k_p^{-1}$ as a function of the propagation distance for the baseline simulation and for $\pm 5\%$ variations of the bunch population.

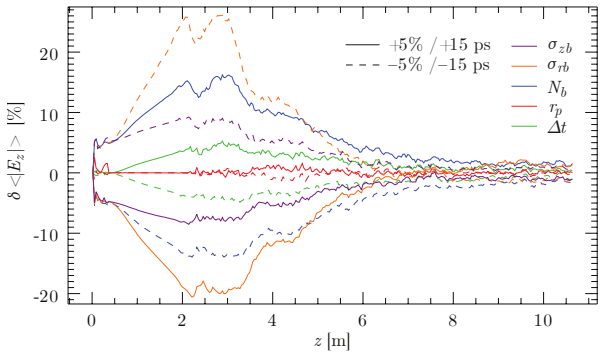

Figure 4.2: Relative deviation of the average absolute value of E_z for all the parameter variations.

giving $n_{b0} \approx 1.89 \times 10^{12}\ \mathrm{cm}^{-3}$ for the proton bunch population $N_b = 1.5 \times 10^{11}$.

Although we have chosen parameters that are representative of the AWAKE experiment, the findings reached here should be general. We have confirmed that this is the case by performing additional simulations with a different set of initial conditions (e.g. double the bunch charge).

The following parameters were independently varied by ±5%: σ_{zb}, σ_{rb}, N_b and r_p. The RMS timing jitter of the proton bunch with respect to the ionizing laser pulse Δt was also varied by ±15 ps. Note that Δt in practice constitutes a shift in the longitudinal bunch profile, thus encompassing either more or less driving charge. Here we will assume that the plasma density and thus the frequency of the wakefields do not vary. The plasma source developed for AWAKE is capable of preserving a constant density along the entire propagation distance to within 0.2% [80]. Larger density variations will be studied in Sec. 4.2.

4.1.2 Effects on the wakefield amplitude

Both the wakefield amplitude and the SMI growth rate depend on the bunch density. The wakefields driven by each self-modulated microbunch can reach an amplitude of the order of $E_z = E_0(n_{b0}/n_0)$ (in the linear regime). Since n_{b0} is given by Eq. 4.2, we expect to observe a general dependence of the wakefield variation according to $E_z \propto N_b/(\sigma_{zb}\sigma_{rb}^2)$.

To quantify this variation, we compare the average absolute value of the longitudinal field component $\langle |E_z| \rangle$ along the propagation distance z for each input parameter variation. The average $\langle \cdot \rangle$ is computed for the entire simulation window up to a radius of one plasma skin depth ($k_p^{-1} \approx 201\ \mu\mathrm{m}$ for $n_0 = 7 \times 10^{14}\ \mathrm{cm}^{-3}$). The resulting data is shown in Fig. 4.1 for the baseline parameters and for variations in the bunch population N_b. In all three cases, the average fields grow rapidly until around $z = 4$ m, after which the self-modulation process saturates and the overall wakefield amplitude gradually decreases. As expected, more (less) bunch charge leads to a higher (lower) field amplitude.

The effects can be better visualized by normalizing the measured amplitude at each z to the baseline case. This relative deviation, defined as $\delta \langle |E_z| \rangle = (\langle |E_z| \rangle - \langle |E_{z,\mathrm{baseline}}| \rangle) / \langle |E_{z,\mathrm{baseline}}| \rangle$, is plotted in Fig. 4.2 for all parameter variations. In general, the effects are maximum during the growth of the SMI ($z < 4$ m), reaching $\delta \langle |E_z| \rangle \approx 26\%$ at $z \approx 2.8$ m for $0.95\ \sigma_{rb}$. However, after saturation of the SMI ($z \gtrsim 6$ m) all cases converge to the baseline amplitude within ±2%.

During the growth phase of the SMI, where linear wakefield theory is still valid ($z \lesssim 4$ m), the trends in Fig. 4.2 are roughly consistent with our expected scaling $E_z \propto N_b/(\sigma_{zb}\sigma_{rb}^2)$: an increase of

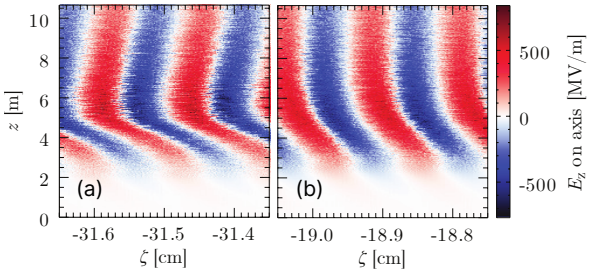

Figure 4.3: Stacked line-outs of E_z on the axis along the propagation distance for two different regions of the wakefields, (a) $\zeta \approx -2.5\ \sigma_{zb}$ and (b) $\zeta \approx -1.5\ \sigma_{zb}$, where ζ is defined with respect to the position of the seed.

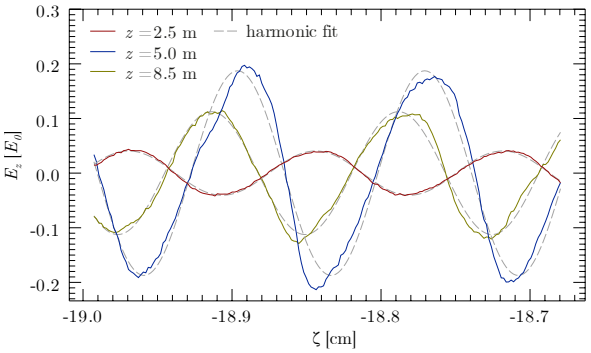

Figure 4.4: Examples of the harmonic fit to a segment of E_z located around $\zeta \approx -1.5\ \sigma_{zb}$ at three different positions along the plasma. The solid lines correspond to the data (smoothed) and the dashed lines to the fits.

N_b by 5% produces higher values for $\langle |E_z| \rangle$, for example, and the variations in σ_{zb} and σ_{rb} cause inversely proportional effects, with the σ_{rb} parameter variations causing the largest effects. There is also a distinct effect on the growth rate, as evinced by the different slopes up to $z = 3$ m in Fig. 4.2.

Since the timing jitter Δt is small when compared to the bunch duration we expect its main effect to be associated with an increase or decrease in total charge driving the wakefields (corresponding to $N_b \pm 2.85\%$). Finally, a $r_p \pm 5\%$ variation seems to have no significant effect on the wakefield amplitude, at least for our choice of the baseline plasma radius. A smaller plasma radius can enhance the wakefield's focusing force and hence the SMI's growth rate by hindering the plasma's shielding response to the charge in the drive bunch [81]. However, this effect only becomes prominent when r_p approaches σ_{rb}, which, despite the variations of ±5%, is not the case here.

4.1.3 Effects on the wakefield phase

We now turn our attention to the behavior of the wakefield phase. Both numerical and theoretical work has shown that, during the growth of the SMI, the phase velocity of the wakefields varies along the plasma and along the bunch, eventually converging towards the driver velocity after saturation [42, 78]. This is exemplified in Fig. 4.3, where the on-axis line-outs of the longitudinal wakefields for each z are stacked and represented in a color scale. Since the simulation window moves at c, a negative slope in this graph means that the phase velocity of the wakefields is subluminal, while a positive slope indicates that it is superluminal. The relativistic proton bunch moves at approximately the speed of light, so its velocity would correspond to a vertical line in Fig. 4.3 (more precisely, $\Delta z/\Delta\zeta \approx -2\,\gamma^2$ for bunch particles).

As demonstrated in Fig. 4.3, the wakefields are slower than c during the growth of the SMI, i.e., for $z < 4$ m (see negative slope). After saturation, however, the wakefield velocity behaves differently for different regions along the bunch. Far behind the RIF [around $-2.5\ \sigma_{zb}$, Fig. 4.3(a)] the phase velocity is superluminal for $z > 5$ m, while around $\zeta \approx -\sigma_{zb}$ it is subluminal (not shown). The ideal region to inject witness electrons would therefore be around $1.5\ \sigma_{zb}$ or 18.9 cm behind the RIF [see Fig. 4.3(b)] in this case. Experimentally, the injection position along the bunch can be scanned so as to find the optimal ζ position for maximum electron acceleration.

The effects of the parameter variations on the wakefield phase are studied quantitatively by fitting the function $f(\zeta) = A\ \sin[k_p\,(\zeta - \zeta_s) + \phi]$ (expected for linear wakefields) to 2.5-λ_p-long

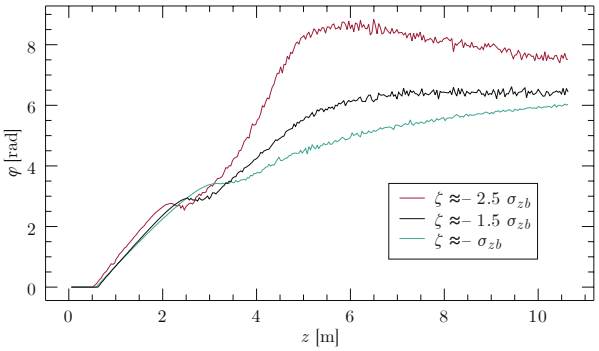

Figure 4.5: Wakefield phase shift along the propagation distance, at three different locations along the proton bunch.

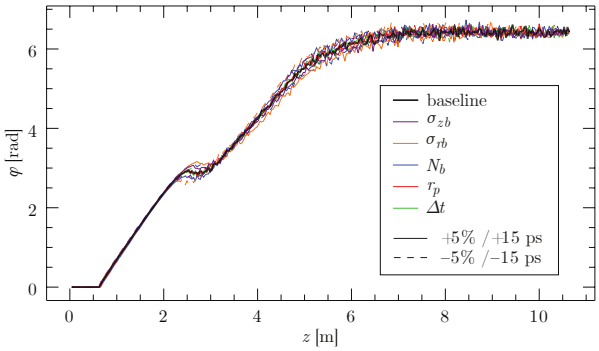

Figure 4.6: Wakefield phase shift along the propagation distance for all parameter variations, at $\zeta \approx -1.5\ \sigma_{zb}$.

segments (starting at ζ_s) of E_z on axis (see Fig. 4.3), where A and ϕ are the fitting parameters. The value of ϕ is always relative to the seed position ζ_s.

As an example, the fit to a segment located around $\zeta \approx -1.5\ \sigma_{zb}$ is shown in Fig. 4.4 for three different propagation distances. The fit is worst around the saturation point of the SMI (see curves for $z = 5$ m), where the fields show signs of nonlinearity (wave steepening). However, the purpose of the fit is to define a local phase shift with respect to ζ_s, which is accomplished if the phases of both curves match, as is the case.

The result of this analysis is shown in Fig. 4.5 for three different positions along the bunch. Note that the burgundy and black curves correspond to the same locations as in Fig. 4.3. Figure 4.5 again suggests that the region around $1.5\ \sigma_{zb}$ behind the RIF is particularly suitable for electron injection, since the phase velocity (and ϕ) remains stable after saturation and is approximately c.

The position $\zeta \approx -1.5\ \sigma_{zb}$ was chosen for the comparison of the effects from the parameter fluctuations, shown in Fig. 4.6. We may estimate a theoretical scaling for the phase shift using an asymptotic model for the SMI, which is valid for $k_p|\zeta| \gg k_\beta z$ (long-bunch, early-time regime; see Eq. 2.118 on p. 34). The longitudinal wakefield component then behaves as $E_z \propto \cos\left[k_p\ \zeta - \frac{\pi}{4} + \varphi(\zeta, z)\right]$, with the phase shift $\varphi(\zeta, z) \propto n_{b0}^{1/3}$ [42]. The condition above is fulfilled for $\zeta \approx -1.5\ \sigma_{zb}$ and $z \sim 10$ m, with $k_p|\zeta| \approx 940.4$ and $k_\beta z \approx 1.9$. Nevertheless, the phase shift in Fig. 4.6 only displays a relationship of the form $\phi \propto N_b^{1/3} / \left(\sigma_{zb}\sigma_{rb}^2\right)^{1/3}$ (where we used Eq. 4.2) roughly between $z = 3.5$–5 m.

The largest effects on the wakefield phase are again observed before the saturation of the SMI, at $z = 2$–3 m (see Fig. 4.6). Here, the largest difference is of roughly $2\pi/20$ for $0.95\ \sigma_{rb}$ at $z \approx 2.5$ m. After this point, phase variations are limited to ±0.4 rad (corresponding to approximately $\lambda_p/16$), an estimate constrained by simulation noise. Moreover, the phase becomes constant after $z \approx 6$ m in all cases, which is also the point after which the wakefield amplitude becomes essentially independent of the input parameter variations (see Fig. 4.2).

4.1.4 Behavior of accelerated electrons

The characteristics of the accelerated electron bunch are the most important experimental output in the AWAKE experiment, and they are non-trivially dependent on several factors besides the wakefields themselves, such as the electrons' initial velocity or the injection point along the plasma. Consequently, the wakefield effects reported above are not sufficient to infer possible effects on the accelerated bunches.

To estimate the effects of input fluctuations on accelerated electrons, we devise a simple, one-dimensional diagnostic where the transverse dynamics of the problem are put aside, but

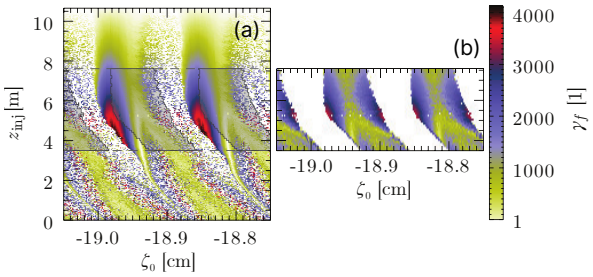

Figure 4.7: Final energy of on-axis test electrons at $z = 10$ m as a function of their injection point and initial position along the bunch, as obtained from (a) the 1D pusher and (b) a PIC simulation (peak value, for electrons initially at $r < 0.5\ k_p^{-1}$). White areas correspond to lost electrons. The shaded areas in (a) correspond to the data in (b).

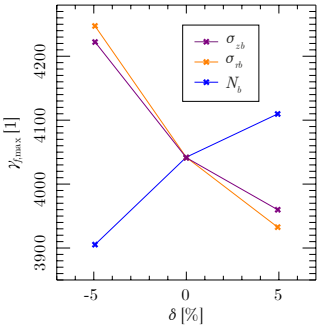

Figure 4.8: Maximum final energy found through the 1D diagnostic of Fig. 4.7(a) for three different parameter variations ($\delta = 0$ corresponds to the baseline parameters).

where dephasing is contemplated. This diagnostic essentially assumes that the electrons stay on the axis at all times, feeling zero transverse forces. Since E_z peaks on the axis and decays radially, an electron performing any transverse motion about the axis is subject to weaker longitudinal forces than if it is propagating exclusively along it (the most effective trajectory in terms of energy gain). This approach thus provides a best-case scenario for the energy gained by accelerated electrons.

Using the on-axis accelerating wakefield E_z obtained in the simulations, we place test particles all along ζ and at every available propagation distance, and calculate their one-dimensional evolution up to $z = 10$ m with a particle-pushing Boris algorithm. The output is the energy gain acquired by an electron (γ_f) as a function of its injection point along the plasma ($z_{\rm inj}$) and its initial position along the bunch (ζ_0). The initial energy of the test electrons is $\gamma_0 = 39.1$, or approximately 20 MeV, which is the maximum range of the electron injector commissioned for AWAKE Run 1 [18]. The spatial resolution of these results is limited to the resolution of the simulation box in the ζ direction (which in this case means that at most 38 evenly-spaced test electrons can be tracked for every $\lambda_p/2$), while the temporal resolution is limited to the number of simulation file dumps (in this case 300 over the entire propagation, giving a maximum resolution for $z_{\rm inj}$ of 3.55 cm).

The result is shown in Fig. 4.7(a) for the baseline simulation. Note that the white pixels correspond to test electrons that lose enough energy at some point along z so as to slip out of the 33-centimeter-long simulation window, and hence do not reach the end of the plasma. The general features of the accelerating field [see Fig. 4.3(b)] are visible in the point density of Fig. 4.7(a). Regions with few test electrons correspond to decelerating regions. In regions where the field is accelerating ($E_z < 0$, for example $-19.00 < \zeta_0\ [\rm cm] < -18.95$), all the test electrons reach the end of the plasma. As expected, the final energies decrease as electrons are injected later along z (shorter acceleration distances), though this is also because the wakefield amplitude decreases after $z \approx 5$ m (see Fig. 4.1). Figure 4.7(a) also implies that some electrons injected in the decelerating phase of the wakefields survive energy loss and dephasing to ultimately reach large energies, including for $z_{\rm inj} < 4$ m (see scattered red pixels).

The comparison between different parameter fluctuations was performed by selecting the maximum final energy ($\gamma_{f,\max}$) attained in the same wakefield period for each different case. The chosen range is $-18.990 \leq \zeta_0\ [\rm cm] \leq -18.956$ (approximately $\lambda_p/4$ long). Figure 4.8 shows $\gamma_{f,\max}$ as a function of the variation amplitude δ for the parameters that caused the largest effects, i.e.,

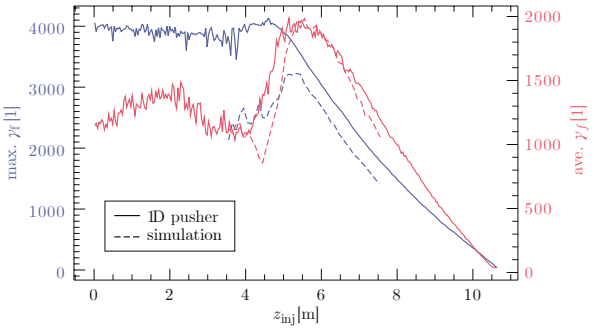

Figure 4.9: Maximum (blue) and average (red) final energies for the region shown in Fig. 4.7 according to the 1D diagnostic (solid lines) and a PIC simulation with test electrons (dashed lines).

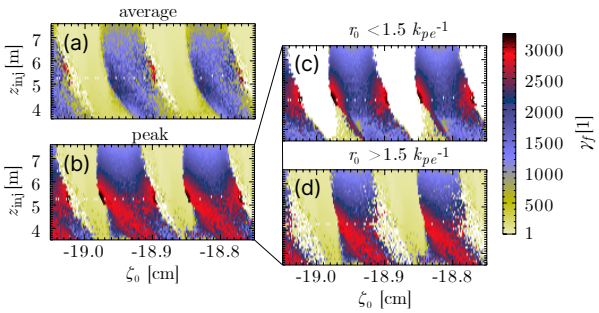

Figure 4.10: Radially averaged (a) and peak (b–d) final energies of injected electrons as a function of their initial position ζ_0 and injection point $z_{\rm inj}$, obtained from the PIC simulation. The peak energies are shown for (b) all r_0, (c) $r_0 < 1.5\ k_{pe}^{-1}$, and (d) $r_0 > 1.5\ k_{pe}^{-1}$.

σ_{zb}, σ_{rb} and N_b. We find trends consistent with $\gamma_{f,\max} \propto N_b/(\sigma_{zb}\sigma_{rb}^2)$, which is justifiable by the fact that the energy gain by trailing particles directly depends on the amplitude of E_z. The resulting maximum final energies vary at most between roughly -3% and +5% (the corresponding injection points lie between 4.15 m and 4.52 m along the plasma).

To validate the diagnostic described above, we performed a further baseline simulation in which test electrons are injected at 41 equally spaced injection points between 3.5 and 7.6 m (see Table A.5, item A.5.2, in Appx. A). These test electrons have zero emittance and are initially uniformly distributed in space (both longitudinally and radially). The resulting data is represented in Fig. 4.7(b) for electrons injected close to the axis ($r_0 < 0.5\ k_p^{-1}$) that reached the end of the plasma. We naturally observe the influence of the transverse wakefields and dynamics in Fig. 4.7(b) in the form of clear-cut regions where all test electrons were lost. The periodic regions with the most surviving electrons in both figures [i.e. accelerating phases in Fig. 4.7(a) and focusing phases in Fig. 4.7(b)] are roughly phase-shifted by around $\lambda_p/4$ [note the shaded superposition of the simulation data in Fig. 4.7(a)], as would be expected from the Panofsky-Wenzel theorem [79]. Otherwise, there is reasonable agreement between both datasets.

A more quantitative comparison between the 1D diagnostic and the simulation results is displayed in Fig. 4.9, consisting of the average (red curves) and maximum (blue curves) values of γ_f within the ζ_0 region contemplated in Fig. 4.7. The peak energies in the 2D simulation results are generally lower than the 1D results (compare dashed and solid blue curves in Fig. 4.9), as expected, since the 1D diagnostic represents a best-case scenario, but both curves follow a very similar evolution after saturation ($z \gtrsim 5$ m). Disagreeing trends are expectable for $z_{\rm inj} < 5.5$ m, which is the region where we expect the most variation of the wakefield phase and therefore particle defocusing. The average energies in turn show very good agreement along the entire $z_{\rm inj}$ region probed (see red curves).

The peak final energies obtained from the simulation with test electrons (see dashed blue curve in Fig. 4.9) suggest an optimum injection point between 5–6 m. Since this data only includes electrons injected close to the axis ($r_0 < 0.5\ k_p^{-1}$), we might wonder whether a different optimal injection point applies to other initial radii. Figure 4.10 offers a more complete picture of the final energy distribution measured in the simulation. Whether we consider the average [Fig. 4.10(a)] or peak [Fig. 4.10(b)] value of the energies attained for each ζ_0, the highest energy gain is met for $z_{\rm inj} = 5 - 6$ m.

Figure 4.10(b) furthermore indicates that some electrons reach high energies despite being

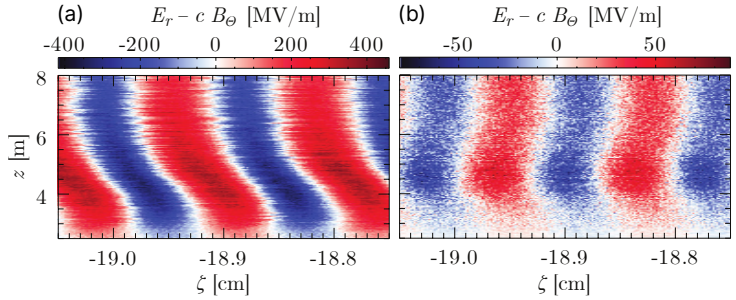

Figure 4.11: Stacked line-outs of the transverse wakefield component, taken at (a) $r = k_{pe}^{-1}$ and (b) $r = 3\,k_{pe}^{-1}$.

injected before saturation of the SMI ($z_{\mathrm{inj}} < 5$ m), as previously suggested by the simple 1D diagnostic results. By separating the analysis of the peak final energies from the simulation into two radial regions above and below $r = 1.5\,k_p^{-1} \approx 0.3$ m, we find that it is the electrons further away from the axis that reach the highest energies when injected before saturation [compare Fig. 4.10(c) and (d)].

This difference is due to the fact that the phase velocity of the wakefields varies along r as well as along ζ and z. This is demonstrated in Fig. 4.11, which depicts stacked line-outs of the transverse wakefield component $E_r - c\,B_\theta$ (responsible for focusing and defocusing) at two different radial positions. For $z < 6$ m, for example, the phase velocity closer to the axis [see Fig. 4.11(a), at $r = k_p^{-1}$] behaves as expected during the growth of the SMI and as previously discussed in Fig. 4.3. At a larger radius, however, the phase is approximately stable between 4–5.5 m [see Fig. 4.11(b), at $r = 3\,k_p^{-1}$]. This would explain why electrons starting before $z = 5$ m at smaller radii tend to be lost (as they slip into defocusing half-periods due to the rapidly changing wakefield phase), while electrons further away from the axis may fall into a stable wakefield phase and benefit from the accelerating fields over a larger distance.

In general, the optimal injection point along the plasma will be determined by the start of the saturation of the SMI, which takes place earlier with either larger n_0 or N_b. The position with the most stable phase along the bunch can also be scanned for different parameters, and it tends to be closer to the seed point for higher n_0 and smaller N_b. The increase of either of these two parameters will further lead to higher wakefield amplitudes, and hence to larger energy gains by trailing electrons.

4.1.5 Comparison to subsequent experimental results

The purpose of the work above was to study the potential of the AWAKE experiment to be successful in its stated goal of electron acceleration. For the parameter variations we considered (±5% and ±15 ps), we found that the wakefield properties converge to similar values after saturation of the SMI, within a few percents for the amplitude and the equivalent of less than $\lambda_p/8$ (12.5% of a period) for the phase. Based on simulations, we also found that the optimal injection coordinates for our parameters ($n_0 = 7 \times 10^{14}$ cm^{-3} and $N_b = 1.5 \times 10^{11}$) are 5–6 m into the plasma and around $1.5\,\sigma_{zb}$ behind the RIF. For injections in this range, electrons close to the axis can reach energies of the order of 1.5 GeV over the last 4–5 m of plasma. Comparable final energies are also attained when injection takes place before saturation ($z < 5$ m), but by electrons far from the axis instead.

Several experimental results have been published by the AWAKE Collaboration after the completion of this work, which we can briefly compare to the findings above. The experiment has for example demonstrated the acceleration of electrons up to 2 GeV [20]. In particular, a final energy

of approximately 1.5 GeV was attained with a constant plasma density of $n_0 = 6.6 \times 10^{14}\ \mathrm{cm}^{-3}$ and where the electrons were located around σ_{zb} behind the ionizing laser pulse, which is generally consistent with the peak energy observed in our witness electron simulation (see Fig. 4.9). Note that the electron beam was injected at an angle in the experiment, its trajectory crossing the proton beam's at around $z = 2\ \mathrm{m}$. Due to the electron beam's emittance and waist location at the plasma entrance, the injected electrons were effectively sprayed over a range in ζ and z, which makes it difficult to compare the injection coordinates directly.

The phase stability of seeded self-modulation has also been studied using experimental data [63]. This analysis of streak camera images of the proton bunch after 10 m found an RMS variation of up to 7% of a period, though this result is limited by several uncertainties in the input parameters and the measurements. Notwithstanding, the experimental finding is in agreement with our post-saturation maximum phase variation of ±0.4 rad, or ±6.4% of a period.

4.2 Detuning effects on the SMI

In Ch. 3, we explored the evolution of the hosing instability as to how it reacts to mismatches between the instability's resonant frequency and a seed frequency in a particle bunch, and we painted a much richer picture of the instability's physics than the one prevailing. At this point, it behooves us to notice, once again, that the self-modulation instability and the HI are closely related, in both mathematical and physical terms. It is therefore worth investigating whether, by applying an analogous approach to the one in Ch. 3, we may discover new properties of the SMI.

Besides this, it is known that a density gradient effectively delays or hastens the growth of the SMI, though this effect has been discussed in the context of asymptotic models that assume small gradients [82], or of the saturation phase of the SMI [83, 84]. We thus have every indication that frequency detuning (via the plasma density) may play an important role in the SMI.

4.2.1 Adiabatic dispersion relation

We once again follow a relatively established prescription to obtain a dispersion relation for the SMI in long particle bunches. In this case, where the equations describe the evolution of the RMS bunch radius, we must make a stricter set of approximations to arrive at a starting point where the mathematical methods become tractable.

As such, we consider a bunch with a transverse flat-top profile, where r_b is the radial edge of the bunch, and assume a small perturbation r_1 around an equilibrium radius r_0, i.e., $r_b = r_0 + r_1$ with $r_1/r_0 \ll 1$. This approximation yields a differential equation for the radius perturbation, which is simplified further in the long-bunch adiabatic regime, i.e., assuming $f(\zeta) \approx 1$ and $\partial_\zeta f(\zeta) \to 0$ for the longitudinal profile $f(\zeta)$. A dispersion relation for the growing modulation of r_1 can be obtained from the resulting partial differential equation, Eq. 2.110:

$$\begin{aligned} \left(\partial_\zeta^2 + 1\right)\left(\partial_z^2 + 4\,\kappa^2 \hat{k}_\beta^2\right) r_1(\zeta, z) = 2\,\nu \hat{k}_\beta^2\, r_1(\zeta, z) \quad \Leftrightarrow \\ \left(\partial_{\zeta_*}^2 + k_p^2\right)\left(\partial_{z_*}^2 + 4\,\kappa^2 k_\beta^2\right) r_1 = 2\,\nu k_\beta^2\, k_p^2\, r_1\ , \end{aligned} \tag{4.3}$$

where the asterisk subscript indicates a variable that is not normalized. Let us recall that the constants κ^2 and ν depend exclusively on the equilibrium radius r_0 and are defined as (see p. 32)

$$\kappa^2 = 2\,K_1(r_0)\,\left[\frac{I_2(r_0)}{r_0} + I_3(r_0)\right]$$

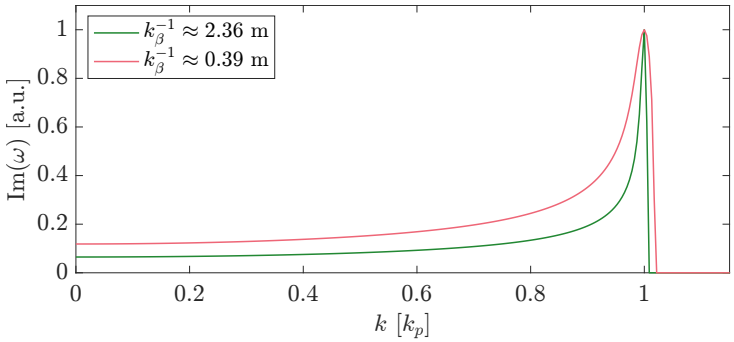

Figure 4.12: SMI growth rate as a function of the wavenumber for two different betatron periods, according to the dispersion relation Eq. 4.5.

$$\nu = 4\, I_2(r_0) K_2(r_0)\ .$$

In addition, please note that Eq. 2.110 can be interpreted as a coupling between two radius perturbations, similarly to the HI: one associated with the plasma density perturbation, $r_{\psi 1}$, and another with the particle bunch, r_1:

$$\left(\partial_z^2 + 4\,\kappa^2 \hat{k}_\beta^2\right) r_1 = 2\,\nu \hat{k}_\beta^2\, r_{\psi 1}(\zeta, z)$$
$$\left(\partial_\zeta^2 + 1\right) r_{\psi 1} = r_1\ .$$

The derivatives in the unnormalized, co-moving variables (z_*, ζ_*) in Eq. 4.3 can be replaced with laboratory frame coordinates (z', t) using the chain rule of differentiation (see Eqs. 3.3–3.4 on p. 42):

$$\left(\partial_t^2 + \omega_p^2\right)\left(\frac{1}{c^2}\partial_t^2 + \frac{2}{c}\,\partial_t \partial_{z'} + \partial_{z'}^2 + 4\,\kappa^2 k_\beta^2\right) r_1 = 2\,\nu k_\beta^2\,\omega_p^2\, y_c\ . \tag{4.4}$$

As shown in Sec. 3.1, we obtain a dispersion relation after replacing plane wave solutions $r_1 \propto \exp[i(kz' - \omega t)]$ into Eq. 4.4 and after some rearrangement:

$$\left(\hat{\omega}^2 - 1\right)\left(\hat{\omega} - \hat{k}\right)^2 - 4\,\kappa^2 \hat{k}_\beta^2\,\hat{\omega}^2 = 2\,\hat{k}_\beta^2(\nu - 2\kappa^2)\ , \tag{4.5}$$

where $\hat{\omega} = \omega/\omega_p$ and $\hat{k} = k/k_p$ are the normalized angular frequency and wavenumber, respectively.

Once again, note that we recover the laboratory frame dispersion relation for the SMI in laser pulses with different constant parameters [68]. In this case, the general parameters defined in Ref. [68] correspond to $\Gamma_1 = 4\,k_\beta^2\kappa^2$, $\Gamma_2 = 2\,k_\beta^2\nu$ and $\Gamma_3 = 1$.

By solving Eq. 4.5 for $\hat{\omega}$ and taking its imaginary part, we obtain the adiabatic growth rate for the SMI, shown in Fig. 4.12 for two different betatron periods. These two values for k_β^{-1} result from the choice of a proton bunch ($M_b/m_e = 1836.153$, green) and a bunch of artificially light, positive particles ($M_b/m_e = 50$, red) with the following parameters: $n_{b0}/n_0 \approx 0.0397$, $\gamma = 427$, and $r_{b0} \approx 0.53\ k_p^{-1}$. Similarly to the HI, the curves in Fig. 4.12 peak at $k = k_p$ and feature a tail for wavelengths longer than λ_p. A crucial difference, however, is that this tail does not become zero at infinite wavelengths ($k = 0$) for the SMI. This finite growth rate in the absence of a seed perturbation is fully consistent with the properties of the SMI, which eventually develops in a long bunch or laser pulse propagating in plasma, with or without seed.

Once again, note that the approach taken above does not accommodate any spatiotemporal effects, due to the assumption of a plane wave perturbation. In the following section, we apply the same methodology as in Sec. 3.2 to unveil a fuller picture of the SMI's growth dynamics.

4.2.2 Dynamic amplitude response

In Sec. 3.2 we argued that the hosing instability can be seen as a harmonic oscillator whose properties vary in time. The same can be shown for the SMI, but only in the approximation of a small perturbation of the slowly evolving bunch radius r_b (for a flat-top transverse profile). This is due to the highly nonlinear evolution of r_b, dictated by the envelope equation (see Eqs. 2.84 and 2.85).

Equation 2.110 describes the evolution of the radius perturbation r_1 for a bunch with a longitudinal profile $f(\zeta)$ and a flat-top transverse profile (and where the second branch of the right-hand side in Eqs. 2.84–2.85, for $r_1(\zeta) < r_1(\zeta')$, is neglected). Written as a parametric oscillator, we obtain the equation:

$$\left(\frac{d^2}{dz^2} + k_{\mathrm{HO}}^2(\zeta, z)\right) r_1(\zeta, z) = F(\zeta, z, r_1) \,, \tag{4.6}$$

where $k_{\mathrm{HO}}^2(\zeta, z)$ and $F(\zeta, z, r_1)$ are given by

$$k_{\mathrm{HO}}^2(\zeta, z) = -4\,\kappa^2 \hat{k}_\beta^2 \int_\zeta^\infty d\zeta' \sin(\zeta - \zeta') f(\zeta') \,, \tag{4.7}$$

$$F(\zeta, z, r_1) = -2\,\nu \hat{k}_\beta^2 \int_\zeta^\infty d\zeta' \sin(\zeta - \zeta') f(\zeta')\, r_1(\zeta', z) \,. \tag{4.8}$$

Since the misleadingly simple structure of Eq. 4.6 conceals a variety of interesting transient effects from the interaction of the driving frequency and the oscillation amplitude, we once again explore the amplitude response of a self-modulating radius perturbation to a seed frequency. We will also see that disregarding the second branch (i.e., for $r_b(\zeta) < r_b(\zeta')$) of the right-hand side $\left[F(\zeta, z, r_1) - r_1(\zeta, z)\, k_{\mathrm{HO}}^2(\zeta, z)\right]$ has important consequences.

In this analysis of the properties of the SMI we will consider a positive-charge particle beam with $\gamma_b = 427$, an RMS length $\sigma_z = 12\,\mathrm{cm}$, an RMS radius $\sigma_r = 200\,\mu\mathrm{m}$, a beam population $N_b = 3 \cdot 10^{11}$, and a cosine-shaped longitudinal profile (see Eq. 3.18 on p. 45). The mass of the beam particles is artificially defined as $m_b = 50\, m_e$, such that the normalized betatron skin depth of the beam is $\hat{k}_\beta^{-1} \approx 1500$. This value is large enough to separate the time scales of self-focusing (or beam pinching) [85] and of the growth of the SMI, such that we can study the SMI before beam pinching dominates, yet low enough to save some computational time in the PIC simulations. The plasma density is $n_0 = 2 \cdot 10^{14}\ \mathrm{cm}^{-3}$, and the window considered for the analysis is $L = 280\ k_p^{-1}$ long ($\sim 44\ \lambda_p$), with the front edge of the beam located at $\zeta_s = 275\ k_p^{-1}$.

The theory available to describe the SMI assumes a flat-top transverse profile where r_0 is in equilibrium. In the PIC simulations, however, this is not the case since the bunch profile varies longitudinally and hence there is a different equilibrium condition at every ζ. Furthermore, since a transversely flat bunch was observed to pinch much faster than one with a Gaussian transverse profile, the latter was chosen to extend the time scale of self-focusing as much as possible. This bunch profile corresponds to a peak beam density $n_{b0}/n_0 \approx 0.02$. For the same amount of bunch charge, the theoretical, flat-top transverse profile corresponds to a peak beam density $n_{b0}/n_0 \approx 0.04$. The normalized emittance of the beam in the simulations is $\varepsilon_N = 3.5\,\mathrm{mm\,mrad}$, which is the nominal value for the proton bunch driver in the AWAKE experiment. Lastly, the initial radius perturbation is defined as $r_{10}(\zeta) = \delta_r\, r_0 \sin[k(\zeta - \zeta_s)]$, with a relative amplitude $\delta_r = 0.1$.

How the amplitude response is measured

Following the same principle as in Sec. 3.2, we measure the amplitude response by defining a ratio between the radius perturbation after a propagation distance z and the initial radius perturbation r_{10}, which has a well-defined frequency, i.e., $r_{10} \propto \sin(k\zeta)$. Since these quantities vary along the bunch (along ζ), we eliminate this dependence by integrating the absolute value of both along ζ. The resulting amplitude response therefore provides information about the entire section of the beam we are considering (with length L), and evolves along the propagation distance:

$$\Pi(k, z) = \frac{\int_L |r_1(z, \zeta)|\, d\zeta}{\int_L |r_{10}(\zeta, k)|\, d\zeta} \,. \tag{4.9}$$

The theoretical evolution for r_1 is found by considering the initial plasma response to the perturbation r_{10} and its effect on the radius perturbation, or, in other words, by applying the power series model (see Sec. 2.4) up to $n = 2$:

$$r_1(z, \zeta) = r_{10}(\zeta) + \mathcal{R}\{r_{10}\}\, \tfrac{1}{2}\, z^2 \,. \tag{4.10}$$

We introduce $\mathcal{R}\{r_1\}$ to symbolize the right-hand side of the differential equation for r_1 (see for example Eq. 2.109), which can be expressed more generally as

$$\frac{d^2 r_1}{dz^2} = \mathcal{R}\{r_1\} \,. \tag{4.11}$$

If we choose to neglect the branch $r_b(\zeta) > r_b(\zeta')$ of the envelope equation for a flat-top transverse profile (Eqs. 2.84–2.85 on p. 26), $\mathcal{R}$ is given by

$$\mathcal{R}\{r_1\} = -2\, \hat{k}_\beta^2 \int_\zeta^\infty d\zeta'\, \sin(\zeta - \zeta')\, f(\zeta') \left[\nu\, r_1(\zeta') - 2\, \kappa^2\, r_1(\zeta)\right] \,, \tag{4.12}$$

which corresponds to Eq. 2.109 rewritten with the constants ν and κ^2.

Otherwise, we can apply the same linearization procedure that led to the result above (described in pp. 30–32) to the complete envelope equation and arrive at

$$\mathcal{R}\{r_1\} = -2\, \hat{k}_\beta^2 \int_\zeta^\infty d\zeta'\, \sin(\zeta - \zeta')\, f(\zeta') \begin{cases} \left[2\, \kappa_<^2\, r_1(\zeta) - \nu\, r_1(\zeta')\right] & r_1(\zeta) \le r_1(\zeta') \\ \left[2\, \kappa_>^2\, r_1(\zeta) + \nu\, r_1(\zeta')\right] & r_1(\zeta) > r_1(\zeta') \end{cases} \,, \tag{4.13}$$

where $\kappa_<^2 = \kappa^2 = 2\, K_1(r_0)\, \left[\frac{I_2(r_0)}{r_0} + I_3(r_0)\right]$, $\kappa_>^2 = 2\, I_1(r_0)\, \left[\frac{K_2(r_0)}{r_0} + K_3(r_0)\right]$, and where we used the identity $I_1(r)K_2(r) + I_2(r)K_1(r) = 1/r$ [52, Eq. 10.28.2]. We will contemplate both versions of $\mathcal{R}$ in the following.

We will likewise seek to validate the theoretical result by comparing it to simulation data. Here we can exploit the axisymmetry implied in the SMI theory and carry out PIC simulations in 2D (axisymmetric) cylindrical geometry. A direct comparison, however, is not straightforward. In a real particle bunch, there is the slow, added effect of self-focusing [85]. In our theoretical model the radius perturbation r_1 is supposed to evolve on top of a constant bunch radius[2], which should therefore find itself in equilibrium, or matched, with the plasma.

A simple matching condition for r_0 can be found in the long-bunch adiabatic regime ($f(\zeta) \approx 1$ and $\partial_\zeta f \to 0$) by setting $dr_0/dz = 0$ in the envelope equation for r_0 (see Eq. 2.105 on p. 31) and

[2] Allowing r_0 to evolve would result in a system of two coupled differential equations for r_0 and r_1, which is significantly more difficult to solve.

assuming a slowly evolving r_0, i.e., $\partial_\zeta r_0 \to 0$. Under these assumptions, Eq. 2.105 reduces to the matching condition

$$\varepsilon^2 = 8\,\hat{k}_\beta^2\, r_0^3\, K_1(r_0)\, I_2(r_0)\ . \tag{4.14}$$

(Note that the intermediate steps for this derivation are justified in Eqs. 2.106–2.107 and Eq. 2.88.) However, simulating the cosinusoidal longitudinal profile mentioned above (see second paragraph after Eq. 4.8) means that the long-bunch adiabatic assumption and thus the matching condition in Eq. 4.14 are no longer strictly met. For a non-constant profile $f(\zeta)$ the actual matching condition is a function of ζ and would be given by a complicated expression. The particle bunch in the 2D cylindrical simulations is therefore unmatched and has a Gaussian transverse shape, for which the time scale for self-focusing is longer than for a flat top. Note that, in the comparison between theory and simulations, we guarantee that the RMS radial size is the same for both transverse profiles, i.e, $r_b = \sqrt{2}\,\sigma_r$ (see Table A.6, items A.6.1 and A.6.4, in Appx. A for the full simulation details).

Our theoretical model describes exclusively the radius perturbation r_1, so we must extract this quantity from the simulation data in order to perform a comparison. This is achieved by subtracting the slowly evolving (or adiabatic) component of the bunch radius $\sigma_{r,\mathrm{adiab}}(\zeta, z)$, which is obtained from a simulation with no SMI seed (see Fig. 4.13, top). Figure 4.13 (bottom) exemplifies the resulting radius perturbation, taken at $z \approx 2\,k_\beta^{-1}$ from a simulation seeded at $0.8\,k_p$. This definition of the radius perturbation is valid until the bunch in the unseeded simulation begins to self-modulate from noise, which introduces a fluctuation at k_p to $\sigma_{r,\mathrm{adiab}}$. The simulation data discussed below is taken long before this point is reached. The amplitude response for the 2D cylindrical simulations is therefore defined as

$$\Pi(k, z) = \frac{\int d\zeta\ |\sigma_{r,k}(\zeta, z) - \sigma_{r,\mathrm{adiab}}(\zeta, z)|}{\int d\zeta |\sigma_{r,k}(\zeta, 0) - \sigma_{r,\mathrm{adiab}}(\zeta, 0)|}\ . \tag{4.15}$$

The SMI amplitude response and subharmonic resonance according to theory

The theoretical amplitude response for the SMI along the propagation distance, given by Eqs. 4.9–4.13, is depicted in Fig. 4.14. As expected, both versions of the theory indicate that the growth of the SMI is maximized for $k = k_p$, although the two solutions exhibit different time scales [note the differing z-axes between Fig. 4.14(a-b) and Fig. 4.14(c-d)]. It is not yet clear why this difference comes about.

The early line-outs in Figs. 4.14b) and d) display a consistent shape around $k = k_p$ (see red and

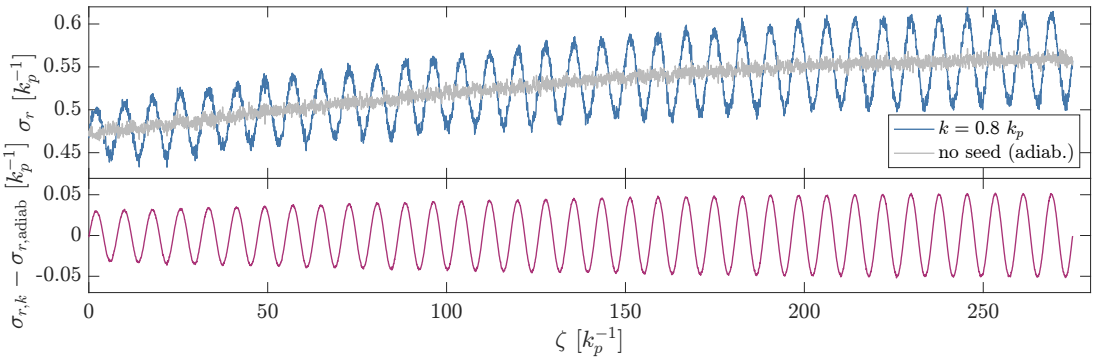

Figure 4.13: Example of the measurement of the RMS radius perturbation from PIC simulations, taken at $z \approx 2\,k_\beta^{-1}$. Top: bunch radius along ζ in two simulations, one where the SMI is seeded at $k = 0.8\,k_p$ (blue) and one without a seed (grey). Bottom: bunch radius perturbation obtained from the subtraction of the grey curve from the blue curve in the top plot.

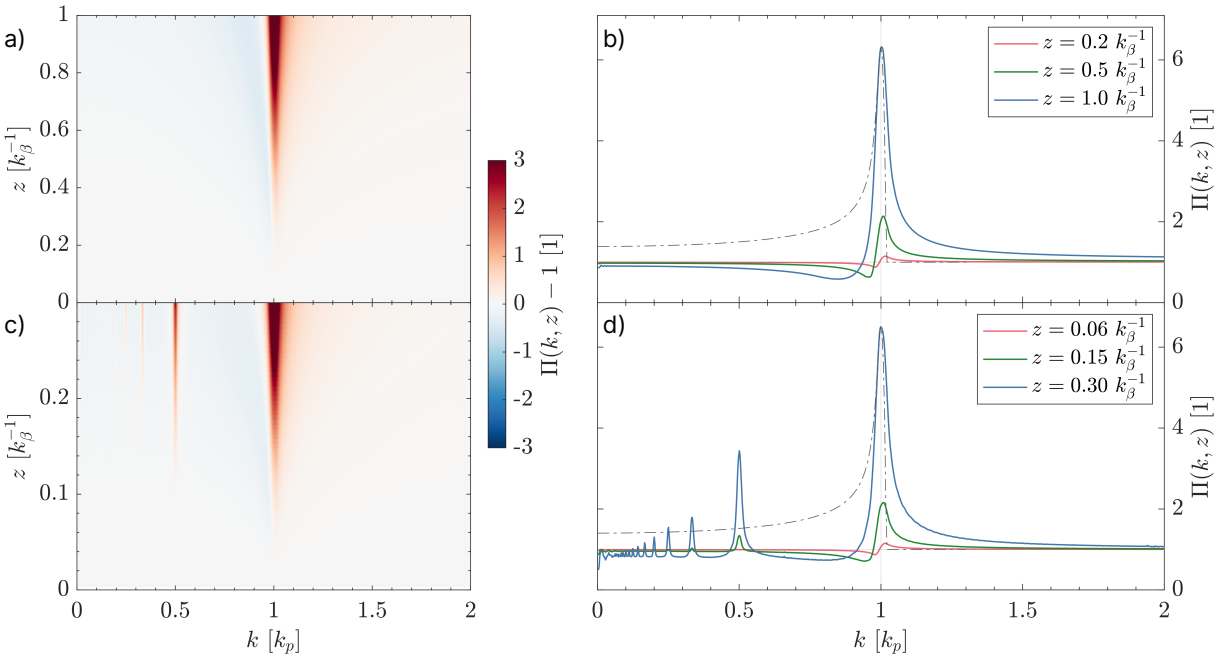

Figure 4.14: SMI amplitude response as a function of seed wavenumber and propagation distance according to two versions of the theory: Eq. 4.12 (a-b) and Eq. 4.13 (c-d), replaced in Eq. 4.10. The evolution along time is shown in a) and c), with line-outs taken at different propagation distances in b) and d). Note that the scale of the z-axis is different for the top and bottom rows. The normalized outline of the amplitude response corresponding to the dispersion relation Eq. 4.5 has been included in b) and d) as a grey dash-dotted curve. Note that the color scale in a) and c) is saturated for values $|\Pi(n_j, z) - 1| > 3$.

green curves). Once again, we can identify a distinctive regime where the maximum damping and maximum growth reach similar magnitudes, as in the case of hosing. However, a crucial difference is that the dynamic amplitude response of the SMI is antisymmetric with respect to the HI, i.e., each non-resonant growth regime applies to opposite regions of k [compare Fig. 4.14b) to Fig. 3.3b)].

Most obvious in Fig. 4.14, though, is the difference between the two versions of the theory: the incomplete version (Eq. 4.12) in Fig. 4.14(a-b), and the complete version (Eq. 4.13) in Fig. 4.14(c-d). The latter exhibits multiple peaks of the amplitude response, in contrast to the single peak in Fig. 4.14a) [see also the line-outs in Fig. 4.14b)]. As discernible in Fig. 4.14d), these peaks are located at unit fractions of the plasma wavenumber, i.e., $k = k_p/N$ where $N \in \mathbb{N}^+$.

The phenomenon of subharmonic resonance can arise in parametric oscillators and nonlinear oscillating systems, where N commonly corresponds to the order of the nonlinearity [86] (e.g. an additional term proportional to $x^N(t)$ in Eq. 3.12). We note that no superharmonic resonances were observed when we extended the theoretical calculation beyond $k > 2\ k_p$, and that this phenomenon is not observed for the hosing instability when the complete, piecewise centroid equation is considered (Eq. 2.62).

Indeed, the explanation for the peaks found here can be attributed to the nonlinear character of the plasma response driving the SMI (Eq. 4.13). Contemplating the overall structure of Eq. 4.11, we immediately see that it is in fact a nonlinear differential equation when the right-hand side is given by Eq. 4.13, i.e., is a piecewise function of r_1. We can therefore expect the evolution of r_1 along z to be nonlinear. For any seed frequency $k_0 > 0$, this nonlinear evolution translates into a progressive distortion of the initially sinusoidal bunch radius perturbation, and therefore into the emergence of harmonics of k_0 in the Fourier space of r_1. Therefore, for seed frequencies that correspond to unit fractions of the plasma frequency, i.e., $k_0 = k_p/M$, the Mth harmonic of k_0 by definition corresponds to k_p, which allows this harmonic to grow resonantly. As an example, for

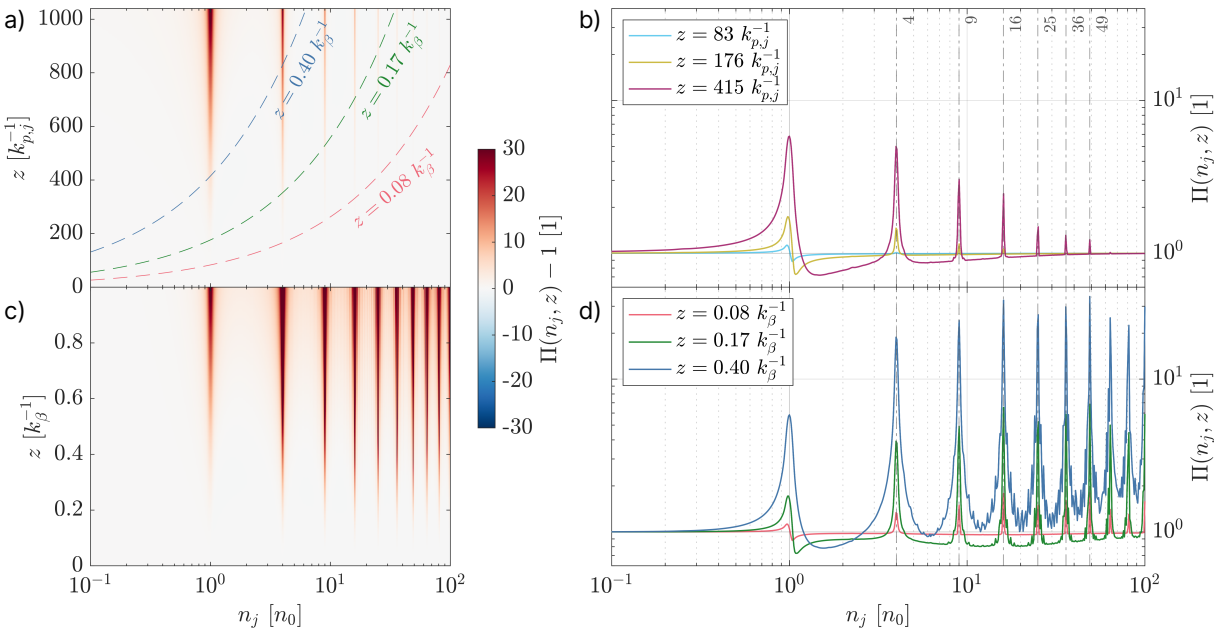

Figure 4.15: SMI amplitude response as a function of plasma density and propagation distance according to the complete theory (Eq. 4.13). In a)–b) the *normalized* propagation distance is kept constant for each plasma density n_j. The isoparametric curves in a) indicate edges in the data where the absolute propagation distance is fixed (expressed in terms of the betatron period, which does not depend on n_j). The data is plotted as a function of the *absolute* propagation distance in c)–d). Note that the color scale in a) and c) is saturated for values $|\Pi(n_j, z) - 1| > 30$.

the seed frequency $k_0 = \frac{1}{3}k_p$, the third harmonic ($M = 3$) corresponds to the plasma frequency and can thus grow resonantly.

This explanation justifies several properties of the subharmonic peaks: why they emerge along the propagation (since the growth of harmonics is tied to the development of the SMI), why their amplitude decreases with increasing M (higher-order harmonics have lower amplitudes), and why no peaks are observed for the incomplete version of the right-hand side Eq. 4.12 and for the hosing instability (the instability's right-hand side is linear in z).

If we considered a different frame of reference for the current study, where the initial perturbation wavenumber was held constant (as previously explored for the HI in Fig. 3.6 and in the accompanying text), we would expect to observe peaks of SMI growth as the plasma density is varied away from the resonant n_0.

Until now we have assumed a plasma with a fixed, constant density n_0, which determines the resonant plasma frequency $\omega_{p,0} = c\, k_{p_0}$. In order to map out the amplitude response, we then varied the perturbation wavelength $\lambda = 2\pi/k$ in an incoming bunch, whereby the observed physics depends on the ratio $k/k_{p,0}$. However, we could equally consider a fixed perturbation wavelength $\lambda_{p,0}$ of the incoming bunch, defined for a reference plasma density n_0 (for which the SMI would grow resonantly) and vary the plasma density n_j where the bunch propagates instead. We must observe the same physics in both cases, though the determining quantity in the latter case is now $k_{p,0}/k_{p,j}$. We can switch between both reference frames via the relationship $\hat{k} = 1/\sqrt{\hat{n}_j}$, where $\hat{n}_j = n_j/n_0$, which follows from the equality of both wavenumber ratios. Note that this correspondence is not strictly true, since in the second case we effectively alter the normalized bunch parameters as well, which should lead to different wakefields and growth rates.

Let us consider the seed frequency $k_{p,0}$ of a perturbed bunch propagating in plasma with density n_0 (resonant growth). The nonlinear evolution of the bunch radius oscillation then translates into the emergence of harmonics of $k_{p,0}$ in Fourier space, i.e., into growing signals at $2\,k_{p,0}$, $3\,k_{p,0}$, and

so on. Now, consider that each of these harmonics, $k_H = M k_{p,0}$ for $M \in \{2, 3, \dots\}$, corresponds to the fundamental plasma frequency for a plasma density n_H, which is given by:

$$\frac{k_H}{k_{p,0}} = M = \sqrt{\frac{n_H}{n_0}} \quad \Leftrightarrow \quad n_H = M^2\, n_0\ . \tag{4.16}$$

Whereas we found the subharmonic peaks in the fixed-density reference frame at $k_{\mathrm{SH}} = k_p/M$, in the fixed-perturbation frame we therefore expect the peaks to be located at $n_{\mathrm{SH}} = M^2 n_0$.

This is confirmed in Fig. 4.15, where the theoretical amplitude response was computed in the fixed-perturbation frame. The normalized bunch parameters were updated and the equations were renormalized for each value of n_j. In Fig. 4.15a) the propagation distance is normalized to $k_{p,j}^{-1}$, the plasma skin depth associated with each value of n_j, which allows us to observe several subharmonic peaks at $n_j = \{4, 9, 16, 25, \dots\}\, n_0$ [see Fig. 4.15b)], as expected from Eq. 4.16. In a realistic experimental set-up, however, the propagation distance might be fixed while the plasma density is scanned. The expected growth observation in this case is shown in Figs. 4.15c–d) as a function of $z k_\beta^{-1}$, which is fixed for a set of bunch parameters and independent of n_j. Note the prediction of faster growth to be observed at subharmonic multiples of the reference density in such a set-up.

We will now proceed to the validation of the theoretical predictions described above using PIC simulations.

The SMI amplitude response and subharmonic resonance according to PIC simulations

The SMI amplitude response obtained from the simulations is shown in Fig. 4.16 for two different phases of its evolution. The theoretical expectation (both versions) was added for a qualitative comparison, at arbitrary propagation distances that best seem to approach the simulation data. A quantitative discrepancy is to be expected here due to the different transverse profiles of the bunch and the extensive assumptions underlying the theory.

The shape of the early amplitude response [see Fig. 4.16a), red cross symbols] agrees with the two versions of the theory, although it seems to feature a negative offset. This offset could be due to some nonlinear component of the self-focusing effect that could not be removed by the subtraction of the seedless case ($\sigma_{r,\mathrm{adiab}}$) alone, and which would decrease the amplitude of the radius perturbation independently of its frequency. In any event, this early regime displays

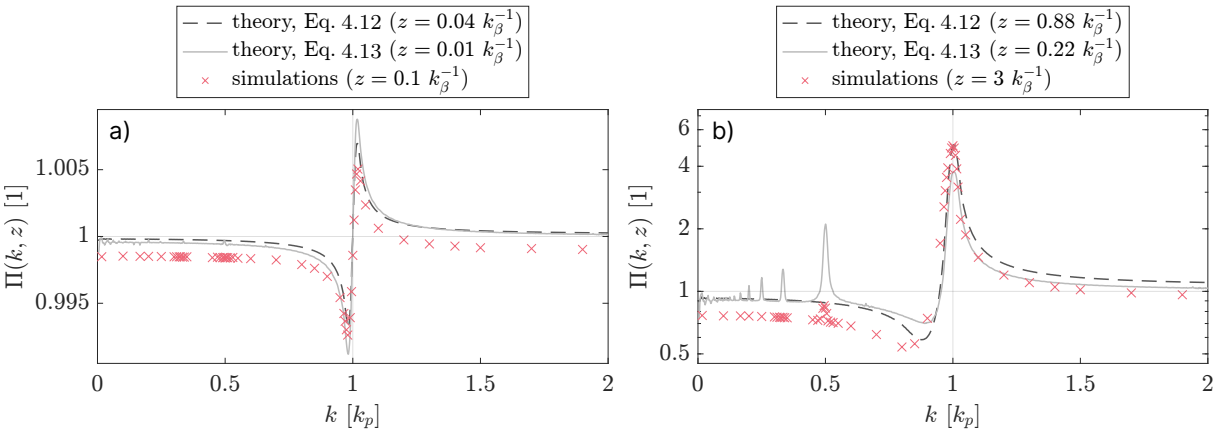

Figure 4.16: Qualitative comparison of the amplitude response obtained from OSIRIS 2D axisymmetric simulations and two versions of the theory at an early (a) and late (b) phase of the evolution. Note that the vertical axis in b) scales logarithmically.

the same characteristics as in the case of hosing (see p. 46), with the obvious exception of the antisymmetry with respect to the axis $k = k_p$.

At later times there is worse agreement with the theoretical models, with a persisting negative offset in the simulation data [see Fig. 4.16b), red cross symbols]. However, crucially for this comparison, the subharmonic peak at $k = \frac{1}{2}k_p$ grows noticeably before $z = 3\,k_\beta^{-1}$, although its relative magnitude is smaller than the full theory would predict for a flat-top bunch (by a factor of ~ 5.5 versus ~ 2). This implies that, even for a smooth transverse bunch profile (Gaussian-shaped), there is some degree of nonlinearity in the plasma response driving the SMI.

From this, we could assume that the nonlinearity of the plasma response is determined by how quickly the transverse profile varies along the transverse coordinate. In that case, the flat top would represent one extreme of this sliding scale, varying infinitely quickly and leading to infinite degrees of nonlinearity. The opposite extreme would consist of a wide-bunch limit where the transverse profile could be considered infinitely smooth (i.e., where $\partial g(r)/\partial r$ could be neglected). Enforcing this limit in the envelope equation, however, leads to the result that $\langle rF_r \rangle = 0$ and thus that the SMI does not develop. We must therefore conclude that the plasma response driving the SMI is always nonlinear to some degree.

The hypothesis that steeper profiles increase the nonlinearity of the SMI can be tested by replacing the transverse profile in the simulations with a super-Gaussian formula,

$$g(r,\zeta) = \exp\left[-\left(\frac{r^2}{\sigma_r^2(\zeta)}\right)^p\right] , \tag{4.17}$$

with increasing powers p. We choose the exponents $p = 2$ and $p = 4$, taking care to adjust each standard deviation of the super-Gaussian profiles $\sigma_{r,p=2}$ and $\sigma_{r,p=4}$ such that the charge per slice in ζ is conserved between the three cases. The resulting profiles are shown in Fig. 4.17a), with $\sigma_{r,p=2}/\sigma_r = \sqrt{2}/\pi^{1/4} \approx 1.06$ and $\sigma_{r,p=4}/\sigma_r = 2/\sqrt{\Gamma(1/4)} \approx 1.05$. All other simulation parameters are maintained (see Table A.6, items A.6.6–A.6.7, in Appx. A for the full simulation details). Note the higher frequency content along r for the steeper profiles, evident in Fig. 4.17b) via the Fourier transforms of each profile.

Figure 4.18 ($p = 1$, top) represents the same simulation data discussed in Fig. 4.16, i.e., for a purely Gaussian transverse bunch profile. Though the simulations were conducted at closely spaced seed wavenumbers to resolve potential peaks, there is no evidence of growth of the second subharmonic ($k = k_p/3$) up to $z = 3\,k_\beta^{-1}$.

As we increase the steepness of the transverse profile, however, both the first ($k = k_p/2$) and second subharmonic resonance peaks become more prominent and emerge earlier (compare

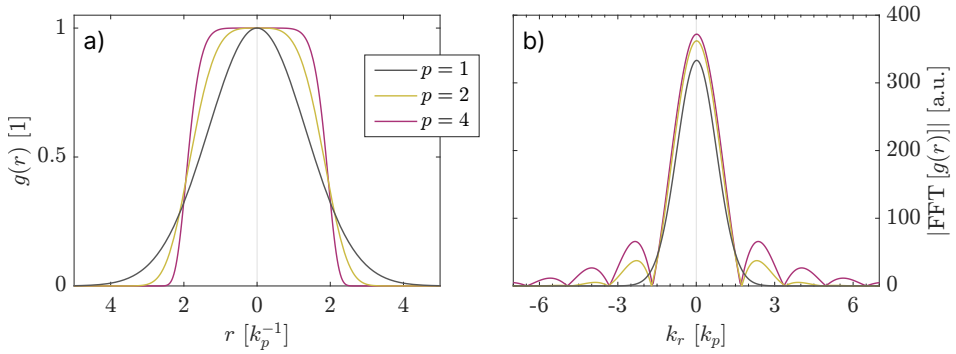

Figure 4.17: Transverse shape of the bunch density profiles used in the 2D axisymmetric simulations (a), and their Fourier transforms along the radial coordinate (b).

with Fig. 4.18, $p = 2$ and $p = 4$). This could be justified by the higher frequency content of the super-Gaussian profiles [see Fig. 4.17b)] and of the respective initial plasma responses $\langle rF_r \rangle / \sigma_r$ (not shown). Transfiguring $g(r)$ closer to a flat top additionally seems to have an effect on the amplitude response away from the fundamental resonance after some propagation, both for $k \to 0$ and $k \to \infty$, whereby the radius modulation is further decreased ($\Pi(k, z) < 1$).

The quantity shown in Fig. 4.18 and previous figures conveys information about how much the oscillation in the beam envelope grows, but not at which frequency (or frequencies). At the subharmonic resonance peaks, for example, is it truly the Mth harmonic corresponding to k_p that is contributing to the increased growth factor?

A naive look at the bunch radius line-outs along ζ for $k = \frac{1}{2}k_p$ and $k = \frac{1}{3}k_p$, shown in Fig. 4.19, seems to suggest a positive answer. After propagating $0.7\ \mathrm{m}$ in plasma, we see evidence of a radius modulation in the super-Gaussian bunch ($p = 4$) at double the initial perturbation frequency which seems to be growing along the bunch (see Fig. 4.19, top). The same applies for the super-Gaussian bunch seeded at $k = \frac{1}{3}k_p$, where this time the growing modulation seems to correspond to three times the initial frequency and exhibits a smaller amplitude at the same propagation distance.

We can repeat this analysis systematically by computing the fast Fourier transform of the bunch radius perturbation along ζ at a given z and comparing the Fourier-space signals to each

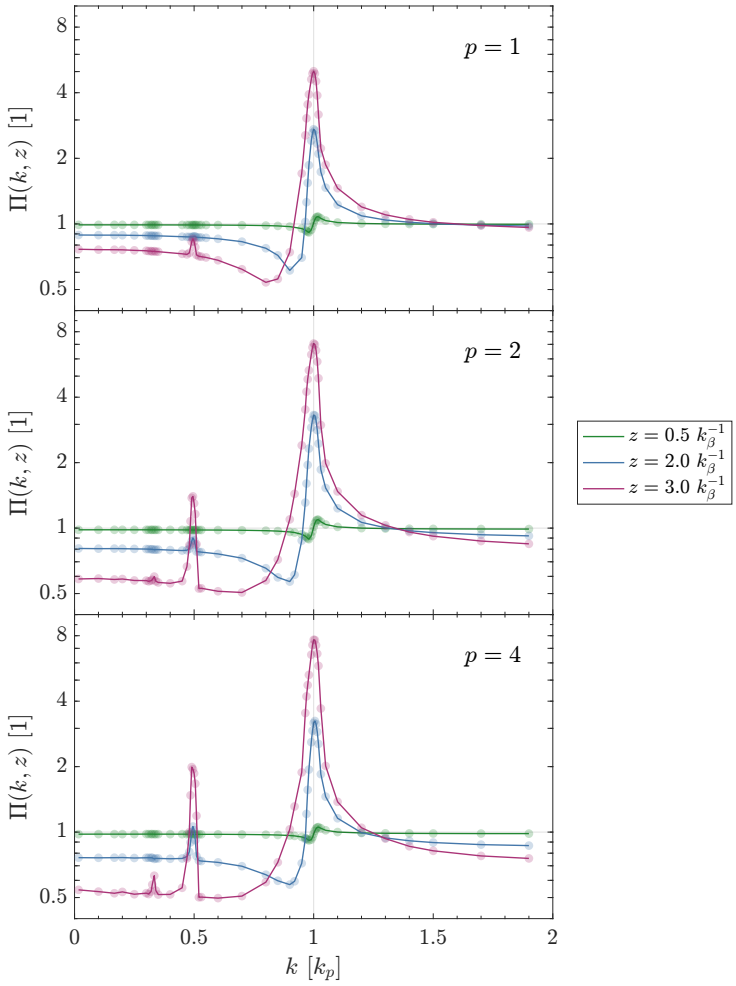

Figure 4.18: Amplitude response of the SMI measured from the OSIRIS 2D axisymmetric simulations for different transverse bunch profiles, defined by the super-Gaussian exponent p (top to bottom), and at different propagation distances (line and symbol colors, see legend). Each circle symbol on a given curve represents the data from one simulation. Note the logarithmic scaling of the vertical axis.

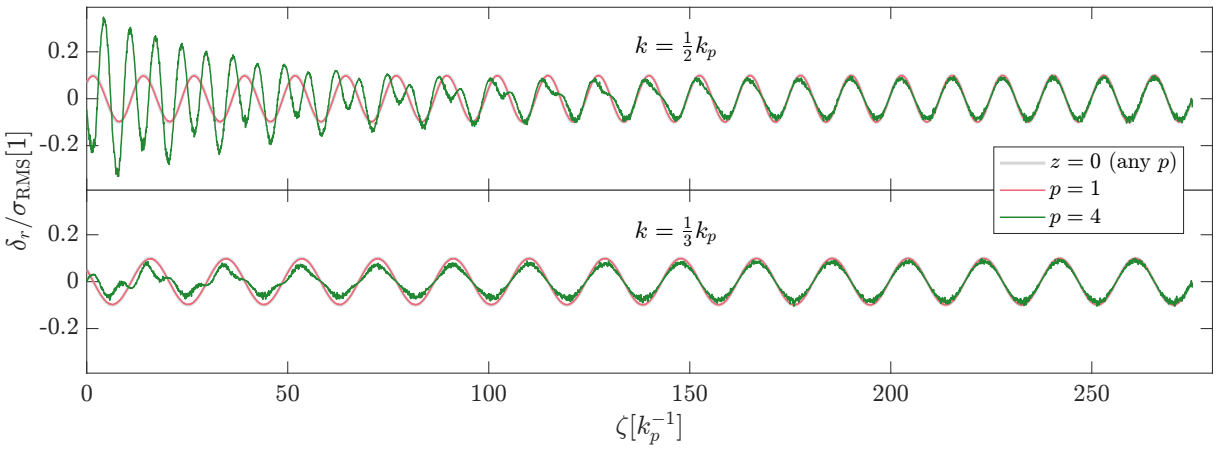

Figure 4.19: Normalized bunch radius perturbation for a Gaussian (red, $p = 1$) and a super-Gaussian (green, $p = 4$) transverse profile after propagating $0.7\ k_\beta^{-1}$, and for the first ($k = \frac{1}{2}k_p$, top) and second ($k = \frac{1}{3}k_p$, bottom) subharmonic resonances. The initial perturbation is shown in the background in grey (hardly visible due to its overlap with the red curves). Results from OSIRIS 2D cylindrical simulations.

initial perturbation frequency. The result of this procedure is shown in Fig. 4.20 for three different inputs (corresponding to each row): the theoretical data, and simulation data for two transverse profiles (Gaussian and super-Gaussian with $p = 4$). The horizontal axis for each plot (k_0) represents the initial perturbation frequency. For each k_0, the Fourier spectrum of the bunch radius at z is plotted along the vertical axis as a function of the transform variable $\tilde{k}$, the spectrum values being represented by the color scale.

At $z = 0$ (see left-hand column of Fig. 4.20) we naturally expect to observe a direct correlation $\tilde{k}(k_0) = k_0$, since the bunch radius is initially sinusoidally modulated at k_0. As the bunch propagates and the SMI evolves, we would expect to observe harmonics of k_0 in the Fourier spectra of the radius, i.e., zero-crossing lines with increasing slope. This is indeed what we observe in Fig. 4.20b) (the theoretical, flat-top case), though we note the absence of the lines $\tilde{k}(k_0) = Mk_0$ for odd harmonics M. As it stands we have not been able to find an explanation for why this is so. Nevertheless, the integrated Fourier spectra (along $\tilde{k}$) in Fig. 4.20b) still exhibit subharmonic peaks at all $k_0 = k_p/M$ (including for odd M), similarly to the curves shown in Fig. 4.14d).

In the case of the simulations, in Figs. 4.20d) and f), we see evidence of the growth of several harmonics, even or odd. This is most clearly visible for the super-Gaussian transverse profile: notice the signals at $\tilde{k}(k_0 = k_p) = 3k_p$, $\tilde{k}(k_0 = \frac{1}{3}k_p) = 3\frac{1}{3}k_p$, and $\tilde{k}(k_0 = \frac{1}{2}k_p) = 3\frac{1}{2}k_p$ in Fig. 4.20f). Interestingly, some additional signatures are visible in the simulation data, once again most perceptibly in Fig. 4.20f) (see faint diagonals). These homogeneous Fourier-space signals are visible at $\tilde{k}(k_0) = \pm(k_p \pm k_0)$, and represent a beat between the seed frequency k_0 and the plasma frequency k_p. More importantly, however, the simulation data seems to confirm our initial supposition that most of the growth observed in the subharmonic resonances is associated with a k_p-oscillating component of the radius perturbation.

The SMI phase response

If we interpret the SMI as an oscillator (the bunch radius) driven by a periodic, sinusoidal force, we expect to see a particular behavior in the phase shift between the oscillator and the periodic force, as discussed in Sec. 3.2.1. The envelope equation in cylindrical coordinates (see p. 24),

$$\frac{d^2\sigma_r}{dz^2} - \frac{\varepsilon_y^2}{2\,\sigma_r^3} = \frac{m_e}{\gamma M_b}\frac{\langle r\ F_r\rangle}{\sigma_r}\ , \tag{4.18}$$

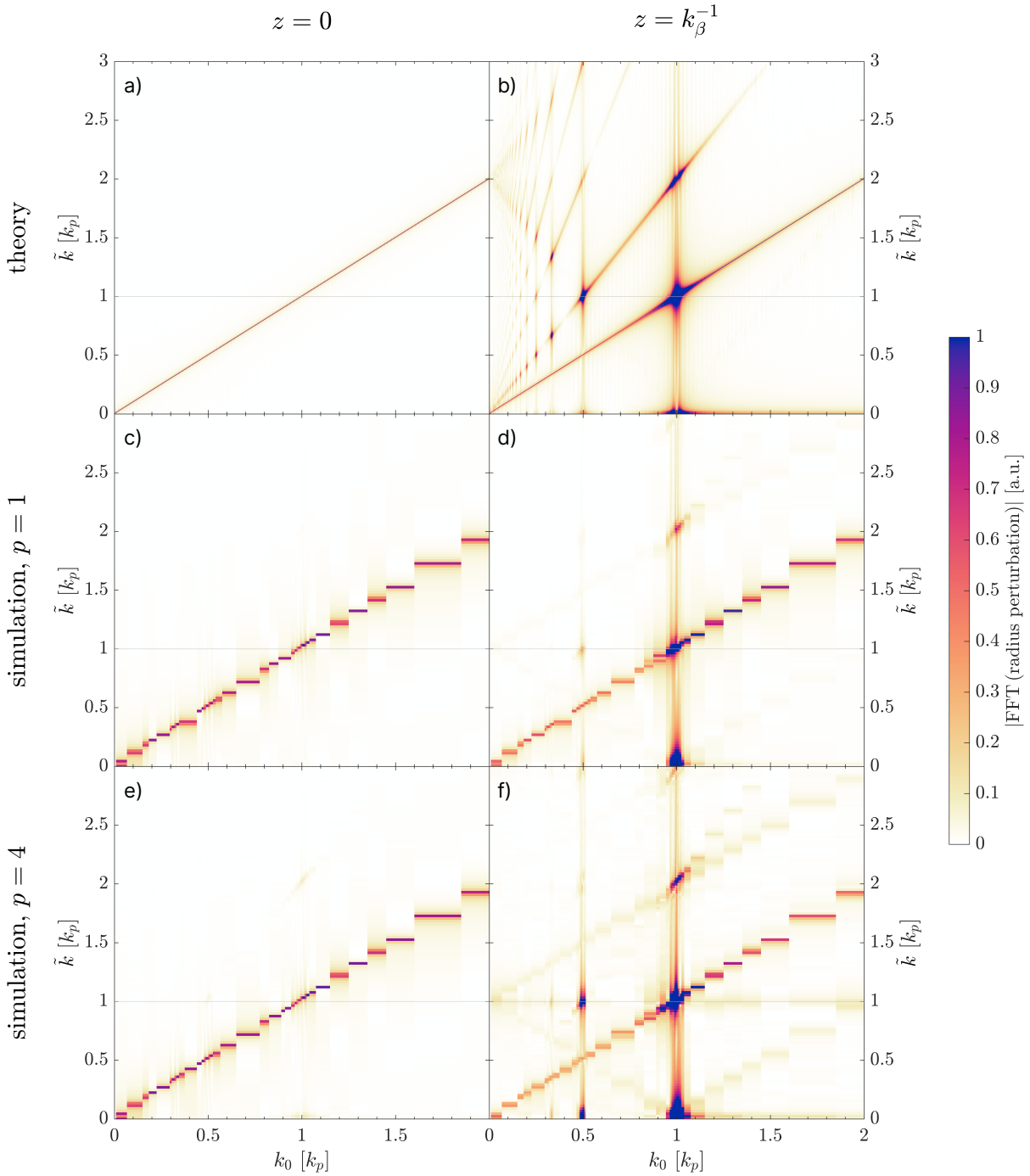

Figure 4.20: Discrete Fourier transform of the perturbation radius (r_1 for the theory and $\sigma_r - \sigma_{r,\mathrm{adiab}}$ for the simulations) as a function of the seed wavenumber k_0, at $z = 0$ (left-hand column) and at $z = k_\beta^{-1}$ (right-hand column), according to theory (a–b), and to simulations with a Gaussian (c–d) and a super-Gaussian (e–f) transverse profile. Each column of data in each plot corresponds to the Fourier spectrum obtained for an initial radius perturbation at k_0. Horizontal guide lines (grey) help locate the plasma frequency in the transform-variable axis $\tilde{k}$. Note that each dataset is normalized to its maximum value at $z = 0$, and that the range of the color scale is limited to this value (values above 1 are indistinguishable).

tells us that two effects play a role in the evolution of the RMS size: one associated with the bunch emittance (second term on the left-hand side) and one associated with the plasma response (right-hand side). Here, the quantity $\langle rF_r \rangle / \sigma_r$ corresponds to the force driving the oscillator. We therefore compare its early relationship to the RMS bunch size σ_r, which is illustrated in Fig. 4.21a) with curves obtained from the 2D axisymmetric simulations at $z \approx 0$. We once again observe three distinct phase shifts between σ_r and $\langle r\ F_r \rangle / \sigma_r$, depending on the seed frequency k relative to k_p.

A comprehensive picture of the phase shift $\Delta\phi$ as a function of seed frequency is given in Fig. 4.21b), based on the theory for a flat-top transverse profile as well as the simulation data. The theoretical phase shift is measured between r_1 and the first-order plasma response $F_{\mathrm{SM},1}$, which follows from the assumption of a small radius perturbation, such that $\langle rF_r \rangle / r_b = F_{\mathrm{SM},0} + F_{\mathrm{SM},1}$. These two plasma response components can be found by writing out the sum of $d^2 r_0/dz^2$ (Eq. 2.105) and $d^2 r_1/dz^2$ (the right-hand side in Eq. 4.13):

$$\frac{d^2}{dz^2}\left(r_0 + r_1\right) - \frac{\varepsilon^2}{r_0^3} = \frac{2\, m_e}{\gamma M_b}\left(F_{\mathrm{SM},0} + F_{\mathrm{SM},1}\right)\ , \tag{4.19}$$

with

$$F_{\mathrm{SM},0} = 2\,\frac{n_{b0}}{n_0}\left(\frac{q_b}{e}\right)^2 I_2(r_0) K_1(r_0) \int_\zeta^\infty d\zeta' \sin(\zeta - \zeta') f(\zeta')\ , \tag{4.20}$$

$$F_{\mathrm{SM},1} = -\frac{1}{2}\frac{n_{b0}}{n_0}\left(\frac{q_b}{e}\right)^2 \int_\zeta^\infty d\zeta' \sin(\zeta - \zeta') f(\zeta') \begin{cases} \left[2\,\kappa_<^2\, r_1(\zeta) - \nu\, r_1(\zeta')\right] & r_1(\zeta) \le r_1(\zeta') \\ \left[2\,\kappa_>^2\, r_1(\zeta) + \nu\, r_1(\zeta')\right] & r_1(\zeta) > r_1(\zeta') \end{cases}\ . \tag{4.21}$$

By contrast, in the simulations $\Delta\phi$ is measured between σ_r and $\langle rF_r \rangle / \sigma_r$, though the adiabatic component of the plasma response is discarded by the phase shift measurement procedure described in Appx. B.

The result of the phase shift analysis in Fig. 4.21b) demonstrates excellent agreement between theory and simulations, despite the different transverse bunch profiles in each case. The physics of this lag between driving force and radius oscillation thus seems to be independent of the bunch's transverse characteristics. Note that the two versions of the theory, piecewise (green curve) and single-branch (yellow curve) overlap completely. It therefore makes sense that there is also no impact on the result when the two versions of the theory are considered, since this discrepancy

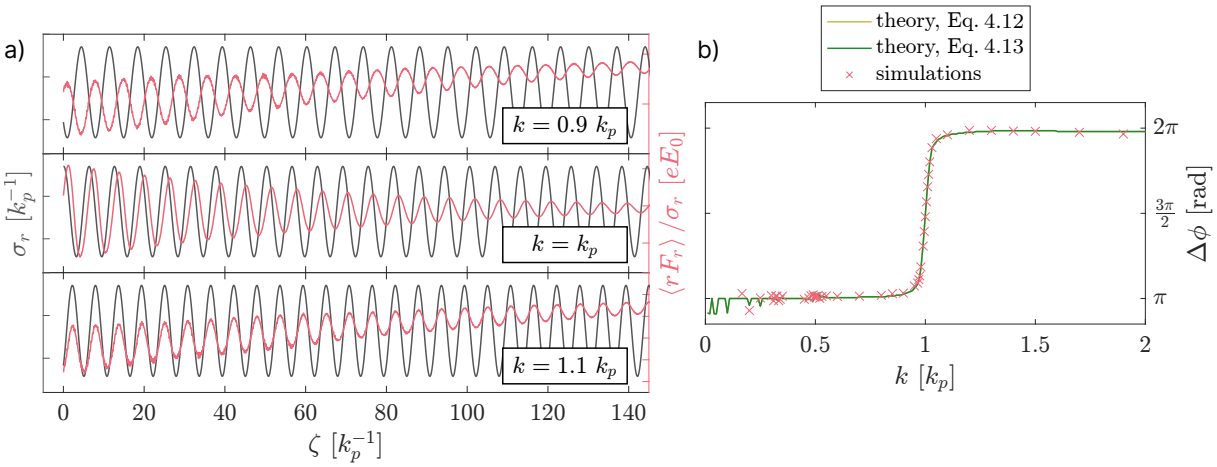

Figure 4.21: a) Initial RMS bunch radius (dark grey) and SMI-driving plasma response (red) for three different seed wavenumbers, obtained from OSIRIS 2D axisymmetric simulations at $z = 0$. b) Phase shift between the initial σ_r and $\langle r\ F_r \rangle / \sigma_r$ (simulations, red cross symbols) or r_1 and $F_{\mathrm{SM},1}$ (theory, green) as a function of the seed wavenumber, according to simulations and to two versions of the theory.

stems from the algebra associated with the averaging over the transverse profile.

4.2.3 Understanding the effect of a plasma density step

For acceleration purposes, the self-modulation instability proves itself an extremely useful mechanism, since it provides high wakefield amplitudes for drivers that would otherwise be unfit for that purpose. Nevertheless, the phase of resonant growth associated with the instability's development eventually reaches a saturation point [see Fig. 4.22a), solid grey curve at $z \approx 5$ m]. Left to its own devices, the particle charge in each microbunch is then continuously eroded by a backwards-slipping wakefield, due to a residual difference between the wakefield phase velocity and the bunch velocity ($\approx c$). The wakefield amplitude therefore drops after the saturation peak [see Fig. 4.22a), grey curves for $z \gtrsim 5$ m].

Previous work based on 2D axisymmetric quasistatic PIC simulations suggests that a small step in the plasma density profile, located relatively early along the development of the SMI, leads to a stable wakefield amplitude after saturation and thus makes it possible to sustain an approximately constant, elevated acceleration gradient [71, 72]. This effect is exemplified in Fig. 4.22a) for a plasma density step increase of 3% (solid red curve). This solution is therefore extremely interesting for the AWAKE experiment, which aims to leverage the self-modulation undergone by a long relativistic proton bunch for electron acceleration, and will be put to the test during the experiment's future program.

It is generally understood that the plasma density step implies a change of the plasma frequency, and therefore a sudden shift of the wakefields with respect to the modulating structure of the bunch. In particular, a positive step (i.e., the plasma density is increased above n_0) readjusts the plasma wavelength such that more bunch charge is caught in focusing fields, as demonstrated in Fig. 4.22b) (left-hand graph, red curve). This may be part of the reason why a high wakefield amplitude can be sustained long after the saturation point when a positive density step is used. Additionally, the positive density step seems to ensure that more energy is transferred from the bunch to the wakefields (i.e., more charge finds itself in decelerating wakefields) after saturation of the SMI [see Fig. 4.22b), right-hand graph].

To thoroughly understand the striking wakefield-sustaining effect behind the plasma density

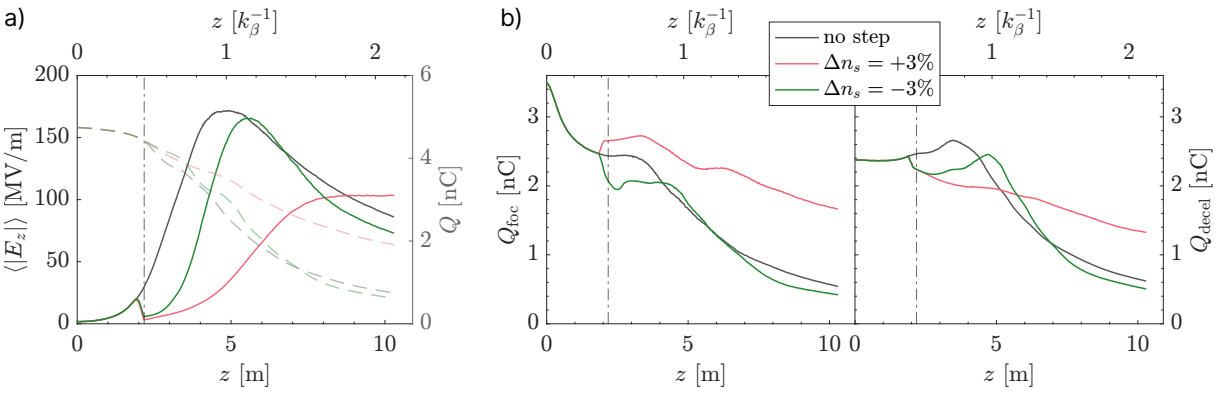

Figure 4.22: a) Average longitudinal wakefield amplitude (solid lines) and total driver bunch charge (dashed lines) within a radius of $1\ k_p^{-1}$ from the propagation axis, with plasma density steps [red and green, see legend in b)] and without (grey). b) Total driver bunch charge within $r \leq k_p^{-1}$ located in focusing (left) and decelerating (right) wakefields, with and without a step in the plasma density profile. The density steps are located at $z = 2.17$ m, indicated by the dash-dotted vertical lines, and they are implemented over a one-centimeter-long ($\sim 50\ k_p^{-1}$) ramp. Data obtained from OSIRIS 2D cylindrical simulations with nominal parameters for the AWAKE experiment (see simulation details in Table A.5, items A.5.3–A.5.5, in Appx. A).

step, however, it would be necessary to establish a theoretical model for the saturation phase of the SMI, which has so far not been accomplished by the scientific community (to the best of the author's current information). Nevertheless, we can at least verify whether the theoretical framework described in the previous sections of this chapter is consistent with the effects associated with the density step before saturation comes into play.

For our density step case study, we perform three simulations with the same bunch parameters as before: we simulate a 280-k_p^{-1}-long section of the front of a bunch composed of artificially light protons ($M_b = 50\, m_e$) propagating in plasma with the baseline density $n_0 = 2 \times 10^{14}\ \mathrm{cm}^{-3}$. We choose a step with a height of $\Delta n_s / n_0 = 4\%$, both above and below n_0, located at $z = 0.5\, k_\beta^{-1}$, and we compare both results to the baseline simulation, where there is no step. In all three cases, the SMI is seeded with a bunch radius perturbation at $k_{p,0}$.

One of the implications of the theoretical analysis is that each growth regime is associated with a specific phase shift between bunch radius and plasma response. When the plasma density n_p is larger than n_0 (or, equivalently, when $k < k_{p,0}$) we expect a phase shift of π and negative growth in the bunch radius modulation. Conversely, when $n_p < n_0$ (or $k > k_{p,0}$) we expect $\Delta\phi = \pi$ and a regime of "slow growth" [compare with Figs. 4.14, 4.15 and 4.21].

We can easily verify whether this is the case in the density step simulations by plotting the bunch radius and plasma response immediately after the step. This is shown in Fig. 4.23a). Without a density step, we observe the $3\pi/2$ phase shift associated with resonant growth of the SMI, as expected [compare Fig. 4.23a), top, to Fig. 4.21a), middle, on p. 75]. With a positive step, however, the plasma response is shifted forwards, although the observed phase shift does not perfectly correspond to π [compare Fig. 4.23a), middle, to Fig. 4.21a), top]. This is perhaps due to the relatively late placement of the density step along z. The opposite density step leads to a phase shift of 2π [see Fig. 4.23a), bottom], as predicted earlier.

The effect of each density step on the development of the SMI is illustrated in Fig. 4.23b), using the average amplitude of the wakefield component E_z to quantify the growth of the instability. The configuration chosen for this case study is not optimized to demonstrate the potential merits of the density step concept: not much wakefield growth can be observed along the limited region considered here, with a smoothly rising bunch, and the significant wakefield amplitude loss undergone when the step is introduced might be minimized by choosing a more adequate step location and height. Nevertheless, it is possible to see a plateauing of the wakefield amplitude

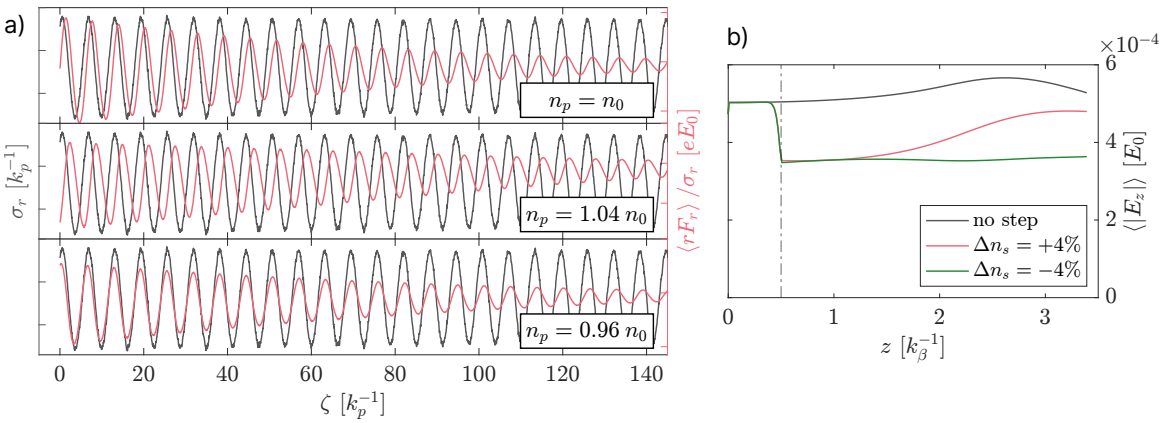

Figure 4.23: a) Initial RMS bunch radius (dark grey) and SMI-driving plasma response (red) at $z = 0.5\, k_\beta^{-1}$ for three different cases: with no density step, and with a step of $\pm 4\%$ (n_p indicates the current plasma density). b) Average longitudinal wakefield amplitude within $r \leq k_p^{-1}$ along the propagation distance for the three different cases. Data obtaind from OSIRIS 2D axisymmetric simulations.

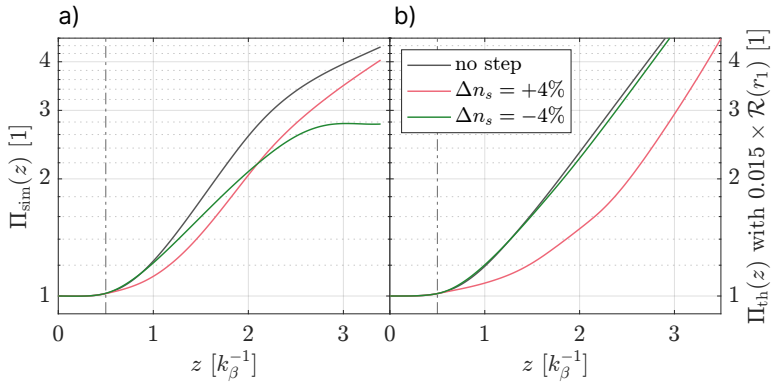

Figure 4.24: SMI amplitude response obtained from OSIRIS 2D cylindrical simulations (a) and from the theoretical model for a flat-top transverse bunch profile (b), for propagation in a plasma with and without a density step. The vertical dash-dotted lines mark the location of the density step.

after saturation ($z \approx 2.5 k_\beta^{-1}$) for $\Delta n_s = +4\%$ in Fig. 4.23b).

Note that this plasma density, $n_p = 1.04\, n_0$, corresponds to a regime of negative growth, which may seem counterintuitive in the context of optimizing the SMI for acceleration purposes. If we consider that the natural development of the SMI is associated with a gradual loss of driving charge (see Fig. 4.22), however, it may make sense to suddenly "slow down" its development such that a stable post-saturation state is found.

We can take a closer look at the growth of the bunch radius modulation from the simulation data by computing the amplitude response $\Pi_{\mathrm{sim}}(z) = \int d\zeta |\sigma_{r,1}(z)| / \int d\zeta |\sigma_{r,1}(0)|$, shown in Fig. 4.24a). For this set of simulations, the oscillatory component of the bunch radius $\sigma_{r,1}$ was obtained by subtracting the moving average of σ_r with a window length of $\lambda_{p,0}$. Note that the positive step results in an initially slower growth rate ($z < 2\, k_\beta^{-1}$) which later surpasses even the resonant rate [compare the red and dark grey curves in Fig. 4.24a) for $z \sim 3\, k_\beta^{-1}$].

We can also compare $\Pi_{\mathrm{sim}}(z)$ with a theoretical prediction for the amplitude response, shown in Fig. 4.24b). This amplitude response is defined as $\Pi_{\mathrm{th}}(z) = \int d\zeta |r_1(z)| / \int d\zeta |r_1(0)|$, where $r_1(z)$ is calculated with a renormalized version of the model in Eqs. 4.10 and 4.13, such that the local plasma density can be varied. Moreover, the plasma response $\mathcal{R}(r_1)$ was scaled by an arbitrary factor of 0.015, such that the theoretical data can be compared with the simulation data on equal scales. There is qualitative agreement for $z \lesssim 2\, k_\beta^{-1}$ (roughly the range of validity of the theoretical model): slower growth for $\Delta n_s = +4\%$, and briefly faster growth for $\Delta n_s = -4\%$ before it is overtaken by the resonant case (see green and dark grey curves in Fig. 4.24).

With this we can conclude that our understanding of the SMI (discussed in the previous sections) is consistent with the early effects observed when a plasma density step is introduced. This does not include post-saturation effects, since a general theoretical model that for this regime does not yet exist.

Chapter 5

Conclusion

This doctoral work set out to contribute to the understanding of the hosing and self-modulation instabilities, particularly in the regime of long particle bunches and linear wakefields. This was accomplished with a combination of analytical and numerical approaches.

The theoretical apparatus was introduced in **Chapter 2**. We presented a systematic and detailed derivation of the equations that are used to treat the HI and SMI in the long-bunch, overdense regime analytically. This included a derivation, discussion and comparison of evolution models (both existing and novel) for both instabilities.

Original results in Chapter 2:

- differential equation for the bunch centroid in 2D Cartesian coordinates for a Gaussian transverse profile (Eq. 2.36 on p. 17), which allows us to study the HI theoretically (in planar geometry) for a more realistic bunch shape
- correction to the differential equations for the bunch centroid and radius for a flat-top transverse profile in cylindrical coordinates (Eqs. 2.62 and 2.85 on p. 22), which revealed previously unknown phenomena related to the development of the SMI
- power series model to describe the bunch centroid and radius as a function of ζ and z during early instability development (Eqs. 2.122–2.123 on p. 35), providing an analytical tool to study both instabilities in a regime that is partly not contemplated in existing evolution models

At the end of Chapter 2, we concluded that the power series model is especially useful at the front of the bunch during the instabilities' growth, where asymptotic models are not valid. Both this and the other original results were crucial to studying novel phenomena of the HI and SMI in the rest of this dissertation. Nevertheless, there is still much to explore in terms of the theory.

Future work ideas related to Chapter 2:

- understand the reason for the different amplitudes of the theory for the SMI and the simulation data (Fig. 2.6 on p. 27)
- investigate the importance of the assumption $r_1 \ll 1$ when modeling the SMI via a bunch

radius perturbation (p. 31)

- develop an asymptotic theory for the SMI that takes the full piecewise plasma response into account, thereby possibly leading to a different result for the growth rate (at k_p)
- develop theoretical models to describe the saturation phase of both instabilities, but most importantly the SMI

In **Chapter 3** we aimed to understand the dependence of the growth of hosing on a perturbation frequency. After obtaining a dispersion relation for the HI in particle beams with established techniques, we then explored a different approach that takes the onset of the instability into account (using the power series model), and found a different growth behavior than the dispersion relation would predict. We made use of a simple physical model, consisting of a sinusoidally driven harmonic oscillator, to better understand the early amplitude response we found with the power series model.

Our result showed different growth regimes (including damping) as a function of different seed frequencies, and was validated with PIC simulations. Lastly, we attempted to exploit these properties to devise a hosing mitigation method consisting of steps in the plasma density profile, i.e., in effect detuning the oscillator system. The limitations of this method were discussed, finding that the HI seems to be delayed rather than suppressed, and that the density steps may have a sizeable impact on the amplitude of the wakefields (36–44% decrease) when the bunch is also self-modulated.

Original results in Chapter 3:

- adiabatic dispersion relation for beam hosing in the long-bunch, overdense regime (Eq. 3.6 on p. 42), which fundamentally demonstrates that longer-wavelength modes of this instability may grow
- hosing amplitude response as a function of an arbitrary perturbation wavenumber, valid in particular during early instability development (Figs. 3.3 and 3.4 on p. 46), showing that it is possible to manipulate the instability's development via detuning techniques
- hosing mitigation method based on plasma density steps (Fig. 3.7 on p. 50), thereby expanding our understanding of hosing suppression in a long plasma-based accelerator

Though the mitigation setup we proposed does not seem to eliminate the hosing instability, it may be useful in affording the SMI enough time to dominate and thus making any further hosing growth impossible. Nevertheless, several questions remain to be answered.

Future work ideas related to Chapter 3:

- obtain an analytical expression for the amplitude response $\Pi(k, z)$ (Eq. 3.16 on p. 45)
- study the exchange of energy during the instability's development
- explore further plasma density profiles to control the development of hosing
- study the evolution of the phase response (Fig. 3.5 on p. 48) along propagation

- study the early amplitude response for hosing in other regimes (short bunch, nonlinear wakefields, etc.)

In the first part of **Chapter 4**, we demonstrated the robustness of the saturated SMI to fluctuations of the initial conditions. This included an analysis of the potential impact of these fluctuations on accelerated electrons, whereby we also tried to find optimal conditions for injection of these electrons. We then made a brief comparison of the results to subsequent experimental data published by the AWAKE Collaboration, which was consistent with our findings.

Original results in Chapter 4, Sec. 4.1:

- simulation-based evidence that the seeded SMI is resistant to input parameter fluctuations (Figs. 4.2 on p. 57 and 4.6 on p. 59), proving its suitability as a plasma-based acceleration mechanism
- finding that electrons injected before SMI saturation may remain trapped and reach high energies after 10 m when they are initially located far from the axis (Fig. 4.10 on p. 61), which is consistent with experimental results

In the second section of **Chapter 4**, we once again investigated how instability growth relates to a perturbation frequency, this time for the SMI. After obtaining the adiabatic dispersion relation for the SMI, we used the same approach as in Chapter 3 to predict its early amplitude response and found some unexpected behavior by considering the complete differential equation for the bunch radius found in Chapter 2. This behavior, which we termed “subharmonic resonance”, was confirmed with simulation data and is more pronounced the steeper the transverse bunch profile is. Finally, we interpreted the effects of a single plasma density step on the development of the SMI, proposed in Refs. [71, 72], from the perspective of the early amplitude response found above, and concluded that these effects are consistent with the framework developed in this section.

Original results in Chapter 4, Sec. 4.2:

- adiabatic dispersion relation for the SMI in the long-bunch, overdense regime (Eq. 4.5 on p. 64), which fundamentally demonstrates that longer-wavelength modes of this instability may grow
- amplitude response of the SMI as a function of an arbitrary perturbation wavenumber, valid in particular during early instability development (Figs. 4.14 on p. 68 and 4.16 on p. 70), showing that it is possible to manipulate the instability’s development via detuning techniques
- phenomenon of subharmonic resonance in the SMI (Figs. 4.15 on p. 69 and 4.18 on p. 72), which constitutes an entirely new aspect of the SMI to be explored
- understanding of the (early) effects of a plasma density step based on fundamental properties of the SMI (Figs. 4.23 and 4.24 on p. 77), which may contribute to an improved control over SMI-generated wakefields

Besides some of the ideas for future investigation mentioned in the context of the HI, which also apply to the SMI, the work in this chapter opens several avenues of inquiry. For example, our theoretical model suggests that the modulation of a bunch at the natural plasma frequency (in a plasma with density n_0) may be unaffected when propagating through plasma at a different density, as long as one of the subharmonic resonances is targeted (e.g. at $4\,n_0$). But there may be other interesting ramifications from this work.

Future work ideas related to Chapter 4:

- understand why the amplitude response of the SMI is antisymmetric to the HI
- investigate how the early amplitude response and its shifting maximum could impact the modulation frequency observed after saturation, which may not correspond to k_p exactly
- explore potential applications of the phenomenon of subharmonic resonance

The main theme emerging in the work developed for this dissertation is the idea of the hosing and self-modulation instabilities as systems that can be detuned and therefore influenced. Though this idea is not at all novel, the detailed implications of this approach have led us to surprising growth regimes and to the possibility of using the plasma density as a lever to manipulate the development of these instabilities. We hope that this proves fertile ground for further research.

Bibliography

[1] *More background on accelerators*, International Atomic Energy Agency, https://www.iaea.org/topics/nuclear-science/nuclear-research/accelerators/background (visited on 06/26/2023).

[2] V. A. Dolgashev, L. Faillace, B. Spataro, S. Tantawi, and R. Bonifazi, "High-gradient rf tests of welded X-band accelerating cavities", Physical Review Accelerators and Beams **24**, 081002 (2021).

[3] D. Broemmelsiek, B. Chase, D. Edstrom, E. Harms, J. Leibfritz, S. Nagaitsev, Y. Pischalnikov, A. Romanov, J. Ruan, W. Schappert, V. Shiltsev, R. Thurman-Keup, and A. Valishev, "Record high-gradient SRF beam acceleration at Fermilab", New Journal of Physics **20**, 113018 (2018).

[4] J. Liu et al., "World record 32.35 tesla direct-current magnetic field generated with an all-superconducting magnet", Superconductor Science and Technology **33**, 03LT01 (2020).

[5] *Facts and figures about the LHC | CERN*, https://home.web.cern.ch/resources/faqs/facts-and-figures-about-lhc (visited on 06/27/2023), the average exchange rate used to estimate the construction cost in Euros was 1.00 CHF = 0.70 EUR.

[6] M. Benedikt et al., *Future Circular Collider - European Strategy Update Documents*, technical report (CERN, Geneva, 2019), the average exchange rate used to estimate the construction cost of Stage 1 in Euros was 1.00 CHF = 1.02 EUR.

[7] T. Behnke, J. E. Brau, B. Foster, J. Fuster, M. Harrison, J. M. Paterson, M. Peskin, M. Stanitzki, N. Walker, and H. Yamamoto, *The International Linear Collider Technical Design Report - Volume 1: Executive Summary*, technical report (2013), the budget estimate in ILCU was converted to Euros using 1 ILCU = 1.25 EUR.

[8] T. Tajima and J. M. Dawson, "Laser Electron Accelerator", Physical Review Letters **43**, 267–270 (1979).

[9] R. D. Ruth, A. W. Chao, P. L. Morton, and P. B. Wilson, "A plasma wake field accelerator", Particle Accelerators **17**, 171–189 (1985).

[10] P. Chen, J. M. Dawson, R. W. Huff, and T. Katsouleas, "Acceleration of Electrons by the Interaction of a Bunched Electron Beam with a Plasma", Physical Review Letters **54**, 693–696 (1985).

[11] T. Kurz et al., "Demonstration of a compact plasma accelerator powered by laser-accelerated electron beams", Nature Communications **12**, 2895 (2021).

[12] A. J. Gonsalves et al., "Petawatt Laser Guiding and Electron Beam Acceleration to 8 GeV in a Laser-Heated Capillary Discharge Waveguide", Physical Review Letters **122**, 084801 (2019).

[13] S. Steinke, J. van Tilborg, C. Benedetti, C. G. R. Geddes, C. B. Schroeder, J. Daniels, K. K. Swanson, A. J. Gonsalves, K. Nakamura, N. H. Matlis, B. H. Shaw, E. Esarey, and W. P. Leemans, "Multistage coupling of independent laser-plasma accelerators", Nature **530**, 190–193 (2016).

[14] S. M. Hooker, R. Bartolini, S. P. D. Mangles, A. Tünnermann, L. Corner, J. Limpert, A. Seryi, and R. Walczak, "Multi-pulse laser wakefield acceleration: a new route to efficient, high-repetition-rate plasma accelerators and high flux radiation sources", Journal of Physics B: Atomic, Molecular and Optical Physics **47**, 234003 (2014).

[15] M. Litos et al., "High-efficiency acceleration of an electron beam in a plasma wakefield accelerator", Nature **515**, 92–95 (2014).

[16] C. A. Lindstrøm et al., "Energy-Spread Preservation and High Efficiency in a Plasma-Wakefield Accelerator", Physical Review Letters **126**, 014801 (2021).

[17] F. Peña et al., "Energy Depletion and Re-Acceleration of Driver Electrons in a Plasma-Wakefield Accelerator", preprint, arXiv:2305.09581 [physics.acc-ph], 10.48550/arXiv.2305.09581 (2023).

[18] E. Gschwendtner et al. (AWAKE Collaboration), "AWAKE, The Advanced Proton Driven Plasma Wakefield Acceleration Experiment at CERN", Nuclear Instruments and Methods in Physics Research Section A: Accelerators, Spectrometers, Detectors and Associated Equipment **829** *2nd European Advanced Accelerator Concepts Workshop - EAAC 2015*, 76–82 (2016).

[19] P. Muggli et al. (AWAKE Collaboration), "AWAKE readiness for the study of the seeded self-modulation of a 400 GeV proton bunch", Plasma Physics and Controlled Fusion **60**, 014046 (2017).

[20] E. Adli et al. (AWAKE Collaboration), "Acceleration of electrons in the plasma wakefield of a proton bunch", Nature **561**, 363–367 (2018).

[21] S. Corde et al., "Multi-gigaelectronvolt acceleration of positrons in a self-loaded plasma wakefield", Nature **524**, 442–445 (2015).

[22] R. D'Arcy et al., "Recovery time of a plasma-wakefield accelerator", Nature **603**, 58–62 (2022).

[23] C. A. Lindstrøm et al., "Preservation of beam quality in a plasma-wakefield accelerator", preprint, 10.21203/rs.3.rs-2300900/v1 (2023).

[24] W. Lu, C. Huang, M. Zhou, W. B. Mori, and T. Katsouleas, "Nonlinear Theory for Relativistic Plasma Wakefields in the Blowout Regime", Physical Review Letters **96**, 165002 (2006).

[25] W. Lu, C. Huang, M. Zhou, M. Tzoufras, F. S. Tsung, W. B. Mori, and T. Katsouleas, "A nonlinear theory for multidimensional relativistic plasma wave wakefields", Physics of Plasmas **13**, 056709 (2006).

[26] T. C. Katsouleas, S. Wilks, P. Chen, J. M. Dawson, and J. J. Su, "Beam Loading in Plasma Accelerators", Particle Accelerators **22**, 81–99 (1987).

[27] V. K. B. Olsen, E. Adli, and P. Muggli, "Emittance preservation of an electron beam in a loaded quasilinear plasma wakefield", Physical Review Accelerators and Beams **21**, 011301 (2018).

[28] M. Tzoufras, W. Lu, F. S. Tsung, C. Huang, W. B. Mori, T. Katsouleas, J. Vieira, R. A. Fonseca, and L. O. Silva, "Beam Loading in the Nonlinear Regime of Plasma-Based Acceleration", Physical Review Letters **101**, 145002 (2008).

[29] T. N. Dalichaouch, X. L. Xu, A. Tableman, F. Li, F. S. Tsung, and W. B. Mori, "A multi-sheath model for highly nonlinear plasma wakefields", Physics of Plasmas **28**, 063103 (2021).

[30] C. A. Lindstrøm et al., "Energy-Spread Preservation and High Efficiency in a Plasma-Wakefield Accelerator", Physical Review Letters **126**, 014801 (2021).

[31] C. Rechatin, X. Davoine, A. Lifschitz, A. B. Ismail, J. Lim, E. Lefebvre, J. Faure, and V. Malka, "Observation of Beam Loading in a Laser-Plasma Accelerator", Physical Review Letters **103**, 194804 (2009).

[32] C. Rechatin, J. Faure, A. Ben-Ismail, J. Lim, R. Fitour, A. Specka, H. Videau, A. Tafzi, F. Burgy, and V. Malka, "Controlling the Phase-Space Volume of Injected Electrons in a Laser-Plasma Accelerator", Physical Review Letters **102**, 164801 (2009).

[33] M. Kirchen, S. Jalas, P. Messner, P. Winkler, T. Eichner, L. Hübner, T. Hülsenbusch, L. Jeppe, T. Parikh, M. Schnepp, and A. R. Maier, "Optimal Beam Loading in a Laser-Plasma Accelerator", Physical Review Letters **126**, 174801 (2021).

[34] S. Jalas, M. Kirchen, P. Messner, P. Winkler, L. Hübner, J. Dirkwinkel, M. Schnepp, R. Lehe, and A. R. Maier, "Bayesian Optimization of a Laser-Plasma Accelerator", Physical Review Letters **126**, 104801 (2021).

[35] A. Ferran Pousa, I. Agapov, S. A. Antipov, R. W. Assmann, R. Brinkmann, S. Jalas, M. Kirchen, W. P. Leemans, A. R. Maier, A. Martinez de la Ossa, J. Osterhoff, and M. Thévenet, "Energy Compression and Stabilization of Laser-Plasma Accelerators", Physical Review Letters **129**, 094801 (2022).

[36] C. A. Lindstrøm, "Self-correcting longitudinal phase space in a multistage plasma accelerator", preprint, arXiv:2104.14460 [physics.acc-ph], `10.48550/arXiv.2104.14460` (2021).

[37] W. Wang et al., "Free-electron lasing at 27 nanometres based on a laser wakefield accelerator", Nature **595**, 516–520 (2021).

[38] R. Pompili et al., "Free-electron lasing with compact beam-driven plasma wakefield accelerator", Nature **605**, 659–662 (2022).

[39] V. K. Neil, L. S. Hall, and R. K. Cooper, "Further theoretical studies of the beam breakup instability", Particle Accelerators **9**, 213–222 (1979).

[40] E. Gschwendtner et al. (AWAKE Collaboration), "The AWAKE Run 2 Programme and Beyond", Symmetry **14**, 1680 (2022).

[41] A. Aschikhin et al., "The FLASHForward facility at DESY", Nuclear Instruments and Methods in Physics Research Section A: Accelerators, Spectrometers, Detectors and Associated Equipment **806**, 175–183 (2016).

[42] C. B. Schroeder, C. Benedetti, E. Esarey, F. J. Grüner, and W. P. Leemans, "Growth and Phase Velocity of Self-Modulated Beam-Driven Plasma Waves", Physical Review Letters **107**, 145002 (2011).

[43] C. B. Schroeder, C. Benedetti, E. Esarey, F. J. Grüner, and W. P. Leemans, "Coupled beam hose and self-modulation instabilities in overdense plasma", Phys. Rev. E **86**, 026402 (2012).

[44] C. B. Schroeder, C. Benedetti, E. Esarey, F. J. Grüner, and W. P. Leemans, "Coherent seeding of self-modulated plasma wakefield accelerators", Physics of Plasmas **20**, 056704 (2013).

[45] J. Vieira, W. B. Mori, and P. Muggli, "Hosing Instability Suppression in Self-Modulated Plasma Wakefields", Physical Review Letters **112**, 205001 (2014).

[46] R. A. Fonseca, L. O. Silva, F. S. Tsung, V. K. Decyk, W. Lu, C. Ren, W. B. Mori, S. Deng, S. Lee, T. Katsouleas, and J. C. Adam, "OSIRIS: A Three-Dimensional, Fully Relativistic Particle in Cell Code for Modeling Plasma Based Accelerators", in Computational Science — ICCS 2002, edited by P. M. A. Sloot, A. G. Hoekstra, C. J. K. Tan, and J. J. Dongarra (2002), pp. 342–351.

[47] J. P. Boris, "Relativistic plasma simulation-optimization of a hybrid code", in Proceeding of Fourth Conference on Numerical Simulations of Plasmas (1970), pp. 3–67.

[48] K. Yee, "Numerical solution of initial boundary value problems involving maxwell's equations in isotropic media", IEEE Transactions on Antennas and Propagation **14**, 302–307 (1966).

[49] M. Masujima, *Applied Mathematical Methods in Theoretical Physics* (John Wiley & Sons, Ltd, 2009) Chap. 2.

[50] N. E. Korotkov and A. N. Korotkov, *Integrals Related to the Error Function* (CRC Press, 2020).

[51] M. Lampe, G. Joyce, S. P. Slinker, and D. H. Whittum, "Electron-hose instability of a relativistic electron beam in an ion-focusing channel", Physics of Fluids B: Plasma Physics **5**, 1888–1901 (1993).

[52] F. W. J. Olver, A. B. Olde Daalhuis, D. W. Lozier, B. I. Schneider, R. F. Boisvert, C. W. Clark, B. R. Miller, B. V. Saunders, H. S. Cohl, and M. A. McClain, eds., *NIST Digital Library of Mathematical Functions*, `http://dlmf.nist.gov/`, Release 1.1.5 of 2022-03-15.

[53] P. M. Lapostolle, "Possible Emittance Increase through Filamentation Due to Space Charge in Continuous Beams", IEEE Transactions on Nuclear Science **18**, 1101–1104 (1971).

[54] J. D. Lawson, P. M. Lapostolle, and R. L. Gluckstern, "Emittance, entropy and information", Particle Accelerators **5**, 61–65 (1973).

[55] T. P. Wangler, K. R. Crandall, R. S. Mills, and M. Reiser, "Relation between Field Energy and RMS Emittance in Intense Particle Beams", IEEE Transactions on Nuclear Science **32**, 2196–2200 (1985).

[56] B. R. Kusse and E. A. Westwig, *Mathematical Physics: Applied Mathematics for Scientists and Engineers* (Wiley, 1998).

[57] A. W. Chao, B. Richter, and C.-Y. Yao, "Beam emittance growth caused by transverse deflecting fields in a linear accelerator", Nuclear Instruments and Methods **178**, 1–8 (1980).

[58] D. H. Whittum, W. M. Sharp, S. S. Yu, M. Lampe, and G. Joyce, "Electron-hose instability in the ion-focused regime", Physical Review Letters **67**, 991–994 (1991).

[59] C. Huang et al., "Hosing Instability in the Blow-Out Regime for Plasma-Wakefield Acceleration", Physical Review Letters **99**, 255001 (2007).

[60] T. J. Mehrling, R. A. Fonseca, A. Martinez de la Ossa, and J. Vieira, "Mechanisms for the mitigation of the hose instability in plasma-wakefield accelerators", Physical Review Accelerators and Beams **22**, 031302 (2019).

[61] T. J. Mehrling, R. A. Fonseca, A. Martinez de la Ossa, and J. Vieira, "Mitigation of the Hose Instability in Plasma-Wakefield Accelerators", Physical Review Letters **118**, 174801 (2017).

[62] T. J. Mehrling, C. Benedetti, C. B. Schroeder, E. Esarey, and W. P. Leemans, "Suppression of Beam Hosing in Plasma Accelerators with Ion Motion", Physical Review Letters **121**, 264802 (2018).

[63] F. Batsch et al. (AWAKE Collaboration), "Transition between Instability and Seeded Self-Modulation of a Relativistic Particle Bunch in Plasma", Physical Review Letters **126**, 164802 (2021).

[64] L. Verra et al. (AWAKE Collaboration), “Controlled Growth of the Self-Modulation of a Relativistic Proton Bunch in Plasma”, Physical Review Letters **129**, 024802 (2022).

[65] R. Lehe, C. B. Schroeder, J.-L. Vay, E. Esarey, and W. P. Leemans, “Saturation of the Hosing Instability in Quasilinear Plasma Accelerators”, Physical Review Letters **119**, 244801 (2017).

[66] B. J. Duda, R. G. Hemker, K. C. Tzeng, and W. B. Mori, “A Long-Wavelength Hosing Instability in Laser-Plasma Interactions”, Physical Review Letters **83**, 1978–1981 (1999).

[67] M. C. Kaluza, S. P. D. Mangles, A. G. R. Thomas, Z. Najmudin, A. E. Dangor, C. D. Murphy, J. L. Collier, E. J. Divall, P. S. Foster, C. J. Hooker, A. J. Langley, J. Smith, and K. Krushelnick, “Observation of a Long-Wavelength Hosing Modulation of a High-Intensity Laser Pulse in Underdense Plasma”, Physical Review Letters **105**, 095003 (2010).

[68] B. J. Duda and W. B. Mori, “Variational principle approach to short-pulse laser-plasma interactions in three dimensions”, Physical Review E **61**, 1925–1939 (2000).

[69] D. Morin, *Introduction to Classical Mechanics: With Problems and Solutions* (Cambridge University Press, 2008).

[70] P. Sprangle, J. Krall, and E. Esarey, “Hose-Modulation Instability of Laser Pulses in Plasmas”, Physical Review Letters **73**, 3544–3547 (1994).

[71] K. V. Lotov, “Controlled self-modulation of high energy beams in a plasma”, Physics of Plasmas **18**, 024501 (2011).

[72] K. V. Lotov, “Physics of beam self-modulation in plasma wakefield accelerators”, Physics of Plasmas **22**, 103110 (2015).

[73] P. Sprangle, E. Esarey, J. Krall, and G. Joyce, “Propagation and guiding of intense laser pulses in plasmas”, Physical Review Letters **69**, 2200–2203 (1992).

[74] N. E. Andreev, L. M. Gorbunov, V. I. Kirsanov, A. Pogosova, and R. Ramazashvili, “Resonant excitation of wakefields by a laser pulse in a plasma”, JETP Letters **55**, 571–576 (1992).

[75] O. Jakobsson, S. M. Hooker, and R. Walczak, “Gev-Scale Accelerators Driven by Plasma-Modulated Pulses from Kilohertz Lasers”, Physical Review Letters **127**, 184801 (2021).

[76] J. J. van de Wetering, S. M. Hooker, and R. Walczak, “Stability of the modulator in a plasma-modulated plasma accelerator”, Physical Review E **108**, 015204 (2023).

[77] M. Turner et al. (AWAKE Collaboration), “Experimental Observation of Plasma Wakefield Growth Driven by the Seeded Self-Modulation of a Proton Bunch”, Physical Review Letters **122**, 054801 (2019).

[78] A. Pukhov, N. Kumar, T. Tückmantel, A. Upadhyay, K. Lotov, P. Muggli, V. Khudik, C. Siemon, and G. Shvets, “Phase Velocity and Particle Injection in a Self-Modulated Proton-Driven Plasma Wakefield Accelerator”, Physical Review Letters **107**, 145003 (2011).

[79] W. K. H. Panofsky and W. A. Wenzel, “Some Considerations Concerning the Transverse Deflection of Charged Particles in Radio-Frequency Fields”, Review of Scientific Instruments **27**, 967 (1956).

[80] E. Öz and P. Muggli, “A novel Rb vapor plasma source for plasma wakefield accelerators”, Nuclear Instruments and Methods in Physics Research Section A: Accelerators, Spectrometers, Detectors and Associated Equipment **740** *Proceedings of the first European Advanced Accelerator Concepts Workshop 2013*, 197–202 (2014).

[81] Y. Fang, J. Vieira, L. D. Amorim, W. Mori, and P. Muggli, “The effect of plasma radius and profile on the development of self-modulation instability of electron bunches”, Physics of Plasmas **21**, 056703 (2014).

[82] C. B. Schroeder, C. Benedetti, E. Esarey, F. J. Grüner, and W. P. Leemans, “Particle beam self-modulation instability in tapered and inhomogeneous plasma”, Physics of Plasmas **19**, 010703 (2012).

[83] F. Braunmüller et al. (AWAKE Collaboration), “Proton Bunch Self-Modulation in Plasma with Density Gradient”, Physical Review Letters **125**, 264801 (2020).

[84] P. I. Morales Guzmán et al. (AWAKE Collaboration), “Simulation and experimental study of proton bunch self-modulation in plasma with linear density gradients”, Physical Review Accelerators and Beams **24**, 101301 (2021).

[85] P. Chen, J. J. Su, T. Katsouleas, S. Wilks, and J. M. Dawson, “Plasma Focusing for High-Energy Beams”, IEEE Transactions on Plasma Science **15**, 218–225 (1987).

[86] Y. A. Mitropol’skii and V. G. Kolomiets, “Asymptotic methods in the theory of nonlinear random oscillations”, Ukrainian Mathematical Journal **46**, 1110–1116 (1994).

[87] J.-L. Vay, “A New Absorbing Layer Boundary Condition for the Wave Equation”, Journal of Computational Physics **165**, 511–521 (2000).

Appendix A

Simulation details

The algorithm employed to solve Maxwell's equations numerically in all simulations in this work is the Yee (finite-difference time-domain) solver. Smoothing of the electromagnetic fields was not applied unless explicitly mentioned. The particle interpolation in all simulations is quadratic.

The boundary conditions for the electromagnetic fields and the simulation particles are the same within each simulation geometry. By default, all boundaries are "open". For the electromagnetic fields, this corresponds to an absorbing, perfectly-matched-layer algorithm [87]. In both two-dimensional geometries (Cartesian and axisymmetric cylindrical), the electromagnetic boundaries in the transverse direction were set to perfect electrical conductors, since this minimized spurious field phenomena at the boundary. Note that there is always a vacuum gap between the transverse window boundaries and any plasma (except for the axial boundary in cylindrical geometry, which also has a specific type of boundary).

The emittance and energy spread of a particle bunch can be contemplated in the simulations imperfectly by introducing an uncorrelated thermal distribution of the velocity along any direction. For the emittance, this corresponds to assuming that the bunch is at its waist. As input for the thermal distribution, we simply require the standard deviation of the Maxwellian distribution $u_{\mathrm{th},i}$, where i is the coordinate. Note that u represents a proper velocity and is normalized to c, i.e., $\hat{u} = u/c = \gamma v/c$.

For the transverse emittance, a simple correspondence to $\hat{u}_{\mathrm{th}}$ can be found by assuming that $p_{x,y}/p_z \ll 1$, where x and y are the transverse coordinates and z is the longitudinal coordinate, and a bi-Gaussian phase space distribution given by (e.g. along x):

$$f(x, x') = \frac{1}{2\pi\sigma_x\sigma_{x'}} \exp\left(-\frac{x^2}{2\sigma_x^2}\right) \exp\left(-\frac{x'^2}{2\sigma_{x'}^2}\right) \ , \tag{A.1}$$

where $x' = \tan(p_x/p_z)$, and σ_x and $\sigma_{x'}$ are the RMS position and angle, respectively. In this case, the geometric emittance is

$$\varepsilon_x = \sqrt{\langle x^2\rangle \langle x'^2\rangle - \langle xx'\rangle^2} = \sqrt{\sigma_x^2\sigma_{x'}^2 - 0} = \sigma_x\sigma_{x'} \ . \tag{A.2}$$

Note that the transverse angle can be approximated as $x' \approx p_x/p_z$ due to our small-angle assumption, and therefore $\sigma_{x'} \approx \sigma_{p_x}/\sigma_{p_z}$. Replacing this in Eq. A.2 and solving for σ_{p_x}, we obtain

$$\sigma_{p_x} = \varepsilon_x \frac{p_z}{\sigma_x} \quad \Leftrightarrow \quad \frac{\sigma_{p_x}}{mc} = \varepsilon_x \frac{p_z}{mc} \frac{1}{\sigma_x} \, , \tag{A.3}$$

where we divided the equation by mc. Noticing that the momentum divided by mc corresponds to

a proper velocity, we can rewrite $\sigma_{p_x}/(mc) = \gamma\sigma_{v_x}/c = \hat{u}_{\mathrm{th},x}$ and $p_z/(mc) = \gamma\sigma_{v_z}/c = \gamma\beta$. Thus the value for the thermal velocity component (in the lab frame) corresponding to an energy spread or emittance is determined via

$$\hat{u}_{\mathrm{th},x} = \frac{\varepsilon_{N,x}\ [\mathrm{mm\ mrad}]}{\sigma_x\ [\mathrm{mm}]}\ , \tag{A.4}$$

where we also used the definition of the normalized emittance, $\varepsilon_N = \gamma\beta\varepsilon$.

The complete parameters for the different sets of simulations are given in the tables below. For each set, there is a table of parameters that are common to all the simulations in the set, and a table for the differing parameters, featuring an item reference for each individual simulation.

With the exception of simulation A.5.2, where many test electrons are distributed along the bunch, there are always two particle species: the plasma electrons and the driving bunch particles. The positive, immobile plasma ions are taken into account implicitly, since the code assumes that there is net charge neutrality at $t = 0$. This poses an issue when a charged particle bunch is present at the beginning of the simulation (since the net charge should not be zero in reality). This inaccuracy is minimized by computing the initial electric field associated with the bunch charge, and having it propagate for the length of one simulation window in vacuum.

The longitudinal shape of the driving bunch is consistent throughout all simulations, and is given by:

$$f(\zeta) = \frac{1}{2}\left[1 + \cos\left(\sqrt{\frac{\pi}{2}}\frac{\zeta - \zeta_c}{\sigma_z}\right)\right]\ , \tag{A.5}$$

where the RMS length σ_z was generally taken as 12 cm, with the exception of the simulations in Sec. A.5, where $\sigma_z = 12.6\ \mathrm{cm}$.

The number of particles per cell for the plasma electrons and the bunch particles is symbolized as $N_{\mathrm{ppc,pl}}$ and $N_{\mathrm{ppc,b}}$, respectively. The grid and window sizes are indicated in terms of length$\times$width($\times$depth). The shape of the transverse bunch profile is specified according to the initials G (Gaussian), FT (flat top) and SG (super-Gaussian).

A.1 Hosing studies – 2D Cartesian geometry

Table A.1: Parameters of simulations in 2D Cartesian geometry.

Common parameters	
n_0 $[10^{14}\ \mathrm{cm}^{-3}]$	0.5
n_{b0} $[n_0]$	0.001
γ_b	480
Bunch particles	e^-
Seeding	$y_{c0} = 0.05\ \sin(1.07\,\zeta)$
Grid size	1750×270
Window size $[k_p^{-1} \times k_p^{-1}]$	140×4
Δt $[\omega_p^{-1}]$	0.0095
$N_{\mathrm{ppc,pl}}$	2
$N_{\mathrm{ppc,b}}$	4
#CPUs	2400
ave. CPUh	200

Differing parameters			
Item	$g(y)$	Bunch transv. size $[k_p^{-1}]$	$t_{\max}$ $[\omega_p^{-1}]$
A.1.1	G	$\sigma_{y0} = 0.266$	6405
A.1.2	FT	$r_{b0} = 0.266 \quad (\sigma_{\mathrm{RMS}} = 0.188)$	6405
A.1.3	G	$\sigma_{y0} = 0.266$	2135

A.2 Hosing studies – 3D geometry

Table A.2: Parameters of simulations in 3D geometry.

Common parameters	
n_0 $[10^{14}\ \mathrm{cm}^{-3}]$	0.5
n_{b0} $[n_0]$	0.001
γ_b	480
$g(\underline{x}_\perp)$	FT
Bunch particles	e^-
Window size $[k_p^{-1} \times k_p^{-1} \times k_p^{-1}]$	140×2×2
$N_{\mathrm{ppc,b}}$	2

Differing parameters

Item	Bunch transv. size $[k_p^{-1}]$	Seeding	Grid size	Δt $[\omega_p^{-1}]$	$t_{\max}$ $[\omega_p^{-1}]$	$N_{\mathrm{ppc,pl}}$	#CPUs	ave. CPUh
A.2.1	$r_{b0} = 0.1$	$y_{c0} = 0.01\ \sin(\zeta)$	1750×660^2	0.0019	140	3	7680	33100
A.2.2	$r_{b0} = 0.1$ (osc.)	$y_{c0} = 0.01\ \sin(\zeta)$ $r_{10} = 0.4\ \cos(\zeta)$	1750×660^2	0.0019	140	3	7680	33100
A.2.1	$r_{b0} = 0.266$	$y_{c0} = 0.027\ \sin(1\zeta)$	1750×250^2	0.005	3880	2	2400	44040
A.2.2	$r_{b0} = 0.266$	$y_{c0} = 0.027\ \sin(\zeta)$	1750×250^2	0.005	3880	2	2400	46430
A.2.3	$r_{b0} = 0.266$	$y_{c0} = 0.027\ \sin(1\zeta)$	1750×250^2	0.005	3880	2	2400	46330

A.3 Comparison to SMI theory – 2D axisymmetric geometry

Table A.3: Parameters of simulations in 2D axisymmetric geometry for comparisons to SMI theory.

Common parameters	
n_0 $[10^{14}\ \mathrm{cm}^{-3}]$	2
n_{b0} $[n_0]$	0.039684
γ_b	427
$g(r)$	FT
Bunch particles	e^+
Bunch transv. size $[k_p^{-1}]$	$r_{b0} = 0.75222$ $(\sigma_{\mathrm{RMS}} = 0.5319)$
Other details	
Window size $[k_p^{-1} \times k_p^{-1}]$	140×4
$t_{\max}$ $[\omega_p^{-1}]$	300
$N_{\mathrm{ppc,pl}}$	4
$N_{\mathrm{ppc,b}}$	4
#CPUs	2400

Differing parameters				
Item	Seeding	Grid size	Δt $[\omega_p^{-1}]$	ave. CPUh
A.3.1	$r_{10} = 0.1\ \sin(\zeta - \zeta_s)$	2800×400	0.008	30
A.3.2	$r_{10} = 0.01\ \sin(\zeta - \zeta_s)$	2800×1200	0.003	100

A.4 Effect of hosing mitigation on SMI – 2D axisym. geometry

Two cases for the self-modulated bunch were considered: one with a density step of +4% at $z = 0.5\, k_\beta^{-1}$ and one without. For each of these cases, two simulations were performed: one with a two-step configuration for hosing mitigation and one without. This corresponds to four simulations in total.

Table A.4: Parameters of simulations in 2D axisymmetric geometry for the effect of hosing mitigation on the SMI.

Common parameters	
n_0 $[10^{14}\ \mathrm{cm}^{-3}]$	0.5
n_{b0} $[n_0]$	0.001
γ_b	480
$g(r)$	G
Bunch particles	e^-
Bunch transv. size $[k_p^{-1}]$	$\sigma_{r0} = 0.266$
Seeding	RIF at ζ_c
Grid size	5600×300
Window size $[k_p^{-1} \times k_p^{-1}]$	280×3
Δt $[\omega_p^{-1}]$	0.008
$t_{\max}$ $[\omega_p^{-1}]$	7000
$N_{\mathrm{ppc,pl}}$	4
$N_{\mathrm{ppc,b}}$	4
#CPUs	4096
ave. CPUh	950

A.5 AWAKE-related studies – 2D axisymmetric geometry

In these simulations, a five-pass binomial smoothing algorithm is applied to the electromagnetic fields for particle interpolation at every time step. More specifically, a 1, 2, 1 stencil is applied four times, followed by a -5, 14, 5 stencil. Note that this smoothing does not affect the actual electromagnetic fields used in the field solver.

Table A.5: Parameters of simulations in 2D axisymmetric geometry for AWAKE-related studies.

Common parameters	
n_0 $[10^{14}\ \mathrm{cm}^{-3}]$	7
n_{b0} $[n_0]$	0.0027
$g(r)$	G
Bunch particles	p^+
Bunch transv. size $[k_p^{-1}]$	$\sigma_{r0} = 1.41$
Seeding	RIF at ζ_c
Grid size	20063×425
Window size $[k_p^{-1} \times k_p^{-1}]$	1663×8
Δt $[\omega_p^{-1}]$	0.012
$t_{\max}$ $[\omega_p^{-1}]$	53000
$N_{\mathrm{ppc,pl}}$	4
$N_{\mathrm{ppc,b}}$	4

Differing parameters

Item	γ_b	Other details	#CPUs	ave. CPUh
A.5.1	480		2400	20000
A.5.2	480	Electrons injected along bunch	4608	95000
A.5.3	427		8192	17190
A.5.4	427	Step down 3% over $\Delta z = 50\ k_p^{-1}$ at $z = 2.5\ \mathrm{m}$	8192	16960
A.5.5	427	Step up 3% over $\Delta z = 50\ k_p^{-1}$ at $z = 2.5\ \mathrm{m}$	8192	16810

A.6 Self-modulation studies – 2D axisymmetric geometry

Table A.6: Parameters of simulations in 2D axisymmetric geometry for self-modulation studies.

Common parameters	
n_0 $[10^{14}\ \mathrm{cm}^{-3}]$	2
n_{b0} $[n_0]$	0.01984
γ_b	427
Bunch particles	$q_b = e,\ M_b = 50\, m_e$
Grid size	5600×300
Window size $[k_p^{-1} \times k_p^{-1}]$	280×3
Δt $[\omega_p^{-1}]$	0.008
$t_{\max}$ $[\omega_p^{-1}]$	5280
$N_{\mathrm{ppc,pl}}$	4
$N_{\mathrm{ppc,b}}$	4

Differing parameters

Item	$g(r)$	Bunch transv. size $[k_p^{-1}]$	Seeding	Other details	#CPUs	ave. CPUh
A.6.1	G	$\sigma_{r0} = 0.53$	–		4096	600
A.6.2	G	$\sigma_{r0} = 0.53$	$r_{10} = 0.1\ \sin[0.8(\zeta - \zeta_s)]$		4096	600
A.6.3	G	$\sigma_{r0} = 0.53$	$r_{10} = 0.1\ \sin[\frac{1}{3}(\zeta - \zeta_s)]$		4096	600
A.6.4	G	$\sigma_{r0} = 0.53$	$r_{10} = 0.1\ \sin[k(\zeta - \zeta_s)]$		4096	600
A.6.5	G	$\sigma_{r0} = 0.53$	$r_{10} = 0.1\ \sin[0.5(\zeta - \zeta_s)]$		4096	600
A.6.6	SG ($p = 2$)	$\sigma_{\mathrm{RMS}} = 1.06$	$r_{10} = 0.1\ \sin[k(\zeta - \zeta_s)]$		4096	600
A.6.7	SG ($p = 4$)	$\sigma_{\mathrm{RMS}} = 1.05$	$r_{10} = 0.1\ \sin[k(\zeta - \zeta_s)]$		4096	600
A.6.8	SG ($p = 4$)	$\sigma_{\mathrm{RMS}} = 1.05$	$r_{10} = 0.1\ \sin[k(\zeta - \zeta_s)]$		4096	600
A.6.9	SG ($p = 4$)	$\sigma_{\mathrm{RMS}} = 1.05$	$r_{10} = 0.1\ \sin[k(\zeta - \zeta_s)]$		4096	600
A.6.10	G	$\sigma_{r0} = 0.53$	$r_{10} = 0.1\ \sin(\zeta - \zeta_s)$	Step down 4% at $z = 0.5\ k_\beta^{-1}$	2400	550
A.6.11	G	$\sigma_{r0} = 0.53$	$r_{10} = 0.1\ \sin(\zeta - \zeta_s)$	Step up 4% at $z = 0.5\ k_\beta^{-1}$	2400	550
A.6.12	G	$\sigma_{r0} = 0.53$	$r_{10} = 0.1\ \sin(\zeta - \zeta_s)$		2400	550

Appendix B

Phase shift measurement method

Our objective is to measure the phase shift between two periodic curves with the same oscillating frequency. We use a cross-correlation of both curves to achieve this, which could be understood as shifting them with respect to each other and finding the amount of shift where their superposition is maximized.

As an example, Fig. B.1 shows the initial centroid and initial plasma response from a 2D simulation where the wavenumber for the centroid perturbation is $0.9\ k_p$. The cross-correlation for these two curves is defined as

$$(y_c \star \langle F_y \rangle)(\zeta') = \int_{-\infty}^{\infty} y_c(\zeta)\ \langle F_y \rangle (\zeta + \zeta')\ d\zeta\ , \tag{B.1}$$

or, for a finite region L,

$$(y_c \star \langle F_y \rangle)(\zeta') = \int_{-L}^{L} y_c(\zeta)\ \langle F_y \rangle (\zeta + \zeta')\ d\zeta\ . \tag{B.2}$$

The cross-correlation for the curves in Fig. B.1 is shown in Fig. B.2a). We are interested in finding the amount of shift ζ' within one wavelength $\lambda = 2\pi/k$ that leads to the most superposition between both curves, i.e., that maximizes the cross-correlation. We therefore find the location of the maximum of $(y_c \star \langle F_y \rangle)$ within $\zeta' = [0, \lambda]$, as illustrated in Fig. B.2b). The red dotted line denotes the shift $\zeta'_{\max}$ found in this case. The final phase shift in radians is calculated according to $\Delta\phi = 2\pi \cdot \zeta'_{\max}/\lambda$. In Fig. B.2, for example, $\zeta'_{\max} = 0.32\ k_p^{-1}$ and $\lambda \approx 6.98\ k_p^{-1}$, which yields the phase shift $\Delta\phi \approx 0.29\ \mathrm{rad}$.

This measurement method is also applied to simulation data related to the self-modulation instability. Whereas the hosing plasma response is purely oscillatory, the plasma response that drives the SMI, given by $\langle rF_r \rangle / \sigma_r$, typically consists of an adiabatic component $F_{\mathrm{SM},0}$ and an oscillatory component $F_{\mathrm{SM},1}$. Since the slowly-varying component may confound our interpretation of the cross-correlation, it is subtracted from the raw data before evaluating the cross-correlation. To obtain $F_{\mathrm{SM},0}$, a moving average is performed with a centered window measuring one oscillation period ($\lambda = 2\pi/k$).

An example of the original plasma response data and the obtained adiabatic component is given in Fig. B.3a). The oscillating component remaining from the subtraction is shown in Fig. B.3b) (blue curve), along with the initial RMS radius of the bunch (black curve). The cross-correlation of these two curves is displayed in Fig. B.4. Once again, the phase shift is determined by finding the maximum of the cross-correlation within the first oscillation wavelength [see red dotted line in Fig. B.4b)].

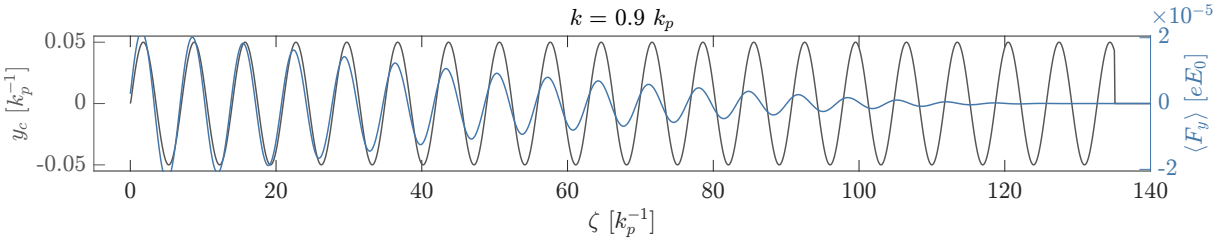

Figure B.1: Initial centroid (black line) and initial average transverse force (blue line) from a 2D slab particle-in-cell simulation.

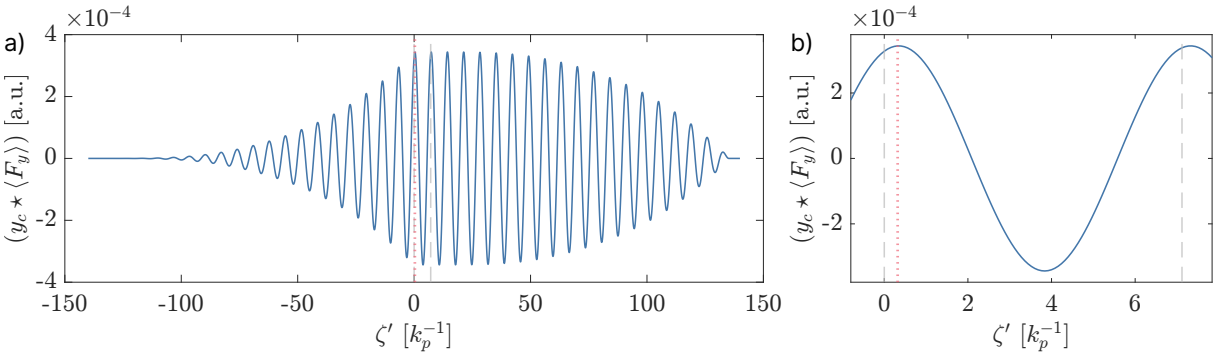

Figure B.2: Cross-correlation of the curves in Fig. B.1: a) full data and b) detail. The dashed grey lines indicate the limits $\zeta' = \{0, \lambda\}$ and the red dotted line indicates the location of the maximum within this region.

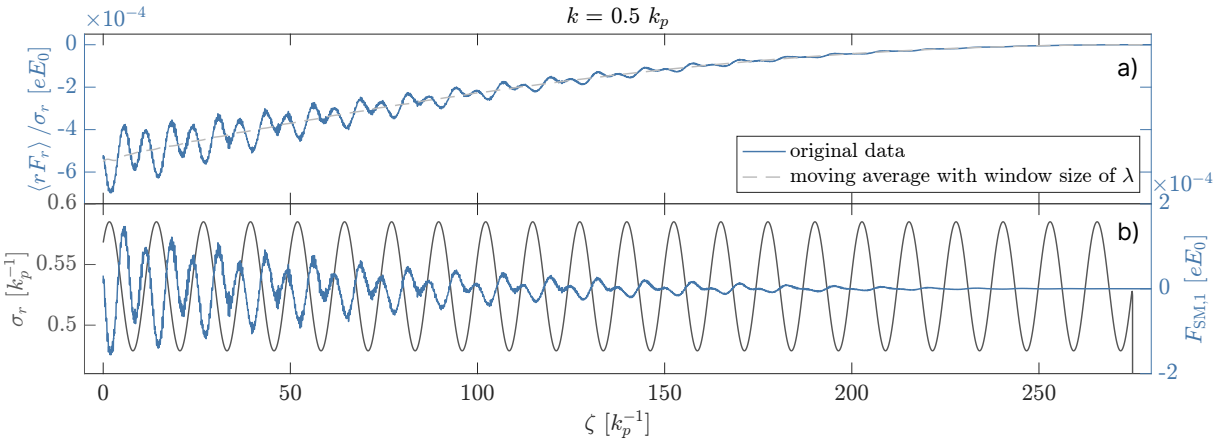

Figure B.3: a) Initial SMI-driving plasma response (blue curve) and its adiabatic component (dashed grey curve), obtained with a moving average. b) Initial RMS radius of the bunch (black curve) and oscillatory component of the initial plasma response (blue curve). Data obtained from a 2D cylindrical particle-in-cell simulation.

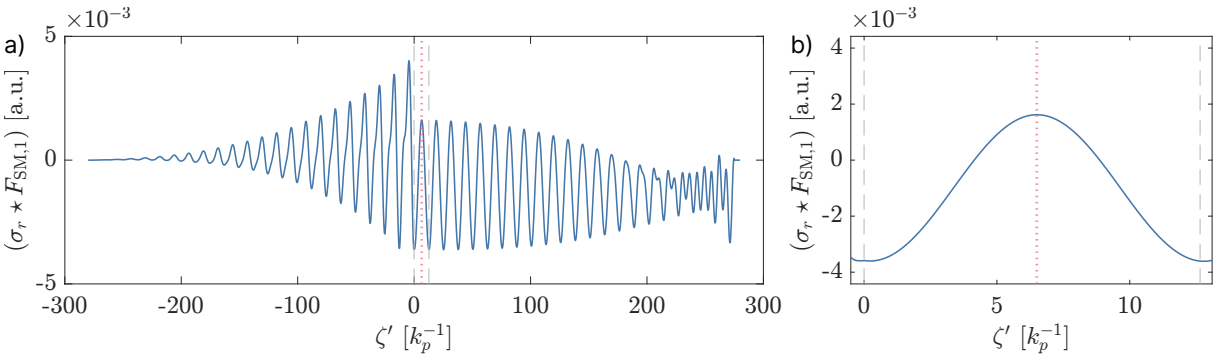

Figure B.4: Cross-correlation of the curves in Fig. B.3b): full data (a) and detail (b). The dashed grey lines indicate the limits $\zeta' = \{0, \lambda\}$ and the red dotted line indicates the location of the maximum within this region.